



저작자표시-비영리-변경금지 2.0 대한민국

이용자는 아래의 조건을 따르는 경우에 한하여 자유롭게

- 이 저작물을 복제, 배포, 전송, 전시, 공연 및 방송할 수 있습니다.

다음과 같은 조건을 따라야 합니다:



저작자표시. 귀하는 원저작자를 표시하여야 합니다.



비영리. 귀하는 이 저작물을 영리 목적으로 이용할 수 없습니다.



변경금지. 귀하는 이 저작물을 개작, 변형 또는 가공할 수 없습니다.

- 귀하는, 이 저작물의 재이용이나 배포의 경우, 이 저작물에 적용된 이용허락조건을 명확하게 나타내어야 합니다.
- 저작권자로부터 별도의 허가를 받으면 이러한 조건들은 적용되지 않습니다.

저작권법에 따른 이용자의 권리는 위의 내용에 의하여 영향을 받지 않습니다.

이것은 [이용허락규약\(Legal Code\)](#)을 이해하기 쉽게 요약한 것입니다.

[Disclaimer](#)

이학박사 학위논문

Development of Thermally
Activated Delayed Fluorescence
Emitters for Highly Efficient
Organic Light-Emitting Diodes

고효율의 유기 발광 소자를 위한 열 활성화 지연
형광 발광체의 개발

2022 년 8 월

서울대학교 대학원

화학부 유기화학전공

이 영 남

Development of Thermally Activated Delayed Fluorescence Emitters for Highly Efficient Organic Light-Emitting Diodes

지도 교수 홍종인

이 논문을 이학박사 학위논문으로 제출함
2022 년 08 월

서울대학교 대학원
화학과 유기화학전공
이영남

이영남의 이학박사 학위논문을 인준함
2022 년 8 월

위 원 장 _____ 김병문 (인)

부위원장 _____ 홍종인 (인)

위 원 _____ 박수영 (인)

위 원 _____ 이동환 (인)

위 원 _____ 김병수 (인)

Abstract

Development of Thermally Activated Delayed Fluorescence Emitters for Highly Efficient Organic Light–Emitting Diodes

Youngnam Lee

Major in Organic Chemistry

Department of Chemistry

The Graduate School

Seoul National University

Thermally activated delayed fluorescence (TADF) emitters significantly improve the internal quantum efficiency (IQE) and external quantum efficiency (EQE) of organic light–emitting diodes (OLEDs). The TADF molecules can harvest both singlet and triplet excitons through efficient reverse intersystem crossing (RISC), which is not available in conventional fluorescent materials. The TADF emitters based on twisted electron donor–acceptor geometries and multiple resonance (MR) effects can effectively reduce the energy difference between the lowest singlet and triplet excited state (ΔE_{ST}). Therefore, the triplet state can be converted to the singlet state using the surrounding thermal energy, thus enabling 100% IQE.

Based on the TADF concept, 3 types of TADF emitters were designed and synthesized for highly efficient OLEDs.

Chapter 2 is focused on TADF emitters containing 1,5-naphthyridine as an electron acceptor and phenoxazine and phenothiazine as electron donors, namely, 2,6-bis(4-(10*H*-phenoxazin-10-yl)phenyl)-1,5-naphthyridine (NyDPO) and 2,6-bis(4-(10*H*-phenothiazin-10-yl)phenyl)-1,5-naphthyridine (NyDPt). Because of the linear molecular structures, NyDPO and NyDPt showed high horizontal emitting dipole ratios of 81% and 84%, respectively. Furthermore, NyDPO and NyDPt exhibited TADF characteristics with photoluminescence quantum yields (PLQYs) of 79% and 45%, respectively. In particular, NyDPt showed dual photoluminescence (PL) emission from quasi-axial and quasi-equatorial conformers. However, only quasi-equatorial emission was observed in the OLED at low current density, resulting in a high device efficiency despite a low PLQY. OLED devices based on NyDPO and NyDPt exhibited high external quantum efficiencies (EQEs) of 29.9% and 25.8%, and maximum luminance values of 33540 cd m⁻² and 14480 cd m⁻², respectively

Chapter 3 is about highly efficient 10-(5,9-dioxa-13*b*-boranaphtho[3,2,1-*de*]anthracen-7-yl)-10*H*-dispiro[acridine-

9,9' -anthracene-10',9''-fluorene] (OBOtSAc) and 10-(2,12-di-*tert*-butyl-5,9-dioxa-13*b*-boranaphtho[3,2,1-de]anthracen-7-yl)-10*H*-dispiro[acridine-9,9'-anthracene-10',9''-fluorene] (tBuOBOtSAc) emitters, comprising almost perpendicularly linked rigid 5,9-dioxa13*b*-boranaphtho[3,2,1-de]anthracene (OBO) electron acceptors and a rigid and linear tri-spiral acridine electron donor. OBOtSAc and tBuOBOtSAc show deep-blue emission (λ_{\max} = 452 and 446 nm) with narrow full width at half maximum (FWHM) values of 50 and 48 nm, respectively. Due to the rigid and twisted structures, and the appropriate singlet and triplet energy levels of both emitters, 10 wt% doped films of OBOtSAc and tBuOBOtSAc in a bis[2-(diphenylphosphino)phenyl]ether oxide (DPEPO) host show efficient TADF emission and PLQYs of 97% and 90%, respectively. Moreover, linear-shaped OBOtSAc and tBuOBOtSAc lead to excellent horizontal emitting dipole orientations (88% and 90%, respectively). Consequently, OLED devices using OBOtSAc and tBuOBOtSAc exhibit maximum EQEs of 31.2% and 28.2%, respectively, and Commission Internationale de l'Éclairage (CIE) coordinates of (0.147, 0.092) and (0.149, 0.061), respectively

Chapter 4 is a study on MR-TADF emitters, namely, 2,12-dichloro-*N,N*,5,9-tetrakis(4-chlorophenyl)-5,9-dihydro-5,9-

diaza-13*b*-boranaphtho[3,2,1-*de*]anthracen-7-amine (Cl-MR) and 2,12-dibromo-*N,N*,5,9-tetrakis(4-bromophenyl)-5,9-dihydro-5,9-diaza-13*b*-boranaphtho[3,2,1-*de*]anthracen-7-amine (Br-MR). Cl-MR and Br-MR showed a decreased lifetime of delayed fluorescence and enhanced reverse intersystem crossing rate through halogen atoms without any changes in ΔE_{ST} and orbital distribution. As a result, Cl-MR showed high PLQY of 85% and EQE of 27.2%. However, Br-MR doesn't have any enhancement of PLQY and EQE. Different performances of Cl-MR and Br-MR were supported by analyzing the rate constant of excited states and bond dissociation energy (BDE) of carbon-halogen bonds.

Keywords : Emitter, Horizontal dipole orientation, Organic light-emitting diode, Polycyclic aromatic hydrocarbon, Thermally activated delayed fluorescence

Student Number : 2016-22748

Table of Contents

Abstract	i
Table of Contents	v
Chapter 1. Background	1
1.1. Basics of organic light-emitting diodes.....	2
1.2. Emitters for organic light-emitting diodes.....	5
1.3. Design principles of organic TADF molecules	10
1.4. Light out-coupling efficiency.....	12
1.5. Relationship between molecular shapes and emitting dipole orientations.....	15
1.6. References.....	19
Chapter 2. High-efficiency thermally activated delayed fluorescence emitters <i>via</i> a high horizontal dipole ratio and controlled dual emission.	22
2.1. Introduction	23
2.2. Experimental section	28
2.3. Results and discussion.....	35
2.4. Conclusion.....	49

2.5. References.....	50
2.6. Supplementary data.....	54

**Chapter 3. High-Efficiency Thermally Activated Delayed
Fluorescence Emitters with High Horizontal Orientation and
Narrow Deep-Blue Emission 57**

3.1. Introduction	58
3.2. Experimental section	64
3.3. Results and discussion.....	69
3.4. Conclusion.....	80
3.5. References.....	82
3.6. Supplementary data.....	85

**Chapter 4. Multiple Resonance Thermally Activated Delayed
Fluorescence Enhanced by Halogen Atoms 87**

4.1. Introduction	88
4.2. Experimental section	91
4.3. Results and discussion.....	98
4.4. Conclusion.....	117

4.5. References.....	118
4.6. Supplementary data.....	121
Abstract in Korean (국문초록)	126

Chapter 1. Background

Chapter 1. Background

1.1. Basics of organic light-emitting diodes

Organic light-emitting diodes (OLEDs) are light-emitting devices that are recently used in display areas such as smartphones and TVs. Over the past 25 years, OLED research and development have become a rapidly progressing and expanding field in academia and industry. OLEDs provide a new way for display technology and are emerging to replace older technologies on the market. OLED displays have superior characteristics to liquid crystal displays (LCDs), which are widely commercialized technologies.¹ For example, OLED devices do not require a backlight panel compared to the LCDs. Because OLEDs do not generate light or consume power when they are off, they are not only energy-efficient but also enable "real black color". OLED displays also enable high resolution, wide viewing angles, high contrast colors, and fast response times. Its main advantage is the implementation of flexible OLED displays that can be bent and rolled like a poster, opening up new possibilities for displays, such as foldable smartphones.²

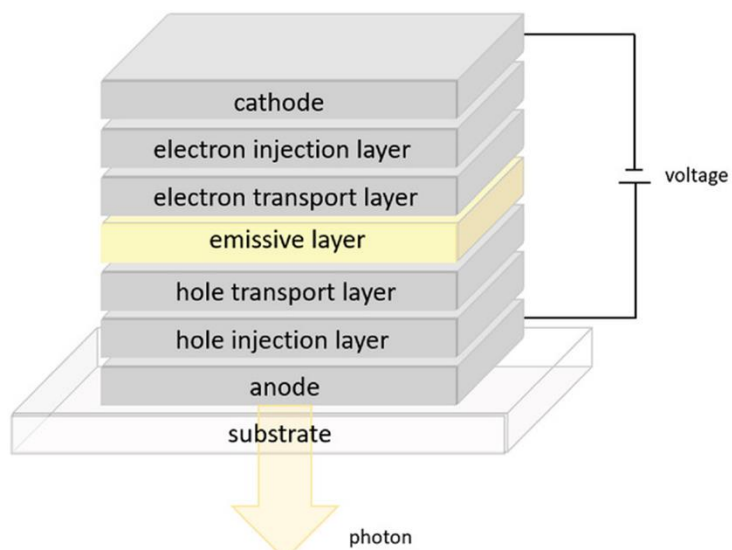


Figure 1–1. A basic organic light–emitting diode (OLED) structure. Reproduced with permission from ref. 1. Copyright 2021 John Wiley & Sons, Inc.

A OLED structure shown in Figure 1–1 is a multilayer device that is typically composed of organic semiconductor layers.^{3,4} An external voltage is applied to inject electrons and holes, i.e. charge carriers, from the cathode and anode. Then, the charge carriers are injected into the electron injection layer (EIL) and hole injection layer (HIL). Next, the electrons and holes pass through the electron transport layer (ETL) and hole transport layer (HTL) to the emission layer (EML), where recombination of the charge carriers and formation of excitons occurs. Electroluminescence (EL) occurs when these excitons are radiatively relaxed from an excited state to a ground state. The rational design of the light-emitting layer, which consists of a host/dopant (emitter) system, is the most important factor in achieving the desired color and high efficiency in OLED devices.⁵

1.2. Emitters for organic light-emitting diodes

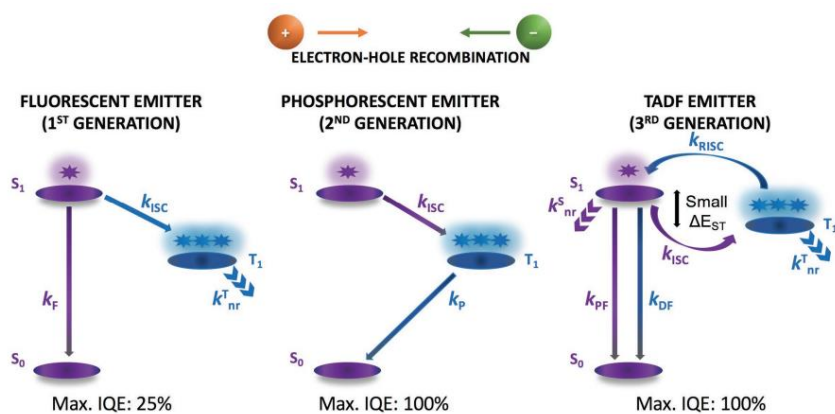


Figure 1–2. Difference of emission mechanism in first–generation (fluorescent), second–generation (phosphorescent), and third–generation (TADF) emitters. F = fluorescence; P = phosphorescence; PF = prompt fluorescence; DF = delayed fluorescence; ISC = intersystem crossing; RISC = reverse intersystem crossing; ΔE_{ST} = the energy difference between the first excited singlet and triplet states; nr = nonradiative. Reproduced with permission from ref. 2. Copyright 2017 John Wiley & Sons, Inc.

1.2.1 Fluorescence emitters

Recombination of electrons and holes in organic semiconductors produces singlet and triplet excitons in a ratio of

1:3 when an electric charge is injected according to spin statistics.⁶ The maximum value of the internal quantum efficiency (IQE, the ratio of the number of generated photons to the number of injected charges) of an OLED using a conventional fluorescent emitter as a dopant is about 25% since only singlet excitons can emit light.⁷ Therefore, the maximum external quantum efficiency (EQE) of the fluorescence OLED can reach approximately 5%, which can be described by the following equation:

$$\text{EQE}_{\text{max}} = \eta_r \times \eta_{\text{ST}} \times \Phi_{\text{PL}} \times \eta_{\text{out}} = \text{IQE}_{\text{max}} \times \eta_{\text{out}}$$

where EQE_{max} and IQE_{max} are the maximum external quantum efficiency and the maximum internal quantum efficiency, respectively. η_r is the proportion of electron-hole recombination, which is supposed to be unity in the ideal case. η_{ST} is the fraction of radiative excitons, Φ_{PL} is the photoluminescence quantum yield (PLQY) of the emitting layer, and η_{out} is the light out-coupling efficiency, which is around 20% for normal OLEDs with an ITO-based flat thin-film architecture. Despite the limited EQE values, the fluorescent emitters have been used for long-lived and stable blue emitters.

1.2.1 Phosphorescence emitters

To enhance the shortcoming of the fluorescence OLED efficiency, Baldo et al. reported an OLED device utilizing a red-emitting organometallic complex called 2,3,7,8,12,13,17,18-octaethyl-21*H*,23*H*-porphyrin platinum(II) (PtOEP) as a dopant in a fluorescence host.⁶ The Pt complex allowed the use of triplet states that were not available in fluorescence materials. Thus, both singlets and triplets were utilized with reported EQE and IQE of 4% and 23%, respectively. The reason that the triplet states can be used for light emission is that they allow intersystem crossing (ISC) in the singlet excited states through strong spin-orbit coupling mediated by the heavy metal (e.g, Ir and Pt).^{6, 8, 9} This research became the starting point for active research on phosphorescence-based OLEDs.

Since 2001, OLED using organometallic complexes with nearly 100% IQE have been reported.¹⁰ Commercial OLED devices for displays are currently based on the green- and red-emitting cyclometalated iridium complexes.¹¹ However, the rarity of the heavy metal complexes is a major drawback and contributes to increased device cost. The potential environmental contamination of these heavy metal complexes is also a concern. Moreover, although organometallic complexes show commercially available performance

in red- and green-emitting devices, blue-emitting organometallic complexes are so far unsatisfactory in terms of material stability, color coordinates, and brightness. Possible reasons for the unsatisfactory device performance may be that triplet polaron annihilation (TPA) causes high-energy polarons leading to device degradation and unstable radical cations causing ligand dissociation or complex isomerization.^{12, 13} There is an urgent need for bright, deep-blue emitting, and stable emitters for OLEDs. This is currently the biggest challenge for emitter designs.

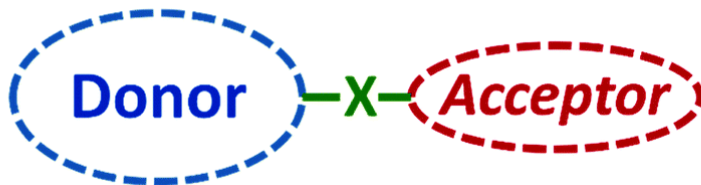
1.2.1 TADF emitters

In response to these demands, thermally activated delayed fluorescence (TADF) is the most promising exciton harvesting technique used in OLED devices after phosphorescence.² After the first reports of OLEDs based on organic TADF emitters in 2011, there has been tremendous interest in efficiency enhancements.^{14, 15} Similar to phosphorescent organometallic emitters, pure organic TADF emitters can achieve 100% IQE by utilizing both singlet and triplet excited states for light emission.¹⁶ One of the important advantages of TADF emitters is that they circumvent problems caused by the use of heavy metal complexes because they are

made of pure organic materials. TADF depends on ΔE_{ST} , which is defined as the energy difference between the lowest singlet state (S_1) and the lowest triplet state (T_1). If ΔE_{ST} is sufficiently small, generally considered to be <0.1 eV, thermal up-conversion from the triplet state to the singlet state by reverse intersystem crossing (RISC) is possible.¹⁷ TADF emitters generally exhibit two types of photoluminescence (PL): prompt fluorescence, which exhibits luminescence directly from singlet excitons, and delayed fluorescence, which exhibits a transition from triplet to singlet state *via* ISC and RISC.

1.3. Design principles of organic TADF molecules

Key goal: Moderate radiative decay rate k_r with small ΔE_{ST}



Methods: Donor-Acceptor backbone

(1) X: Separation of HOMO and LUMO (small ΔE_{ST})

- (a) Introduction of steric hindrance;
- (b) Spiro linker, physical separation of donor and acceptor units;
- (c) X-shaped molecular structure;
- (d) Multiple resonance effect.

(2) Increase the radiative decay rate (k_r)

Increasing the overlap density distribution between the S_0 and S_1 states;
large delocalization of molecular orbitals.

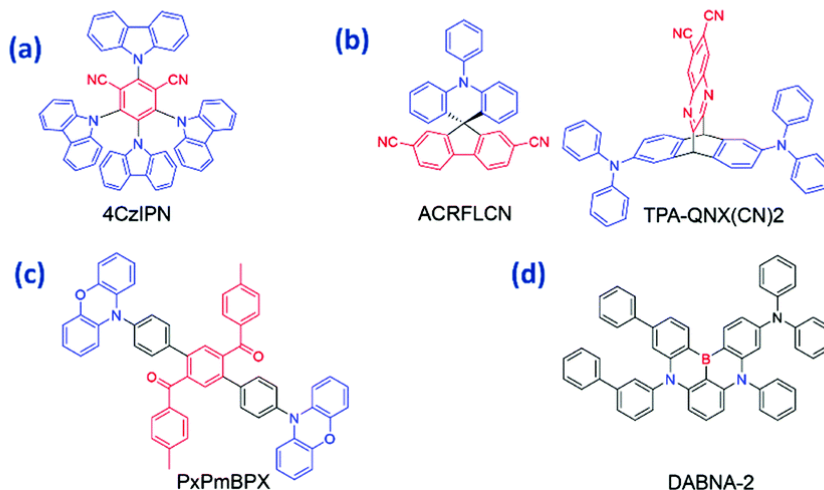


Figure 1–3. Molecular design strategies for efficient TADF molecules. Reproduced with permission from ref. 18. Copyright 2017 The Royal Society of Chemistry.

For TADF to emit, ΔE_{ST} must be small to enable RISC from triplet to singlet excited states.¹⁸ It has been found that small ΔE_{ST} s can be realized by reducing the overlap of the HOMO and LUMO of molecules through intramolecular or intermolecular charge transfer. On the other hand, to obtain high PLQY and EQE, the k_r of the S_1 exciton must be relatively large, which is proportional to the overlap of HOMO and LUMO. Therefore, since small ΔE_{ST} and large k_r conflict with each other for efficient TADF OLEDs, a fine molecular design is required to realize them simultaneously.

Huang et al. (2015) have summarized several design principles of the charge transfer type for the development of the high-efficiency TADF OLEDs.¹⁵ These designs include twisted D-A molecular structures between the donor and acceptor moieties, caused by a bulky substituent, spiro-junction, and physical separation to achieve a small ΔE_{ST} .^{19, 20} In addition, an X-shaped molecular structure and multiple resonance effect have been presented as molecular structures for developing TADF emitters.^{21,}

1.4. Light out-coupling efficiency

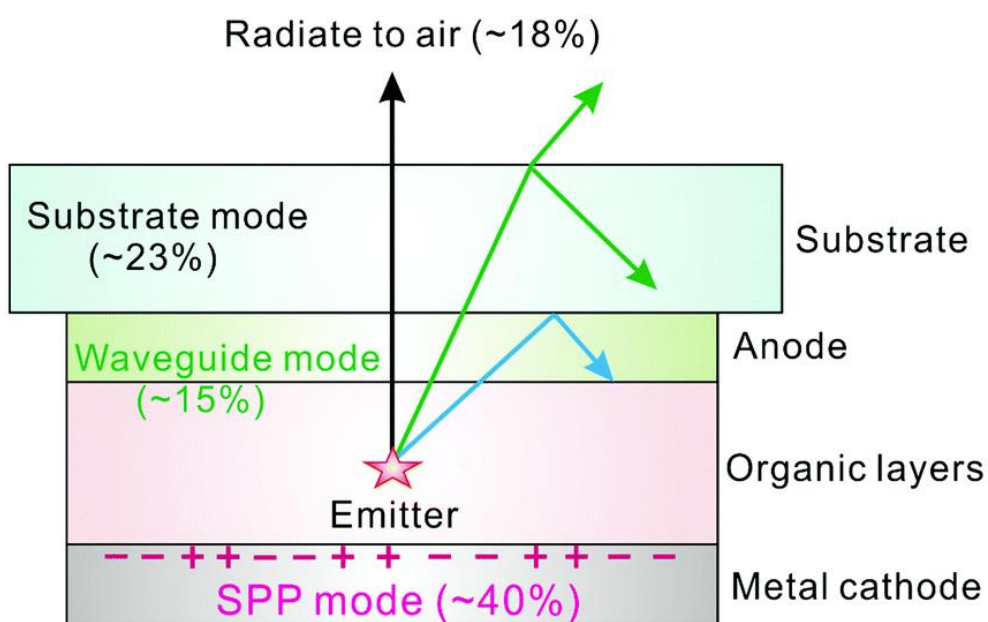


Figure 1–4. Schematic diagram of various types of optical loss channels in conventional planar architectures. Reproduced with permission from ref. 26. Copyright 2020 The Royal Society of Chemistry.

Significant progress has been made in improving the IQE to the 100% using both singlet and triplet states *via* either phosphorescence or TADF. However, most photons emitted from the OLED are trapped within the device due to internal reflection and optical confinement due to different refractive indices for each layer in the multilayer structure.²³⁻²⁶ The fraction of the extracted light to the air η_{out} can be estimated based on ray optics according to Snell's

law:
$$\eta_{\text{out}} = \frac{1}{2n^2}$$

Here n depicts the effective refractive index of the organic layer stack to the air space. Therefore, only about 17% of the photons are emitted from the inside to the outside.²⁷ More accurate processing according to the wave optic method has been extensively investigated to gain more insight into the optical loss channel. As shown in Figure 1-4, excited molecules can be coupled in various optical modes in such a flat stack structure and loss can occur. A significant portion of emitted photons are confined within the substrate (substrate mode, ~23%), guided within the organic layers and transparent anode (waveguide mode, ~15%), and dissipated at the organic-cathode interface (SPP mode, ~40%), resulting in only ~18% of energy flow being radiated outside the device as useful light.

To manufacture high-efficiency OLEDs, it is necessary to improve out-coupling efficiency. Therefore, in recent years, various approaches to enhance out-coupling efficiency have been extensively studied to recover the wasted photons.²⁶

1.5. Relationship between light out-coupling efficiency and emitting dipole orientations

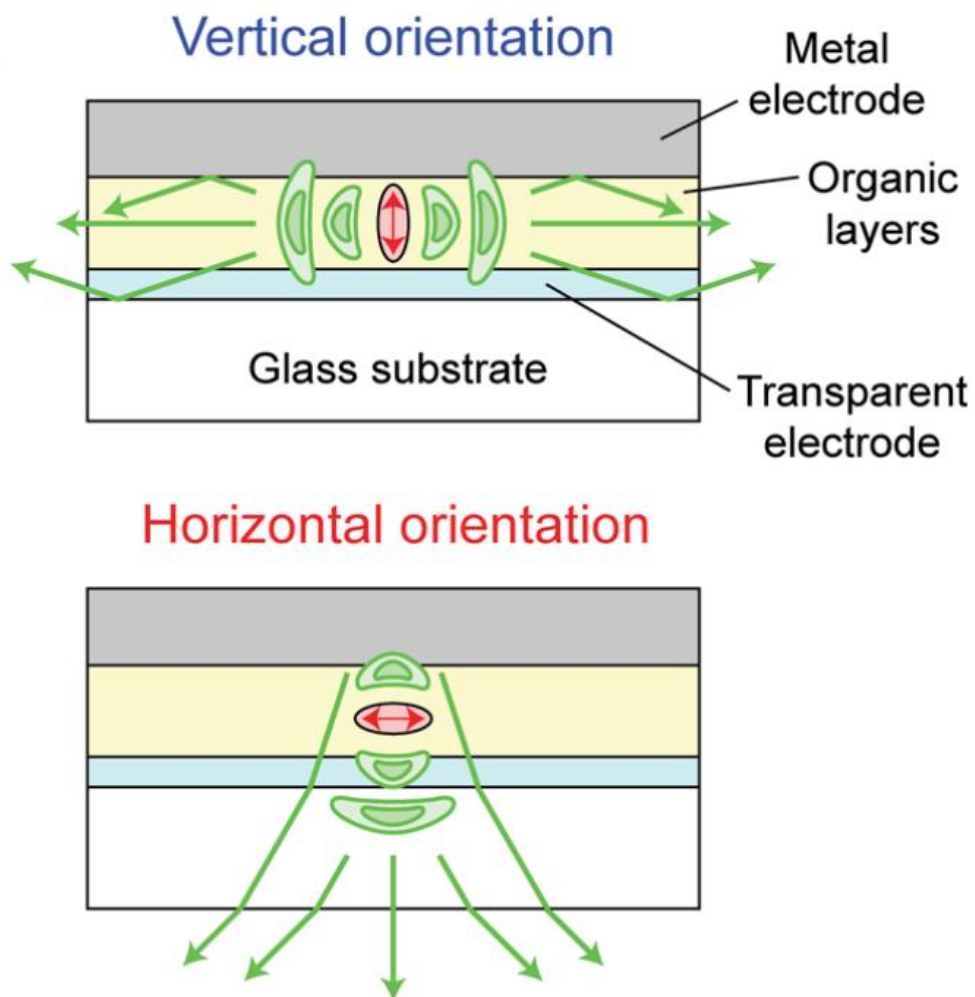


Figure 1–5. Different light out-coupling efficiency between vertical orientation and horizontal orientation. Reproduced with permission from ref. 29. Copyright 2011 The Royal Society of Chemistry.

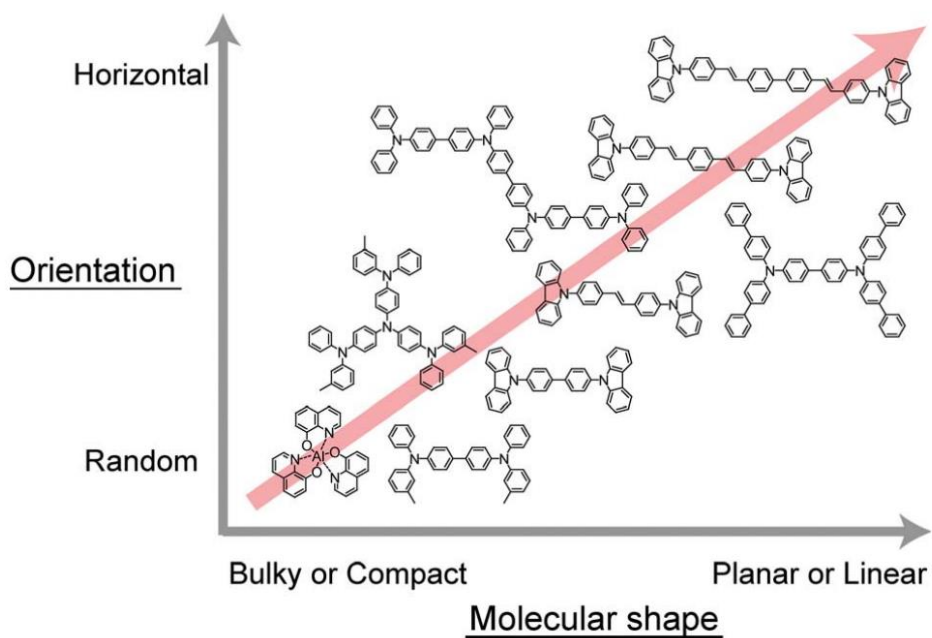


Figure 1–6. Relationship between emitting dipole orientation and molecular shape. Reproduced with permission from ref. 29. Copyright 2011 The Royal Society of Chemistry.

The emitting dipole orientation affects the out-coupling efficiency, which has proven to be one of the important properties for the efficiency of OLEDs. In particular, the horizontal emitting dipole orientation of the emitters reduces light loss in surface plasmon mode and waveguide mode, increasing the out-coupling efficiency of OLEDs. In 2009, Adachi et al. evaluated the optical properties of common organic materials, demonstrating several molecular design guidelines for highly horizontally oriented materials.²⁸ Subsequently, Yokoyama et al. have systematically reviewed several factors of molecular orientation in vacuum-deposited amorphous films of various OLED materials.²⁹

The effect on OLED light extraction according to vertical and horizontal orientation is schematically shown in Figure 1-5.²⁹ Since the photons were emitted mainly in the direction vertical to the transition dipole moment, light extraction is most efficient when the emitting dipole orientation is horizontal. Furthermore, the horizontal dipole orientation increases as the shape of the molecule become linear or planar (Figure 1-6).²⁹ Therefore, it is possible to induce an increase in out-coupling efficiency by controlling the shape of a molecule when designing a new OLED emitter.

TADF-based OLEDs also have been reported to exhibit high efficiencies based on horizontally oriented emitting dipoles. For example, Lee et al. designed an anisotropic molecule using a triscarbazole donor and showed that this molecule can induce 100% horizontal orientation.³⁰ In addition, the triscarbazole-based light-emitting system has a high PLQY due to the wide distribution of orbitals in the HOMO, which improves the transition dipole moment. As a result, it was possible to obtain a high EQE of 30% or more without any other light extraction method. Therefore, TADF emitter designs that enhance the EQE by modulating the orientation of the emission dipole have received more and more attention.

1.6. References

1. G. Hong, X. Gan, C. Leonhardt, Z. Zhang, J. Seibert, J. M. Busch and S. Bräse, *Adv. Mat.*, 2021, 33, 2005630.
2. M. Y. Wong and E. Zysman-Colman, *Adv. Mat.*, 2017, 29, 1605444.
3. X. Yang, G. Zhou and W.-Y. Wong, *Chem. Soc. Rev.*, 2015, 44, 8484–8575.
4. C. Bizzarri, E. Spuling, D. M. Knoll, D. Volz and S. Bräse, *Coordination Chemistry Reviews*, 2018, 373, 49–82.
5. M. Godumala, S. Choi, M. J. Cho and D. H. Choi, *J. Mater. Chem. C*, 2016, 4, 11355–11381.
6. M. A. Baldo, D. F. O'Brien, Y. You, A. Shoustikov, S. Sibley, M. E. Thompson and S. R. Forrest, *Nature*, 1998, 395, 151–154.
7. D. Y. Kondakov, T. D. Pawlik, T. K. Hatwar and J. P. Spindler, *Journal of Applied Physics*, 2009, 106, 124510.
8. H. Sasabe and J. Kido, *European Journal of Organic Chemistry*, 2013, 2013, 7653–7663.
9. B. Minaev, G. Baryshnikov and H. Agren, *Phys. Chem. Chem. Phys.*, 2014, 16, 1719–1758.
10. C. Adachi, M. A. Baldo, M. E. Thompson and S. R. Forrest,

Journal of Applied Physics, 2001, 90, 5048–5051.

11. H. Xu, R. Chen, Q. Sun, W. Lai, Q. Su, W. Huang and X. Liu, Chem. Soc. Rev., 2014, 43, 3259–3302.

12. K. P. Klubek, C. W. Tang and L. J. Rothberg, Org. Electron., 2014, 15, 1312–1316.

13. Y. Zhang, J. Lee and S. R. Forrest, Nat. Commun., 2014, 5, 5008.

14. A. Endo, K. Sato, K. Yoshimura, T. Kai, A. Kawada, H. Miyazaki and C. Adachi, Appl. Phys. Lett., 2011, 98, 083302.

15. Y. Tao, K. Yuan, T. Chen, P. Xu, H. Li, R. Chen, C. Zheng, L. Zhang and W. Huang, Adv. Mat., 2014, 26, 7931–7958.

16. C. Adachi, Japanese Journal of Applied Physics, 2014, 53, 060101.

17. H. Uoyama, K. Goushi, K. Shizu, H. Nomura and C. Adachi, Nature, 2012, 492, 234–238.

18. Z. Yang, Z. Mao, Z. Xie, Y. Zhang, S. Liu, J. Zhao, J. Xu, Z. Chi and M. P. Aldred, Chem. Soc. Rev., 2017, 46, 915–1016.

19. K. Kawasumi, T. Wu, T. Zhu, H. S. Chae, T. Van Voorhis, M. A. Baldo and T. M. Swager, J. Am. Chem. Soc., 2015, 137, 11908–11911.

20. Y. Lee and J.-I. Hong, Adv. Opt. Mater., 2021, 9, 2100406.

21. T. Hatakeyama, K. Shiren, K. Nakajima, S. Nomura, S. Nakatsuka, K. Kinoshita, J. Ni, Y. Ono and T. Ikuta, *Adv. Mat.*, 2016, 28, 2777–2781.
22. S. Y. Lee, T. Yasuda, I. S. Park and C. Adachi, *Dalton Transactions*, 2015, 44, 8356–8359.
23. Q. Yue, W. Li, F. Kong and K. Li, *Advances in Materials Science and Engineering*, 2012, 2012, 985762.
24. G. Gu, D. Z. Garbuzov, P. E. Burrows, S. Venkatesh, S. R. Forrest and M. E. Thompson, *Opt. Lett.*, 1997, 22, 396–398.
25. N. C. Greenham, R. H. Friend and D. D. C. Bradley, *Adv. Mat.*, 1994, 6, 491–494.
26. S.-J. Zou, Y. Shen, F.-M. Xie, J.-D. Chen, Y.-Q. Li and J.-X. Tang, *Materials Chemistry Frontiers*, 2020, 4, 788–820.
27. Y.-J. Lee, S.-H. Kim, J. Huh, G.-H. Kim, Y.-H. Lee, S.-H. Cho, Y.-C. Kim and Y. R. Do, *Appl. Phys. Lett.*, 2003, 82, 3779–3781.
28. D. Yokoyama, A. Sakaguchi, M. Suzuki and C. Adachi, *Org. Electron.*, 2009, 10, 127–137.
29. D. Yokoyama, *J. Mater. Chem. A*, 2011, 21, 19187–19202.
30. S. Y. Byeon, J. Kim, D. R. Lee, S. H. Han, S. R. Forrest and J. Y. Lee, *Adv. Opt. Mater.*, 2018, 6, 1701340.

Chapter 2. High–efficiency thermally activated
delayed fluorescence emitters *via* a high
horizontal dipole ratio and controlled dual
emission

Chapter 2. High-efficiency thermally activated delayed fluorescence emitters *via* a high horizontal dipole ratio and controlled dual emission

A part of this section was published in *Journal of Material Chemistry C*.¹

2.1. Introduction

Organic light-emitting diodes (OLEDs) are currently used in numerous display areas, e.g. smartphones, TVs and others.^{2, 3} However, commercially available OLEDs are more expensive than liquid crystal displays (LCDs) because they use transition metals such as Ir and Pt.⁴ Recently, purely organic thermally activated delayed fluorescence (TADF) materials have been actively developed to not only solve the cost problem but also enhance the photoluminescence quantum yields (PLQYs) using both singlet and triplet excited states.⁵⁻⁸ TADF materials generally have a twisted donor-acceptor structure which reduces the energy difference between the singlet and triplet state (ΔE_{ST}) to almost zero. Although these TADF materials have high PLQYs, the EQEs of the manufactured devices are significantly reduced due to the low out-coupling efficiency.⁹⁻¹¹ Therefore, TADF materials should have not only high PLQYs, but also high light out-coupling efficiency.^{12, 13}

We have previously developed a linear–shape TADF emitter NyDPAc using 1,5–naphthyridine as an electron acceptor and dimethylacridine as an electron donor.¹⁴ NyDPAc has a distorted donor–acceptor–donor structure for TADF emission and exhibited a high horizontal emitting dipole orientation (EDO) ratio (92%) due to its highly linear molecular structure. Therefore, OLED devices using an NyDPAc emitter exhibited a high EQE of 20.9% even at a relatively low PLQY (57%). However, due to weak intramolecular charge transfer (ICT), the ΔE_{ST} of NyDPAc was relatively large, resulting in low triplet utilization and severe device efficiency roll–off. Thus, we assumed that the introduction of a stronger electron donor than dimethylacridine would improve the OLED device efficiencies.

Phenoxazine and phenothiazine have been widely used as strong electron donors.^{15–20} Furthermore, since the hydrogens at their 1,9–position cause severe steric hindrance with ortho hydrogens of the adjacent phenyl groups, TADF emitters having phenoxazine or phenothiazine have a highly distorted structure, inducing separation of the highest occupied molecular orbital (HOMO) and lowest unoccupied molecular orbital (LUMO). In particular, TADF emitters containing phenothiazine have a long C–S bond which leads to quasi–axial and quasi–equatorial conformations, resulting in

dual emission.²¹⁻²³ The quasi-axial form causes a decrease in the PLQY of TADF emitters because ΔE_{ST} is raised due to the less twisted molecular structure between the electron donor and acceptor. Therefore, the emission of the quasi-axial conformation needs to be suppressed for high-efficiency TADF emitters involving phenothiazine.¹⁹⁻²³

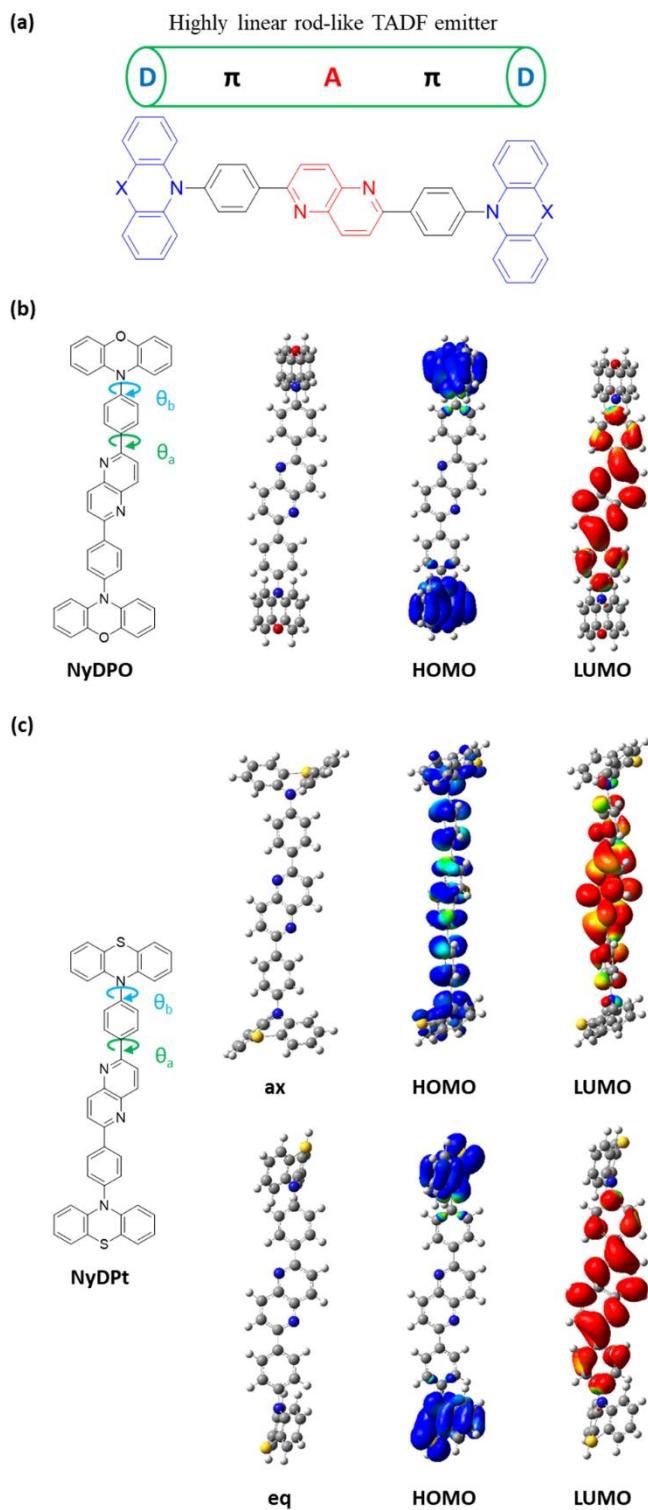


Figure 2–1. (a) Molecular design strategy and (b and c) calculated molecular structures and orbital distributions of NyDPO and NyDPt (blue: HOMO, red: LUMO).

Herein, we designed and synthesized linear rod-like donor-acceptor-donor type TADF emitters using a 1,5-naphthyridine core as an electron acceptor and phenoxazine (NyDPO) or phenothiazine (NyDPt) as an electron donor (Figure 2-1a). A small ΔE_{ST} was expected due to the introduction of phenoxazine or phenothiazine as a stronger electron donor compared with dimethylacridine used as an electron donor moiety of NyDPAc. Furthermore, linear-shape NyDPO and NyDPt were also expected to have high horizontal dipole orientation. As a result, both of them exhibited very small ΔE_{ST} and high horizontal EDO. In particular, NyDPt showed dual photoluminescence (PL) emission arising from the quasi-axial and equatorial conformations of phenothiazine in both toluene solution and doped films in 4,4'-bis(*N*-carbazolyl)-1,1'-biphenyl (CBP). Because of the existence of a quasi-axial form upon photoexcitation, NyDPt showed a lower PLQY of 45% than NyDPO (79%). Nevertheless, OLED devices using NyDPO and NyDPt achieved high external quantum efficiencies (EQEs) of 29.9% and 25.8%, respectively. Considering that the PLQY of NyDPt was close to half of NyDPO, the high EQE of the NyDPt-based OLED devices is remarkable. We examined the relationship between the PLQYs and EQEs and revealed that only the quasi-equatorial conformer was involved in the device's emission at low voltages, resulting in high

EQE.

2.2. Experimental section

2.2.1. Quantum chemical calculations

Density functional theory (DFT) calculations were performed to predict optimized molecular structures and orbital distributions of frontier orbitals. Time-dependent density functional theory (TD-DFT) calculations were performed to calculate energies of excited states. All calculations were employed using Gaussian 09 software at the B3LYP/6-31G(d) level.

2.2.2. Photophysical property analysis

Ultraviolet-visible (UV-vis) spectra were recorded on a Jasco V-730 spectrophotometer. Fluorescence and phosphorescence spectra were recorded on a Jasco FP-8300 spectrophotometer. Absolute quantum efficiency was obtained with a PTI QuantaMaster 40 spectrofluorometer using a 3.2 in. integrating sphere at room temperature. Transient photoluminescence (PL) was measured with time-correlated single photon counting (TCSPC) techniques by using a PicoQuant, FluoTime 250 instrument. A 377 nm pulsed laser was used as an excitation source. For angle-

dependent PL (ADPL) measurements, p-polarized light emitted from PL samples was measured by attaching the film substrate to a half-cylinder lens with index-matching oil and changing the angle between the sample and the detector from -90° to 90° using a motorized rotational stage.

2.2.3. Electrochemical and thermal analysis

Cyclic voltammetry (CV) experiments were conducted in DMF solution (1.00 mM) with 0.1 M tetra-*n*-butylammonium perchlorate (TBAP) as the supporting electrolyte. A glassy carbon electrode was employed as the working electrode and referenced to an Ag reference electrode. All potential values were calibrated against the ferrocene/ferrocenium (Fc/Fc⁺) redox couple. The onset potential was determined from the intersection of two tangents drawn at the rising and background current of the cyclic voltammogram. Differential scanning calorimetry (DSC) and thermogravimetric analysis (TGA) were performed with a TA instrument DSC Q10 and TGA Q50 in a nitrogen atmosphere at a heating rate of $10^\circ\text{C min}^{-1}$.

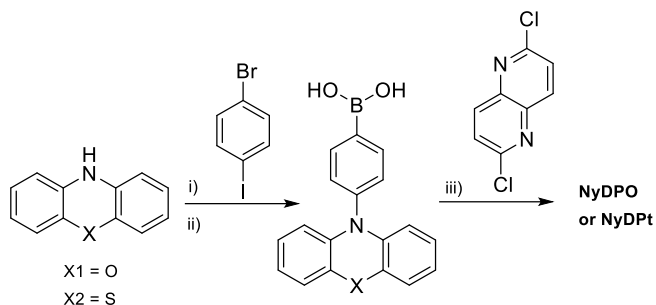
2.2.4. Device fabrication and measurements

The patterned indium-tin-oxide (ITO, 70 nm) substrates were washed with water and isopropyl alcohol, followed by 10 min

UV–ozone treatment. Organic layers, LiF, and Al were thermally evaporated at a deposition rate of 1–2 Å s⁻¹ for organic layers, 0.1 Å s⁻¹ for LiF, and 3–5 Å s⁻¹ for the Al electrode. OLED properties were measured using a Keithley source meter 2400 and a PR–650 spectrascan colorimeter.

2.2.5. Synthesis and characterization

Commercially available reagents and solvents were used without further purification unless otherwise noted. ¹H–spectra were recorded using an Agilent 400–MR DD2 400 MHz or Varian/Oxford As–500 500 MHz in CDCl₃ and DMSO–d₆. ¹H–NMR chemical shifts were referenced to CHCl₃ (7.26 ppm) and DMSO (2.50 ppm). ¹³C–NMR spectra could not be obtained because NyDPO and NyDPt have very low solubility in all NMR solvents. Mass spectra were recorded on a matrix–assisted laser desorption ionization time–of–flight (MALDI–TOF) Microflex instrument from Bruker. Elemental analysis (EA) data (Thermo Fisher Scientific, Flash2000) and high–resolution mass spectrometric (HRMS) data (JEOL, JMS–700) with fast atom bombardment (FAB) positive mode were received directly from the National Center for Inter–University Research Facilities (NCIRF).



i) $\text{CuSO}_4 \cdot 5\text{H}_2\text{O}$, K_2CO_3 , *o*-dichlorobenzene, reflux; ii) *n*-BuLi, trimethylborate, THF, $-78^\circ \text{C} \rightarrow \text{rt}$; iii) $\text{Pd}(\text{PPh}_3)_4$, K_2CO_3 , Toluene/ H_2O , reflux

Scheme 2-1. Synthetic routes for NyDPO and NyDPt

2.2.5.1. Synthesis of 10-(4-bromophenyl)-10*H*-phenoxazine.

A mixture of phenoxazine (200 mg, 1.09 mmol), 1-bromo-4-iodobenzene (339 mg, 1.20 mmol), $\text{CuSO}_4 \cdot 5\text{H}_2\text{O}$ (29 mg, 0.11 mmol) and K_2CO_3 (301 mg, 2.18 mmol) in *o*-dichlorobenzene (5 mL) was stirred at 180°C overnight. After cooling down to room temperature, the solvent was removed under reduced pressure and filtered through silica pad. The crude product was purified by column chromatography (SiO_2 , dichloromethane:hexane = 1:10) to afford compound 10-(4-bromophenyl)-10*H*-phenoxazine (255 mg, 69%) as a white solid. ^1H NMR (500 MHz, CDCl_3) δ 7.75 (d, $J = 8.4$ Hz, 2H), 7.26 (d, $J = 8.5$ Hz, 2H), 6.75 – 6.65 (m, 4H), 6.65 – 6.59 (m, 2H), 5.94 (d, $J = 7.8$ Hz, 2H).

2.2.5.2. Synthesis of 10-(4-bromophenyl)-10*H*-phenothiazine

A mixture of phenothiazine (2.0 g, 10 mmol), 1-bromo-4-iodobenzene (3.1 g, 11 mmol), CuSO₄·5H₂O (249 mg, 1.0 mmol) and K₂CO₃ (2.76 g, 20 mmol) in *o*-dichlorobenzene (20 mL) was stirred at 180°C overnight. After cooling down to room temperature, the solvent was removed under reduced pressure and filtered through silica pad. The crude product was purified by column chromatography (SiO₂, hexane only) to afford compound 10-(4-bromophenyl)-10*H*-phenothiazine (1.4 g, 40%) as a white solid. ¹H NMR (500 MHz, CDCl₃) δ 7.76 (d, J = 8.5 Hz, 2H), 7.32 (d, J = 8.5 Hz, 2H), 7.15 (dd, J = 7.4, 1.6 Hz, 2H), 6.96 (dd, J = 16.4, 8.8 Hz, 4H), 6.36 (d, J = 8.0 Hz, 2H).

2.2.5.3 Synthesis of (4-(10*H*-phenoxazin-10-yl)phenyl)boronic acid

*n*BuLi (11 mL, 17.7 mmol) was added dropwise to a solution of 10-(4-bromophenyl)-10*H*-phenoxazine (4.0 g, 11.8 mmol) in dry THF (60 mL) at -78°C under a nitrogen atmosphere. After the solution was stirred for 1 hour, trimethylborate (2.6 mL, 23.6 mmol) was added. The mixture was stirred at room temperature overnight. After 1N HCl solution was poured into the mixture, the organic phase was extracted with dichloromethane and washed with brine. The

crude product was precipitated using dichloromethane and hexane, which was used for the next step without further purification. MS (MALDI-TOF): calcd. for $C_{18}H_{14}BNO_3$ $[M]^+$: 303.1067; found: 303.032.

2.2.5.4. Synthesis of (4-(10*H*-phenothiazin-10-yl)phenyl)boronic acid

*n*BuLi (13 mL, 21.2 mmol) was added dropwise to a solution of 10-(4-bromophenyl)-10*H*-phenothiazine (5.0 g, 14.1 mmol) in dry THF (70 mL) at -78°C under a nitrogen atmosphere. After the solution was stirred for 1 hour, trimethylborate (3.1 mL, 28.2 mmol) was added. The mixture was stirred at room temperature overnight. After 1N HCl solution was poured into the mixture, and the organic phase was extracted with dichloromethane and washed with brine. The crude product was precipitated using dichloromethane and hexane, which was used for the next step without further purification. MS (MALDI-TOF): calcd. for $C_{18}H_{14}BNO_2S$ $[M]^+$: 319.0838; found: 319.075.

2.2.5.5. Synthesis of 2,6-bis(4-(10*H*-phenoxazin-10-yl)phenyl)-1,5-naphthyridine (NyDPO)

A mixture of 2,6-dichloro-1,5-naphthyridine (330 mg, 1.66

mmol), (4-(10*H*-phenoxazin-10-yl)phenyl)boronic acid (1.3 g, 4.32 mmol), Pd(PPh₃)₄ (196 mg, 0.17 mmol) and K₂CO₃ (917 mg, 6.64 mmol) in toluene (16 mL) and water (6 mL) was stirred at 100 °C overnight. After cooling down to room temperature, the solid was filtered and purified by recrystallization from chloroform and ethanol to afford NyDPO (967 mg, 90%) as a yellow solid. ¹H NMR (400 MHz, DMSO-*d*₆) δ 8.67 – 8.52 (m, 8H), 7.65 (d, *J* = 8.5 Hz, 4H), 6.81 – 6.75 (m, 4H), 6.74 – 6.67 (m, 8H), 6.04 – 5.97 (m, 4H). HRMS (FAB+): calcd for C₄₄H₂₈N₄O₂ [M]⁺: 644.2212; found: 644.2212. Elem. Anal.: calcd for C₄₄H₂₈N₄O₂ C 81.97, H 4.38, N 8.69; found C 82.15, H 4.48, N 8.58.

2.2.5.6. Synthesis of 2,6-bis(4-(10*H*-phenothiazin-10-yl)phenyl)-1,5-naphthyridine (NyDPt)

A mixture of 2,6-dichloro-1,5-naphthyridine (400 mg, 2.00 mmol), (4-(10*H*-phenothiazin-10-yl)phenyl)boronic acid (1.6 g, 5.01 mmol), Pd(PPh₃)₄ (231 mg, 0.20 mmol) and K₂CO₃ (1.4 g, 10.31 mmol) in toluene (20 mL) and water (10 mL) was stirred at 100 °C overnight. After cooling down to room temperature, the solid was filtered and purified by recrystallization from chloroform and ethanol to afford NyDPt (1.0 g, 74%) as a pale red solid. ¹H NMR (400 MHz, DMSO-*d*₆) δ 8.55 (dt, *J* = 18.7, 9.4 Hz, 8H), 7.56 (d, *J* = 8.6 Hz, 4H),

7.21 (dd, $J = 7.6, 1.5$ Hz, 4H), 7.11 – 7.02 (m, 4H), 6.97 (td, $J = 7.5, 1.1$ Hz, 4H), 6.53 (dd, $J = 8.1, 1.0$ Hz, 4H). HRMS (FAB+): calcd for $C_{44}H_{28}N_4S_2$ [M]⁺: 676.1755; found: 676.1760. Elem. Anal.: calcd for $C_{44}H_{28}N_4S_2$ C 78.08, H 4.17, N 8.28, S 9.47; found C 78.48, H 4.29, N 8.23, S 9.64.

2.3. Results and discussion

Table 2–1. Calculated data of NyDPO and NyDPt

Compound	θ_a ($^\circ$)	θ_b ($^\circ$)	HOMO (eV)	LUMO (eV)	E_{gap} (eV)	S_1 (eV)	T_1 (eV)	ΔE_{ST} (eV)
NyDPO	19	87	4.67	2.31	2.36	1.978	1.973	0.005
NyDPt [ax]	15	8	4.94	1.60	3.34	2.950	2.301	0.649
NyDPt [eq]	18	82	4.99	2.30	2.69	2.318	2.313	0.005

DFT calculations were performed to predict optimized molecular structures and electronic distributions of the frontier orbitals. Moreover, excited–state energies were evaluated by TD–DFT calculations. All calculations were carried out using Gaussian 09 software at the B3LYP/6–31G(d) level. Calculated data of NyDPO and NyDPt are presented in Figure 2–1 and summarized in Table 2–1. In Figure 2–1b, NyDPO showed a linear–shape molecular structure exhibiting dihedral angles θ_a and θ_b of 19° and 87° , respectively. Due to the highly distorted structure, the HOMO and

LUMO of NyDPO were well separated, resulting in a small ΔE_{ST} of 0.005 eV. According to references, the calculations of NyDPt were performed as the quasi-equatorial and quasi-axial forms.²⁰⁻²² The quasi-equatorial form showed dihedral angles θ_a of 18° and θ_b of 82° , similar to NyDPO. Thus, the quasi-equatorial form also showed well-separated orbital distributions between the HOMO and LUMO and a small ΔE_{ST} of 0.005 eV. However, the quasi-axial form showed dihedral angles θ_a of 15° and θ_b of 81° . Since θ_b of the quasi-axial form of NyDPt is much smaller compared with NyDPO and the quasi-equatorial form of NyDPt, the HOMO and LUMO were highly superimposed. The overlapped HOMO and LUMO of the quasi-axial form of NyDPt caused a large ΔE_{ST} of 0.6483 eV. Therefore, NyDPO and the quasi-equatorial form of NyDPt with small ΔE_{ST} values were expected to exhibit TADF.

All the synthetic details are described in the Experimental section. The synthesis of 2,6-dichloro-1,5-naphthyridine was previously reported.¹⁴ Phenoxazine and phenothiazine were cross-coupled to 1-bromo-4-iodobenzene through Ullmann coupling to give rise to the corresponding bromides,^{24, 25} which were then transformed into boronic acids. The boronic acids reacted with 2,6-dichloro-1,5-naphthyridine through Suzuki-Miyaura coupling to provide NyDPO and NyDPt.

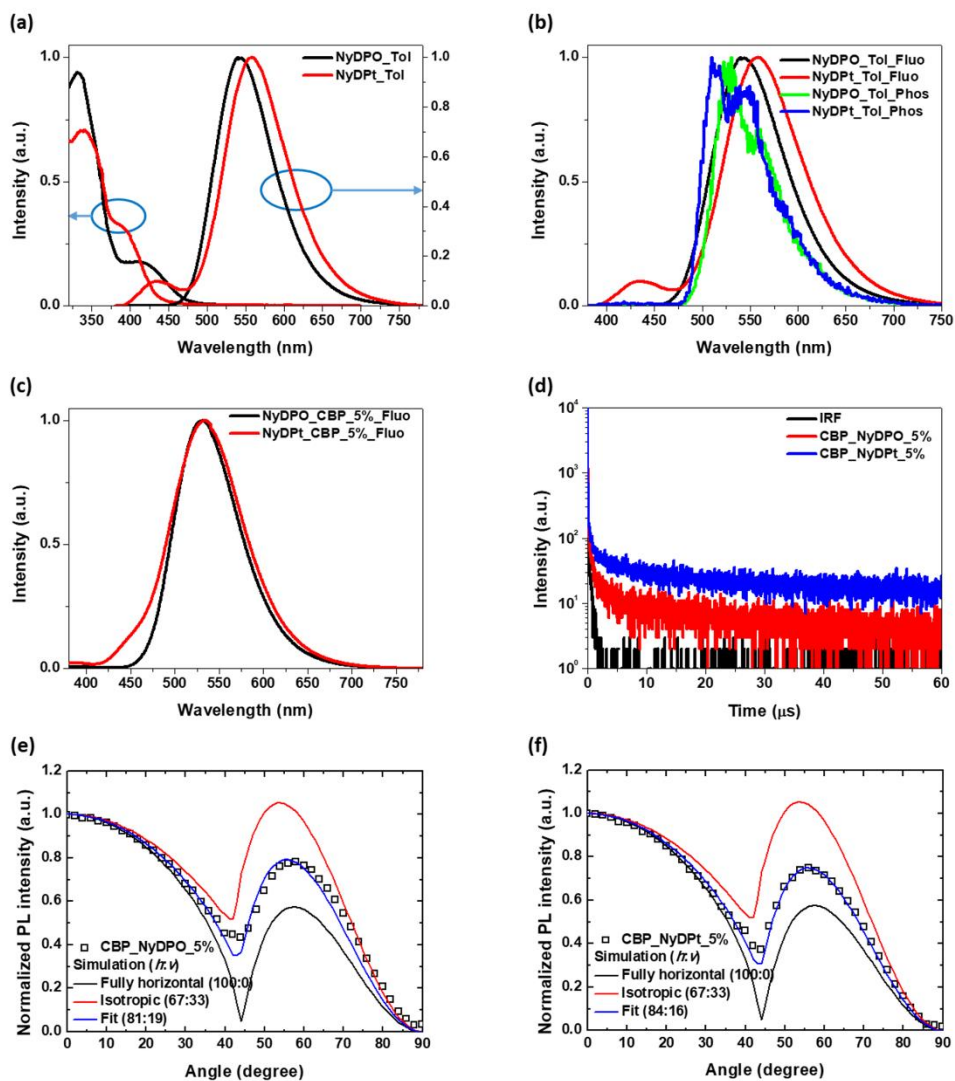


Figure 2-2. Photophysical properties of NyDPO and NyDPT. (a) UV/vis and PL in toluene solution (10^{-5} M), (b) fluorescence and phosphorescence spectra in toluene solution (10^{-5} M), (c) PL of the 5 wt% doped film in the CBP host, (d) transient PL of the 5 wt% doped film in the CBP host, and (e and f) angle-dependent PL of the 5 wt% doped films in the CBP host.

Table 2–2. Summarized properties of NyDPO and NyDPt.

Compound	$\lambda_{\text{Max}}^{(a)}$ (nm)	$\lambda_{\text{Max}}^{(b)}$ (nm)	$\Delta E_{\text{ST}}^{(c)}$ (eV)	$\Phi^{(d)}$ (%)	$\tau_1^{(e)}$ (ns)	$\tau_2^{(f)}$ (us)	$\theta_{//}^{(g)}$ (%)	HOMO ^(h) (eV)	LUMO ^(h) (eV)	$T_g^{(i)}$ (°C)	$T_d^{(j)}$ (°C)
NyDPO	540	530	0.09	79	22.4	11.29	81	5.06	2.88	–	435
NyDPt	433,558	533	0.59, 0.016	45	38.6	10.00	84	5.04	2.88	135	432

(a) Measured in toluene solution (10^{-5} M), (b) Measured in 5 wt% doped film in CBP host, (c) Energy difference between S_1 and T_1 , (d) Absolute photoluminescence quantum efficiency, (e) Lifetime of prompt decay, (f) Lifetime of delayed decay, (g) Horizontal emitting dipole ratio, (h) Estimated from the onset potentials ($^{\text{ox}}E_{\text{onset}}$ and $^{\text{red}}E_{\text{onset}}$ [eV] against Fc/Fc⁺ redox couple) in CV experiments, (i) Glass transition temperature, (j) Thermal decomposition temperature at 5% weight loss.

Table 2–3. Kinetic constants of NyDPO and NyDPt.

Compound	$\tau_{\text{PF}}^{(a)}$ (ns)	$\tau_{\text{TADF}}^{(b)}$ (us)	$\Phi_{\text{PF}}^{(c)}$ (%)	$\Phi_{\text{TADF}}^{(d)}$ (%)	$k_{\text{PF}}^{(e)}$ ($\times 10^7$)	$k_{\text{TADF}}^{(f)}$ ($\times 10^5$)	$k_{\text{IC}}^{(g)}$ ($\times 10^6$)	$k_{\text{ISC}}^{(h)}$ ($\times 10^6$)	$k_{\text{RISC}}^{(i)}$ ($\times 10^5$)
NyDPO	22.4	11.29	70	9	4.46	0.89	8.31	5.09	1.00
NyDPt	38.6	10.00	14.1	30.9	2.59	1.00	4.46	17.8	3.19

(a) Lifetime of prompt fluorescence, (b) Lifetime of delayed fluorescence, (c) PLQY of prompt fluorescence, (d) PLQY of delayed fluorescence, (e) Rate constant of prompt fluorescence, (f) Rate constant of delayed fluorescence, (g) Rate constant of internal conversion, (h) Rate constant of intersystem crossing, (i) Rate constant of reverse intersystem crossing.

To evaluate the photophysical properties of NyDPO and NyDPt, UV/vis absorption, PL, transient PL, and angle-dependent PL measurements were conducted in toluene solution or doped films using CBP as a host. The photophysical properties are presented in Figure 2-2 and summarized in Table 2-2. As shown in Figure 2-2a, NyDPO and NyDPt showed ICT absorption bands at 380–480 nm and 380–450 nm, respectively. Thus, both of them revealed charge transfer (CT) emission. In toluene, NyDPO only exhibited single emission with λ_{\max} at 540 nm, but NyDPt showed dual emission with λ_{\max} at 433 and 558 nm. With increasing solvent polarity, solvatochromic shifts were observed in the emission spectra of NyDPt (Figure S2-1). The dual emission of NyDPt at 433 and 558 nm corresponds to the CT emission of the quasi-axial form and quasi-equatorial form, respectively.²² As revealed in Figure 2-2a, the PL emission of NyDPt mainly comes from the quasi-equatorial form.

The energy levels of the singlet and triplet states were determined by room temperature and low temperature (77 K) PL measurements (Figure 2-2b). Each energy was calculated using the onset of the spectrum. NyDPO showed a ΔE_{ST} of 0.090 eV, which is sufficient to convert the triplet to the singlet state *via* reverse intersystem crossing.⁴ NyDPt showed a ΔE_{ST} of 0.59 eV and 0.016

eV in the quasi-axial and quasi-equatorial conformers, respectively. This suggests that only the quasi-equatorial form is sufficient to convert the triplet to the singlet state, resulting in TADF emission,⁴ while the quasi-axial conformation would not emit TADF and thus contributes to a decrease in the PLQY and device efficiency.

The PL spectra of 5 wt% doped films of NyDPO and NyDPt in CBP showed single and dual emission, respectively, as in the solution state (Figure 2-2c). The PL spectra of neat and doped films in CBP and DPEPO are also appended in Figure S2-2. NyDPO showed only single emission in both non-doped and doped films as in the solution state. However, in the case of NyDPt, the neat film only showed single emission unlike the doped films, because energy can be transferred from the quasi-axial form to the quasi-equatorial form due to the short intermolecular distance of NyDPt in the neat film.²⁰ The absolute PLQYs of the 5 wt% doped films of NyDPO and NyDPt in CBP were 79% and 45%, respectively. The much lower PLQY value of NyDPt in CBP should result from the existence of the quasi-axial conformer despite the strong electron-donating ability of phenothiazine.

The transient PL characteristics of the 5 wt% doped films of NyDPO and NyDPt in CBP confirmed the TADF property (Figure 2-2d). NyDPO showed a prompt component with a lifetime of 22.4 ns

and a delayed component with a lifetime of 11.29 μs . The lifetimes of the prompt and delayed component of NyDPt were 38.6 ns and 10.00 μs , respectively. The kinetic constants of NyDPO and NyDPt were calculated using a previously reported method (Table 2–3).^{26, 27} The k_{ISC} and k_{RISC} values of NyDPt are larger than those of NyDPO. The triplet consumptions associated with k_{ISC} and k_{RISC} are the crucial factor to improve the TADF device efficiency roll-off.²⁸ Therefore, considering only PL, NyDPt is expected to exhibit better device efficiency roll-off than NyDPO.

The ADPL measurements of NyDPO and NyDPt showed a horizontal dipole orientation of 81% and 84% in the 5% doped film using CBP as a host, respectively. These high horizontal EDOs were attributed to their overall linear molecular structures,¹² which could improve the light out-coupling efficiency. However, the 5 wt% doped films of NyDPO and NyDPt in CBP showed lower horizontal EDO than previously reported NyDPAc (92%) doped in DPEPO despite the overall structural similarity between the three emitters. To understand the difference in the horizontal EDO values, we also conducted ADPL measurements of NyDPAc doped in CBP, showing a lower horizontal EDO (84%) than the previously reported NyDPAc film doped in DPEPO (Figure S2–3). This was because host-dopant interactions vary depending on the host species.²⁹ In addition, the

glass transition temperature (T_g) and polarization of the host molecules are also known to affect the horizontal EDO.³⁰ This result implies that selecting an appropriate host can maximize the horizontal EDO of NyDPO and NyDPt.

To confirm the energy levels of NyDPO and NyDPt, CV was conducted. The HOMO/LUMO levels of NyDPO and NyDPt were calculated to be 5.06/2.88 and 5.04/2.88 eV, respectively (Figure S2-4). Thus, CBP (HOMO = 5.9 eV, LUMO = 2.7 eV) can be a suitable host for NyDPO and NyDPt. The thermal decomposition temperature (T_d) of NyDPO and NyDPt exceeded 430°C, and T_g of NyDPt was found to be 135°C (Figure S2-5 and S2-6), indicating their thermal stability.

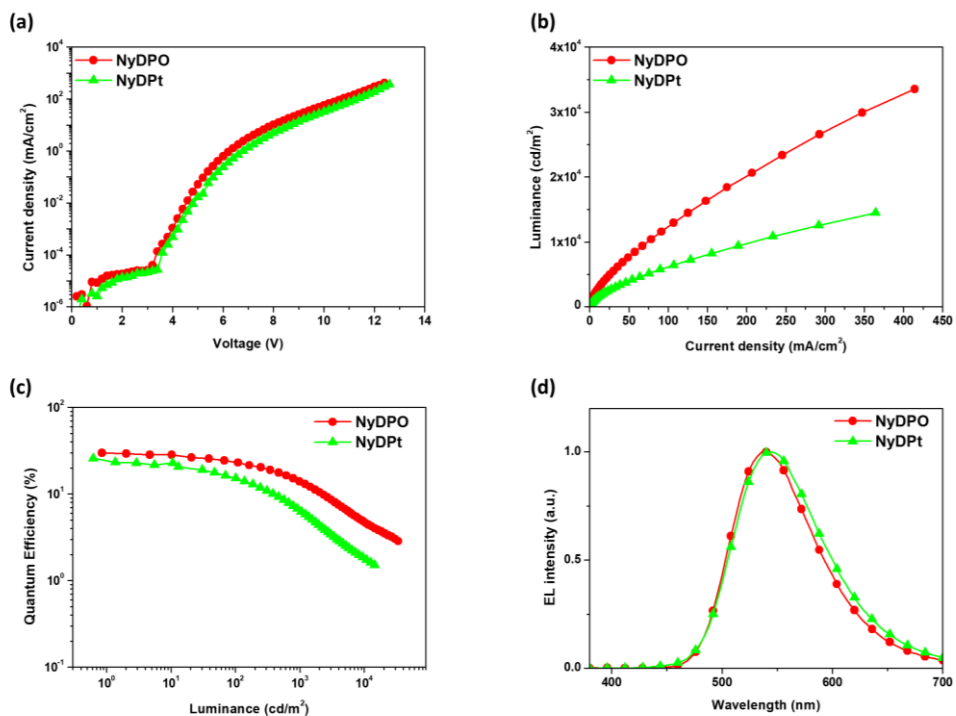


Figure 2-3. OLED characteristics of NyDPO- and NyDPt-based devices. (a) Voltage-current density (V-J) graph, (b) current density-luminance (J-L) graph, (c) luminance-quantum efficiency (J-QE) graph, and (d) emission spectra at 1000 cd m⁻².

Table 2–4. Summarized device data of NyDPO and NyDPt.

Compound	$V_{\text{on}}^{(a)}$ (V)	$\text{EQE}_{\text{max}}^{(b)}$ (%)	$\text{EQE}_{100}^{(c)}$ (%)	$\text{EQE}_{500}^{(d)}$ (%)	$\text{EQE}_{1000}^{(e)}$ (%)	$L_{\text{max}}^{(f)}$ (Cd/m ²)	$\lambda_{\text{Max}}^{(g)}$ (nm)	CIE ^(h)
NyDPO	4.0	29.9	23.1	17.6	14.0	33540	540	(0.36, 0.58)
NyDPt	4.2	25.8	15.2	9.3	6.3	14480	544	(0.38, 0.56)

(a) Turn on voltage, (b) Maximum EQE, (c) EQE at 100 cd m⁻², (d) EQE at 500 cd m⁻², (e) EQE at 1000 cd m⁻², (f) Maximum luminance, (g) EL emission wavelength at 1000 cd m⁻², (h) CIE 1931 color coordinates.

To verify the OLED characteristics of NyDPO and NyDPt, we fabricated a multilayer structure as follows: ITO (70 nm)/*N,N'*-bis(naphthalen-1-yl)-*N,N'*-bis(phenyl)benzidine (NPB, 50 nm)/1,3-di(9*H*-carbazol-9-yl)benzene (mCP, 10 nm)/CBP:emitter (5 wt%, 20 nm)/2,2',2''-(1,3,5-benzinetriyl)-tris(1-phenyl-1*H*-benzimidazole) (TPBi, 50 nm)/LiF (1 nm)/Al (100 nm). Device data are presented in Figure 2-3 and summarized in Table 2-4. The OLED device using NyDPO as an emitter showed an EQE of 29.9% and a maximum luminance of 33540 cd m⁻². The EQE and maximum luminance of the NyDPO-based devices are better than those of the NyDPAc-based devices.¹⁴ This is because phenoxazine is more strongly electron-donating than dimethylacridine so that the singlet energy level is forced to be close to the triplet state. Thus, NyDPO can reach a higher PLQY, resulting in a high EQE through more efficient triplet utilization than NyDPAc.

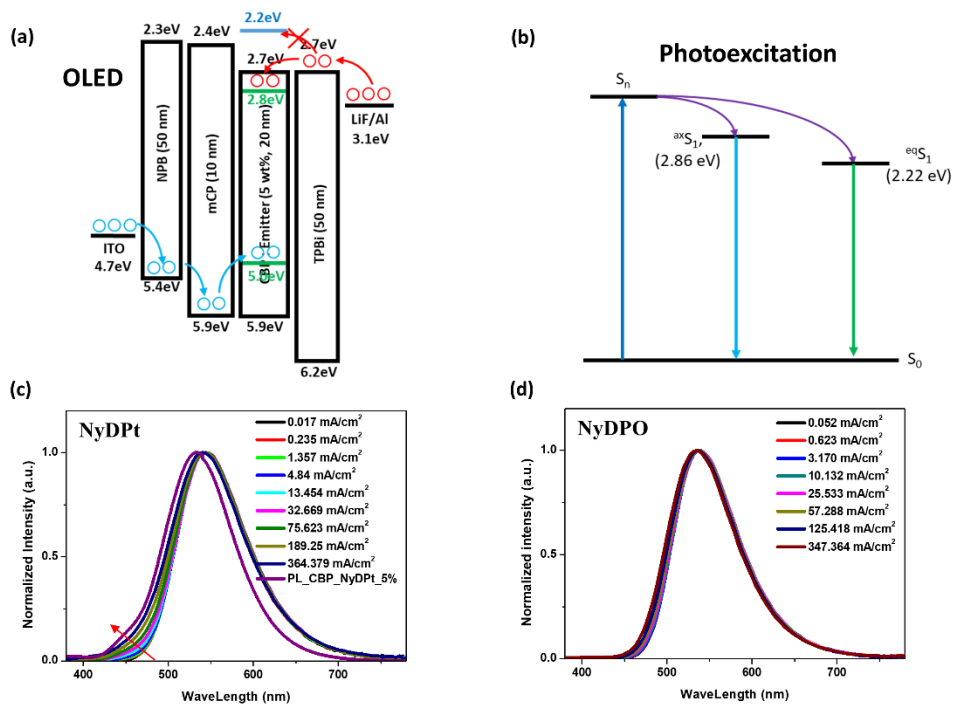


Figure 2-4. (a) Energy level diagram of NyDPt-based OLED devices (in the EML; green = quasi-equatorial form, sky blue = quasi-axial form), (b) energy level diagram of the photoexcitation process of NyDPt, (c) normalized EL and PL spectra of NyDPt, and (d) normalized EL spectra of NyDPO.

In particular, despite a relatively low PLQY of 45%, the NyDPt-based devices exhibited a high EQE of 25.8% and a maximum luminance of 14480 cd m⁻². To understand the unusual high EQE, the energy level diagrams of the OLED devices and photoexcitation process were drawn based on the previously reported energy levels of OLED materials³¹ and the HOMO (5.04 eV) and λ_{\max} values of the quasi-axial and equatorial forms (433 nm and 558 nm) of NyDPt (Figure 2-4a, b). In the photoexcitation process, electrons are excited from S₀ to S_n and then moved to ^{ax}S₁ and ^{eq}S₁ by internal conversion, resulting in dual emission (Figure 2-4b). Since both the quasi-axial and quasi-equatorial conformers are involved in PL, the PLQYs would be relatively reduced due to quasi-axial forms that cannot utilize triplet states. On the other hand, in the OLED process, holes and electrons move through their respective transporting layers and form excitons by recombination in the emitting layer (EML) (Figure 2-4a). Because electrons are injected into energy levels with low electron injection barriers,³² holes and electrons will form excitons in quasi-equatorial forms rather than in quasi-axial forms at low current densities. As shown in Figure 2-4c, only the quasi-equatorial CT emission was observed at low current densities. Due to the difference in the processes of generating the excited states by photoexcitation and electrical excitation, NyDPt could exhibit high

EQEs despite its low PLQYs. Moreover, the high EDO caused by the linear molecular shape further enhanced the EQE.

On the other hand, as the current density increases, electrons are accumulated and injected into the energy level of the quasi-axial form, which will result in dual emission by forming excitons in the quasi-axial and equatorial conformers. As shown in Figure 2-4c, with increasing current density, the emission increases in the short wavelength region, unlike the existing emission at low current density. NyDPO-based OLEDs having the same device structure only exhibited single emission with increasing current density (Figure 2-4d). Thus, it could be inferred that the dual emission was caused by NyDPt itself. In addition, if the emission of the quasi-axial conformation increases, the device efficiency will be significantly reduced because the triplet cannot be utilized in the quasi-axial form. Both NyDPO and NyDPt showed severe efficiency roll-off due to the intrinsic long TADF lifetime.^{4, 28} As shown in Figure 2-3c and Table 2-4, the efficiency roll-off of NyDPt was worse than that of NyDPO having low k_{ISC} and k_{RISC} . Therefore, the existence of the quasi-axial form is the major factor that lowers the performance of the device as the voltage increases.

2.4. Conclusion

In summary, we developed donor–acceptor–donor type TADF emitters NyDPO and NyDPt with 1,5–naphthyridine as an electron acceptor moiety and phenoxazine and phenothiazine as end–capped electron donor moieties. NyDPO and NyDPt exhibited high EDOs of 81% and 84%, which enhanced the light out–coupling efficiency. Moreover, the strong electron–donating ability of phenoxazine and phenothiazine and the overall structural distortion resulted in almost zero ΔE_{ST} values. Thus, NyDPO–based OLED devices showed a high EQE of 29.9% due to a high PLQY and horizontal EDO. NyDPt exhibited a low PLQY of 45% due to the influence of the quasi–axial form, but the maximum EQE of NyDPt–based OLED devices was 25.8% as the emission of the quasi–axial form was suppressed at low current density. Our results suggest that high–efficiency TADF emitters can be developed by using a linear molecular shape and by controlling dual emission.

2.5. References

1. Y. Lee and J.-I. Hong, *J. Mater. Chem. C*, 2020, 8, 8012–8017.
2. H.-W. Chen, J.-H. Lee, B.-Y. Lin, S. Chen and S.-T. Wu, *Light Sci. Appl.*, 2018, 7, 17168–17168.
3. A. Salehi, X. Fu, D.-H. Shin and F. So, *Adv. Funct. Mater.*, 2019, 29, 1808803.
4. Z. Yang, Z. Mao, Z. Xie, Y. Zhang, S. Liu, J. Zhao, J. Xu, Z. Chi and M. P. Aldred, *Chem. Soc. Rev.*, 2017, 46, 915–1016.
5. H. Uoyama, K. Goushi, K. Shizu, H. Nomura and C. Adachi, *Nature*, 2012, 492, 234–238.
6. S. Hirata, Y. Sakai, K. Masui, H. Tanaka, S. Y. Lee, H. Nomura, N. Nakamura, M. Yasumatsu, H. Nakanotani, Q. Zhang, K. Shizu, H. Miyazaki and C. Adachi, *Nat. Mater.*, 2015, 14, 330–336.
7. Y. Lee, S.-J. Woo, J.-J. Kim and J.-I. Hong, *Dyes Pigm.*, 2020, 172, 107864.
8. S. Jeong, Y. Lee, J. K. Kim, D.-J. Jang and J.-I. Hong, *J. Mater. Chem. C*, 2018, 6, 9049–9054.
9. K. Suzuki, S. Kubo, K. Shizu, T. Fukushima, A. Wakamiya, Y. Murata, C. Adachi and H. Kaji, *Angew. Chem. Int. Ed.*, 2015, 54, 15231–15235.
10. M. Kim, S. K. Jeon, S.-H. Hwang, S.-S. Lee, E. Yu and J. Y.

Lee, J. Phys. Chem. C, 2016, 120, 2485–2493.

11. T. Hosokai, H. Matsuzaki, H. Nakanotani, K. Tokumaru, T. Tsutsui, A. Furube, K. Nasu, H. Nomura, M. Yahiro and C. Adachi, Sci. Adv., 2017, 3, e1603282.

12. D. Yokoyama, J. Mater. Chem. A, 2011, 21, 19187–19202.

13. K. Saxena, V. K. Jain and D. S. Mehta, Opt. Mater., 2009, 32, 221–233.

14. Y. Lee, S.–J. Woo, J.–J. Kim and J.–I. Hong, Org. Electron., 2020, 78, 105600.

15. H. Tanaka, K. Shizu, H. Miyazaki and C. Adachi, ChemComm, 2012, 48, 11392–11394.

16. Y. Liu, G. Xie, K. Wu, Z. Luo, T. Zhou, X. Zeng, J. Yu, S. Gong and C. Yang, J. Mater. Chem. C, 2016, 4, 4402–4407.

17. M. Okazaki, Y. Takeda, P. Data, P. Pander, H. Higginbotham, A. P. Monkman and S. Minakata, Chem. Sci., 2017, 8, 2677–2686.

18. B. Wang, X. Qiao, Z. Yang, Y. Wang, S. Liu, D. Ma and Q. Wang, Org. Electron., 2018, 59, 32–38.

19. I. Marghad, F. Bencheikh, C. Wang, S. Manolikakes, A. Rérat, C. Gosmini, D. h. Kim, J.–C. Ribierre and C. Adachi, RSC Adv., 2019, 9, 4336–4343.

20. S. Xiang, R. Guo, Z. Huang, X. Lv, S. Sun, H. Chen, Q. Zhang and L. Wang, Dyes Pigm., 2019, 170, 107636.

21. H. Tanaka, K. Shizu, H. Nakanotani and C. Adachi, *J. Phys. Chem. C*, 2014, 118, 15985–15994.
22. M. K. Etherington, F. Franchello, J. Gibson, T. Northey, J. Santos, J. S. Ward, H. F. Higginbotham, P. Data, A. Kurowska, P. L. Dos Santos, D. R. Graves, A. S. Batsanov, F. B. Dias, M. R. Bryce, T. J. Penfold and A. P. Monkman, *Nat. Commun.*, 2017, 8, 14987.
23. P. L. dos Santos, M. K. Etherington and A. P. Monkman, *J. Mater. Chem. C*, 2018, 6, 4842–4853.
24. S.-H. Lee, C. T.-L. Chan, K. M.-C. Wong, W. H. Lam, W.-M. Kwok and V. W.-W. Yam, *J. Am. Chem. Soc.*, 2014, 136, 10041–10052.
25. C. Duan, J. Li, C. Han, D. Ding, H. Yang, Y. Wei and H. Xu, *Chem. Mater.*, 2016, 28, 5667–5679.
26. S. Oda, B. Kawakami, R. Kawasumi, R. Okita and T. Hatakeyama, *Org. Lett.*, 2019, 21, 9311–9314.
27. J. Lee, N. Aizawa, M. Numata, C. Adachi and T. Yasuda, *Adv. Mat.*, 2017, 29, 1604856.
28. K. Masui, H. Nakanotani and C. Adachi, *Org. Electron.*, 2013, 14, 2721–2726.
29. C.-K. Moon, K.-H. Kim, J. W. Lee and J.-J. Kim, *Chem. Mater.*, 2015, 27, 2767–2769.
30. M. Tanaka, H. Noda, H. Nakanotani and C. Adachi, *Appl. Phys.*

Lett., 2020, 116, 023302.

31. Y. Tao, C. Yang and J. Qin, Chem. Soc. Rev., 2011, 40, 2943–2970.

32. C.-T. Sun, I.-H. Chan, P.-C. Kao and S.-Y. Chu, J. Electrochem. Soc, 2011, 158, H1284–H1288.

2.6. Supplementary data

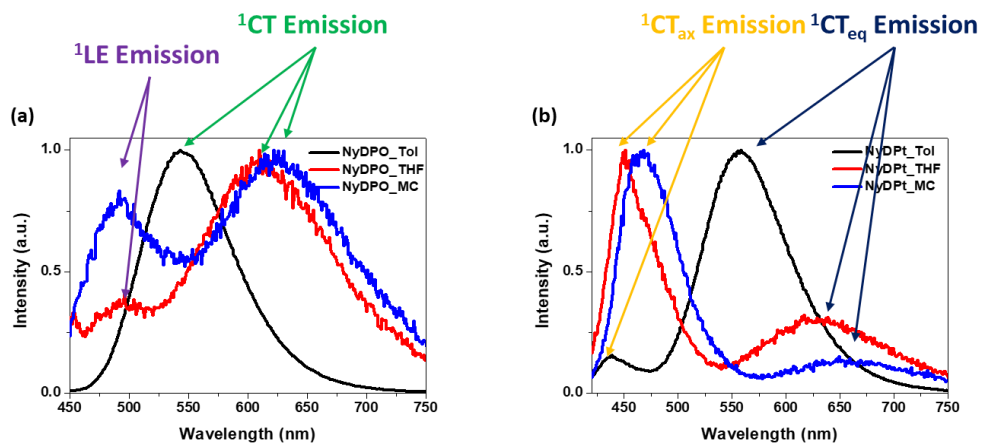


Figure S2-1. Effects of solvent polarity on PL spectra of (a) NyDPO and (b) NyDPt.

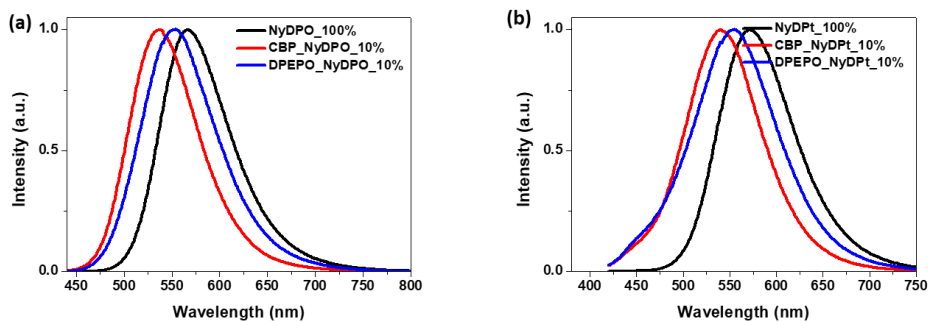


Figure S2-2. PL spectra of neat film and doped film. (a) NyDPO and (b) NyDPt.

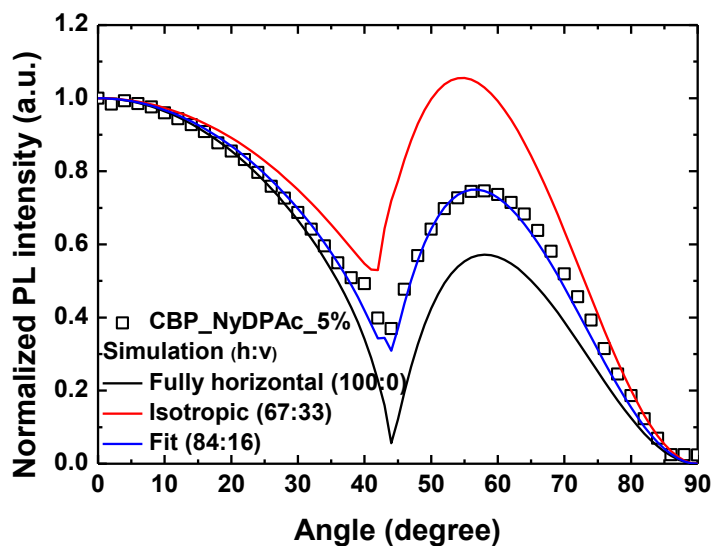


Figure. S2-3. Angle-dependent PL spectra of 5 wt% doped film of NyDPAc in CBP.

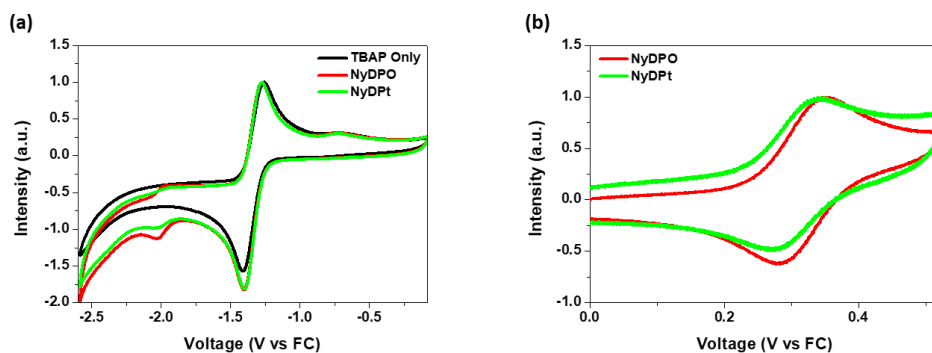


Figure. S2-4. Cyclic voltammograms of NyDPO and NyDPt. (a) reduction and (b) oxidation.

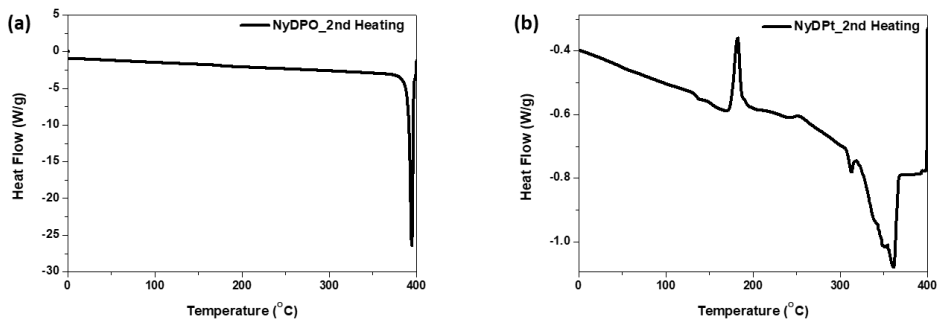


Figure S2-5. DSC thermograms of (a) NyDPO and (b) NyDPt.

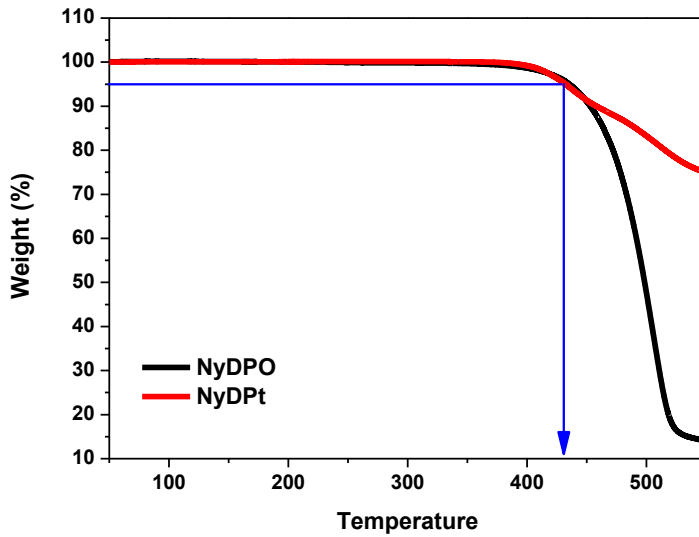


Figure S2-6. TGA thermograms of NyDPO and NyDPt.

Chapter 3. High-Efficiency Thermally
Activated Delayed Fluorescence Emitters with
High Horizontal Orientation and Narrow Deep-
Blue Emission

Chapter 3. High-Efficiency Thermally Activated Delayed Fluorescence Emitters with High Horizontal Orientation and Narrow Deep-Blue Emission

A part of this section was published in *Advanced Optical Materials*.¹

3.1. Introduction

Thermally activated delayed fluorescence (TADF) emitters significantly improve the internal quantum efficiency (IQE) of organic light-emitting diodes (OLEDs), because TADF molecules can harvest both singlet and triplet excitons through efficient reverse intersystem crossing (RISC), which is not available in conventional fluorescent materials.^{2, 3} TADF molecules based on twisted electron donor-acceptor geometries can effectively reduce the energy difference between the lowest singlet and triplet excited states (ΔE_{ST}). Therefore, the triplet state can be converted to the singlet state using the surrounding thermal energy, thus enabling 100% IQE.

Strong electron donors and electron acceptors facilitate the separation of the highest occupied molecular orbital (HOMO) and lowest unoccupied molecular orbital (LUMO), resulting in a small ΔE_{ST} .⁴ Thus, in general, TADF emitters with strong charge-transfer (CT) characters showed evident TADF emissions and high

photoluminescence (PL) quantum yields (PLQYs) compared to those of the emitters with weak CT characters. Blue TADF emitters require a wide energy difference between the HOMO and LUMO (E_{gap}), which can be achieved by a weak electron donor and electron acceptor. Therefore, the development of high-efficiency blue TADF emitters is quite challenging. Although many blue TADF emitters with high efficiencies have been reported,⁵⁻⁷ to the best of our knowledge, there have been no examples of deep-blue TADF emitters (Commission Internationale de l'Éclairage (CIE) $y < 0.1$) with a maximum external quantum efficiency (EQE) of over 30%. The development of highly efficient deep-blue TADF emitters requires consideration of factors, such as the optimum emission wavelength, narrow full width at half maximum (FWHM), and molecular orientation effects, which can be achieved by choosing appropriate electron donors and acceptors along with the overall conformational rigidity and linear molecular shape of the emitters.

In general, CT-based TADF molecules have a high degree of freedom in the excited state, resulting in a wide FWHM and thus poor color purity.⁸ The poor color purity of most TADF emitters limits their application in commercial OLEDs, despite their high efficiency. Therefore, in developing TADF emitters, researchers must consider not only the efficiency but also the color purity. The narrow FWHM

is usually achieved by exploiting the reduced conformational flexibility or multiple resonance effects of boron and nitrogen atoms.⁷

9, 10

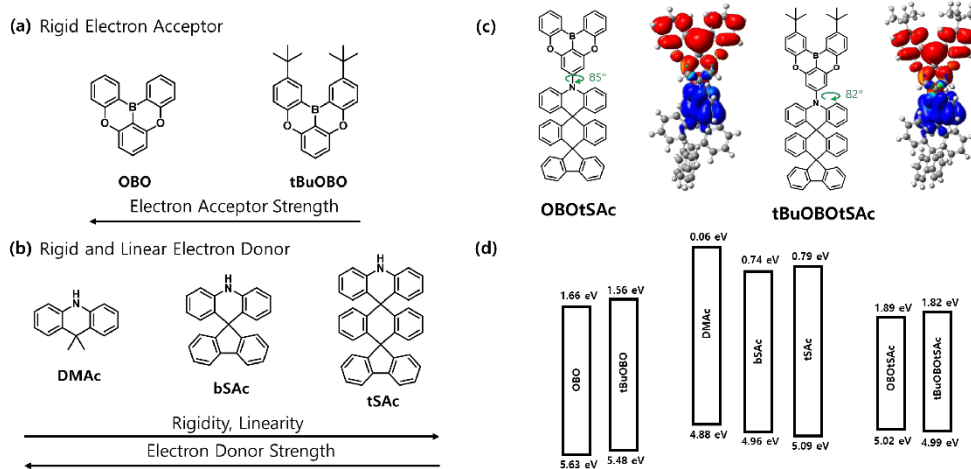


Figure 3-1. a) Molecular structures of OBO and tBuOBO. b) Molecular structures of DMAc, bSAc, and tSAc. c) Molecular structures and orbital distributions of OBOtSAc and tBuOBOtSAc (blue: HOMO, red: LUMO). d) Calculated HOMO and LUMO values of OBO, tBuOBO, DMAc, bSAc, tSAc, OBOtSAc, and tBuOBOtSAc

To realize deep-blue emissions, the electron donor and acceptor units must be carefully selected. Recently, there have been reports on B-doped, B,N-doped, and B,O-doped polycyclic aromatic hydrocarbons.¹¹⁻¹³ Among them, B,O-containing naphthoanthracene, 5,9-dioxa-13*b*-boranaphtho[3,2,1-*de*]anthracene (OBO, Figure 3-1a), is rigid and has a shallow LUMO energy and large triplet energy (E_T), induced by the combination of boron and oxygen atoms; thus, it has been used as an excellent electron acceptor for blue emission.^{10, 14} Moreover, if a *tert*-butyl group with electron-donating ability is introduced into OBO, the LUMO energy level of 2,12-di-*tert*-butyl-5,9-dioxa-13*b*boranaphtho[3,2,1-*de*]anthracene (tBuOBO, Figure 3-1a) will be further increased (becomes shallower), which is more advantageous for deep-blue emission.

Numerous TADF emitters using dimethylacridine (9,9-dimethyl-9,10-dihydroacridine, DMAc) as an electron donor have been developed.¹⁵⁻¹⁸ DMAc is suitable for inducing TADF by separating the HOMO and LUMO of the electron donor (DMAc)-acceptor-type emitters because of the steric hindrance between the hydrogen atoms at the fourth and fifth positions of DMAc and an adjacent aromatic linker or electron acceptor group. However, the

electron-donating ability of DMAc itself is too strong to allow for deep-blue emission, because the sp^3 hybridized gem-dimethyl group strengthens the electron-donating ability through hyperconjugation. In addition, the gem-dimethyl moiety of DMAc increases the conformational degree of freedom, resulting in nonradiative decay pathways of the excited states. A recent study showed that the modification of DMAc to bi-spiral acridine (bSAc, Figure 3-1b) weakens the hyperconjugative electron-donating effect, thus lowering the HOMO energy and increasing the conformational rigidity.¹⁵ Consequently, the emission wavelength is blue-shifted, and PLQY is improved. Therefore, a further rigidified tri-spiral acridine (tSAc, Figure 3-1b) type electron donor is expected to induce deep-blue emission with improved PLQY due to the weaker hyperconjugative electron-donating effect of tSAc than that of bSAc.

Since the light from the emitting layer (EML) of OLED devices passes through the glass substrate, the amount of light emitted to the outside is limited.¹⁹ Therefore, to increase the OLED EQEs, both the IQE and out-coupling efficiency must be considered. Fluorophores emit light perpendicularly to the dipole.²⁰ Therefore, if emitting dipoles are aligned horizontally, the out-coupling efficiency will increase. Recent studies have shown that molecules with linear or planar anisotropic shapes are arranged horizontally on the

substrate.^{20–23} Thus, a linearly extended tSAC as an electron donor would improve the outcoupling efficiency of TADF molecules, resulting in increased EQEs.

Herein, we report two TADF emitters, 10-(5,9-dioxa-13*b*-boranaphtho[3,2,1-*de*]anthracen-7-yl)-10*H*-dispiro[acridine-9,9'-anthracene-10',9''-fluorene] (OBOtSAC) and 10-(2,12-di-*tert*-butyl-5,9-dioxa-13*b*-boranaphtho[3,2,1-*de*]anthracen-7-yl)-10*H*-dispiro[acridine-9,9'-anthracene-10',9''-fluorene] (tBuOBOtSAC) (Figure 3-1c). The highly distorted geometries of an OBO electron acceptor and a tSAC electron donor with conformational rigidity, long linear molecular shapes, and appropriate electron-donating/accepting ability of the two emitters resulted in highly efficient deep-blue TADF emission due to the narrow FWHM values of 50 and 48 nm, respectively, high degrees of horizontal orientation of transition dipole moments (with 88% and 90% of dipoles horizontally oriented), and high PLQYs of 97% and 90%, respectively. Consequently, OLED devices based on OBOtSAC and tBuOBOtSAC emitters exhibited a maximum EQE of 31.2% with a CIE *y* coordinates of 0.092 and a maximum EQE of 28.2% with a CIE *y* coordinates of 0.061.

3.2. Experimental section

3.2.1. Quantum chemical calculations

Density functional theory (DFT) calculations were performed to predict optimized molecular structures and orbital distributions of frontier orbitals. Time-dependent density functional theory (TD-DFT) calculations were performed to estimate energies of excited states. All calculations were employed using Gaussian 09 software at the B3LYP/6-31G(d) level.

3.2.2 Photophysical property analysis

Ultraviolet-visible (UV-vis) spectra were recorded on a Jasco V-730 spectrophotometer. Fluorescence and phosphorescence spectra were recorded on a Jasco FP-8300 spectrophotometer. Absolute quantum efficiency was obtained with a PTI QuantaMaster 40 spectrofluorometer using a 3.2 in. integrating sphere at room temperature. Transient PL was measured through the time-correlated single-photon counting (TCSPC) techniques by using a PicoQuant, FluoTime 250 instrument. A 377 nm pulsed laser was used as an excitation source. The angle-dependent PL (ADPL) measurements and analyses of horizontal dipole ratios were performed using an integrated angle-dependent spectrometer and its built-in simulator (JALS; JooAm). A 365-nm UV lamp served as an

excitation source. PL emissions were detected over the range of -90° to $+90^\circ$ in 2° increments. The analyses were performed at the peak wavelength of each sample. Only p-polarized light was detected for analysis. The horizontal dipole ratio was determined by fitting the measured angle-dependent intensity profile.

3.2.3. Electrochemical and thermal analysis

Cyclic voltammetry (CV) experiments were conducted in DMF solution (1.00 mM) with 0.1 M tetra-*n*-butylammonium perchlorate (TBAP) as the supporting electrolyte. A glassy carbon electrode was employed as the working electrode and referenced to an Ag reference electrode. All potential values were calibrated against the ferrocene/ferrocenium (Fc/Fc⁺) redox couple. The onset potential was determined from the intersection of two tangents drawn at the rising and background current of the cyclic voltammogram. Differential scanning calorimetry (DSC) and thermogravimetric analysis (TGA) were performed with a TA instrument DSC Q10 and TGA Q50 in a nitrogen atmosphere at a heating rate of $10^\circ\text{C min}^{-1}$.

3.2.4. Device fabrication and measurements

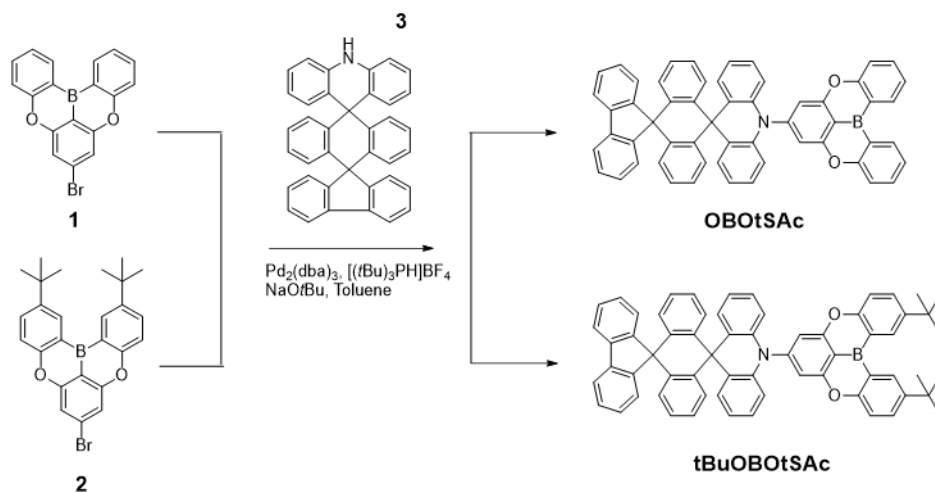
The patterned indium-tin-oxide (ITO, 70 nm) substrates were washed with water and isopropyl alcohol, followed by 10 min

UV–ozone treatment. Organic layers, LiF, and Al were thermally evaporated at a deposition rate of 1–2 Å s⁻¹ for organic layers, 0.1 Å s⁻¹ for LiF, and 3–5 Å s⁻¹ for the Al electrode. OLED properties were measured using a Keithley source meter 2400 and a PR–650 spectrascan colorimeter.

3.2.5. Synthesis and characterization

Commercially available reagents and solvents were used without further purification unless otherwise noted. Compounds 1, 2, and 3 were synthesized by following previously reported references. ¹H– and ¹³C–spectra were recorded using a Varian/Oxford As–500 500 MHz in CDCl₃. ¹H–NMR chemical shifts were referenced to CHCl₃ (7.26 ppm). ¹³C–NMR chemical shifts in CDCl₃ were reported relative to CHCl₃ (77.23 ppm). Elemental analysis (EA) data (Thermo Fisher Scientific, Flash2000) and high–resolution mass spectrometric (HRMS) data (JEOL, JMS–700) with fast atom bombardment (FAB) positive mode were received directly from the National Center for Inter–University Research Facilities (NCIRF).

3.2.5.1. Synthesis of 10–(5,9–dioxo–13*b*–boranaphtho[3,2,1–de]anthracen–7–yl)–10*H*–dispiro[acridine–9,9'–anthracene–10',9''–fluorene] (OBOtSAc)



Scheme 3–1. Synthetic routes for OBotSAc and tBuOBtSAc.

A mixture of **1** (523 mg, 1.50 mmol) and **3** (500 mg, 1.01 mmol) were fully dissolved in hot toluene (500 mL). After the reaction mixture was cooled to room temperature, tris(dibenzylideneacetone)dipalladium(0) (45 mg, 0.05 mmol), tris-*tert*butylphosphine/HBF₄ (29 mg, 0.10 mmol), and NaOtBu (192 mg, 2.00 mmol) were added to the mixture. Then, the reaction mixture was degassed with nitrogen atmosphere and stirred at 100°C for 24 h. The reaction mixture was filtered with silica using hot toluene and chloroform. After the solvent was evaporated, the crude product was purified by recrystallization from chloroform and ethanol to afford OBotSAc (570 mg, 75%) as a yellow solid. ¹H NMR (500 MHz, CDCl₃, δ): 8.80 (d, J = 7.9 Hz, 2H), 7.92 (d, J = 8.1 Hz, 2H), 7.79 (s, 2H), 7.63 (d, J = 8.7 Hz, 2H), 7.48 (dd, J = 27.4, 13.2 Hz, 8H), 7.29 (s, 4H), 7.18 – 7.04 (m, 4H), 6.96 (s, 2H), 6.83 (s, 4H), 6.54 (d, J = 7.7

Hz, 2H), 6.41 (d, $J = 7.7$ Hz, 2H); HRMS (FAB+) m/z : $[M]^+$ calcd for $C_{56}H_{34}BNO_2$: 763.2683; found: 763.2683. Anal. calcd for $C_{56}H_{34}BNO_2$: C 88.07, H 4.49, N 1.83; found: C 88.19, H 4.48, N 1.84.

3.2.5.2. Synthesis of 10-(2,12-di-*tert*-butyl-5,9-dioxa-13*b*-boranaphtho[3,2,1-*de*]anthracen-7-yl)-10*H*-dispiro[acridine-9,9'-anthracene-10',9''-fluorene] (tBuOBOTsAc)

A mixture of 2 (627 mg, 1.36 mmol) and 3 (450 mg, 0.91 mmol) were fully dissolved in hot toluene (450 mL). After the reaction mixture was cooled to room temperature, tris(dibenzylideneacetone)dipalladium(0) (41 mg, 0.045 mmol), tri-*tert*butylphosphine/ HBF_4 (26 mg, 0.09 mmol), and NaOtBu (173 mg, 1.80 mmol) were added to the mixture. Then, the reaction mixture was degassed with nitrogen atmosphere and stirred at 100°C for 24 h. The reaction mixture was filtered with silica using hot toluene and chloroform. After the solvent was evaporated, the crude product was purified by recrystallization from chloroform and ethanol to afford tBuOBOTsAc (360 mg, 52%) as a yellow solid. 1H NMR (500 MHz, $CDCl_3$, δ): 8.84 (s, 2H), 7.92 (d, $J = 8.0$ Hz, 2H), 7.85 (d, $J = 8.8$ Hz, 2H), 7.57 (d, $J = 8.7$ Hz, 2H), 7.51 (d, $J = 8.0$ Hz, 2H), 7.43 (s, 4H), 7.29 (s, 4H), 7.14 (d, $J = 7.8$ Hz, 2H), 7.08 (s, 2H), 6.95 (d, $J = 7.7$ Hz, 2H), 6.83 (s, 4H), 6.54 (d, $J = 8.3$ Hz, 2H), 6.40 (d, $J = 8.4$ Hz,

2H), 1.53 (s, 18H); ^{13}C NMR (125 MHz, CDCl_3 , δ): 159.62, 158.78, 157.82, 146.79, 145.49, 145.00, 140.51, 139.38, 134.43, 132.01, 131.91, 131.86, 131.17, 130.34, 128.56, 128.06, 127.51, 127.39, 126.75, 126.40, 125.47, 120.93, 120.00, 118.08, 114.82, 111.09, 58.08, 48.72, 34.63, 31.57; HRMS (FAB+) m/z : $[\text{M}]^+$ calcd for $\text{C}_{64}\text{H}_{50}\text{BNO}_2$: 875.3935; found: 875.3927; Anal. calcd for $\text{C}_{56}\text{H}_{34}\text{BNO}_2$: C 87.76, H 5.75, N 1.60; found: C 87.71, H 5.76, N 1.62.

3.3. Results and discussion

Table 3–1. Calculated data

Compound	HOMO [eV]	LUMO [eV]	E_{gap} ^{a)} [eV]	E_{S} ^{b)} [eV]	E_{T} ^{c)} [eV]	ΔE_{ST} ^{d)} [eV]
OBO	5.63	1.66	3.97	3.425	2.903	0.522
tBuOBO	5.48	1.56	3.92	3.390	2.860	0.530
DMAc	4.88	0.06	4.82	3.779	3.189	0.590
bSAc	4.96	0.74	4.22	3.613	3.049	0.564
tSAc	5.09	0.79	4.29	3.600	3.036	0.564
OBOtSAc	5.02	1.89	3.13	2.628	2.621	0.007
tBuOBOtSAc	4.99	1.82	3.17	2.664	2.657	0.007

^{a)} Energy difference between the HOMO and LUMO; ^{b)} Lowest singlet energy; ^{c)} Lowest triplet energy; ^{d)} Energy difference between E_{S} and E_{T} .

The optimized molecular structures and frontier orbitals were estimated using DFT calculations (B3LYP/6–31G(d)). Singlet and triplet energies were evaluated using TD–DFT calculations (B3LYP/6–31G(d) for OBO, tBuOBO, DMAc, bSAc, and tSAc or

MPW1B95/6-31G(d,p) for OBOtSAc and tBuOBOtSAc). All calculations were performed using the Gaussian 09 software. The calculation results are shown in Figure 3-1 and summarized in Table 3-1. tBuOBO possesses a higher LUMO level than OBO because of the electron-donating *tert*-butyl group (Figure 3-1d). The structural modification from DMAc to tSAc lowers the HOMO level as the hyperconjugation effect decreases (Figure 3-1d). OBOtSAc and tBuOBOtSAc exhibit distorted molecular structures with twist angles of 85° and 82° (Figure 3-1c), respectively. Owing to the highly distorted structure, the HOMO and LUMO of both molecules are separated (Figure 3-1c). Consequently, the ΔE_{ST} values of OBOtSAc and tBuOBOtSAc are significantly smaller than those of OBO, tBuOBO, and tSAc. Figure 3-1d shows the calculated HOMO and LUMO energies of the electron donors and acceptors, OBOtSAc and tBuOBOtSAc.

The detailed synthesis procedure is described in the Experimental section. OBOtSAc and tBuOBOtSAc were synthesized through the Buchwald-Hartwig coupling between brominated OBO (1) (or brominated tBuOBO (2)) and tSAc (3), and purified twice by vacuum thermal sublimation. OBOtSAc and tBuOBOtSAc were characterized by ¹H-NMR, ¹³C-NMR, mass spectrometry, and elemental analyses. The ¹³C-NMR spectra of OBOtSAc could not be

obtained because of the low solubility of all the NMR solvents

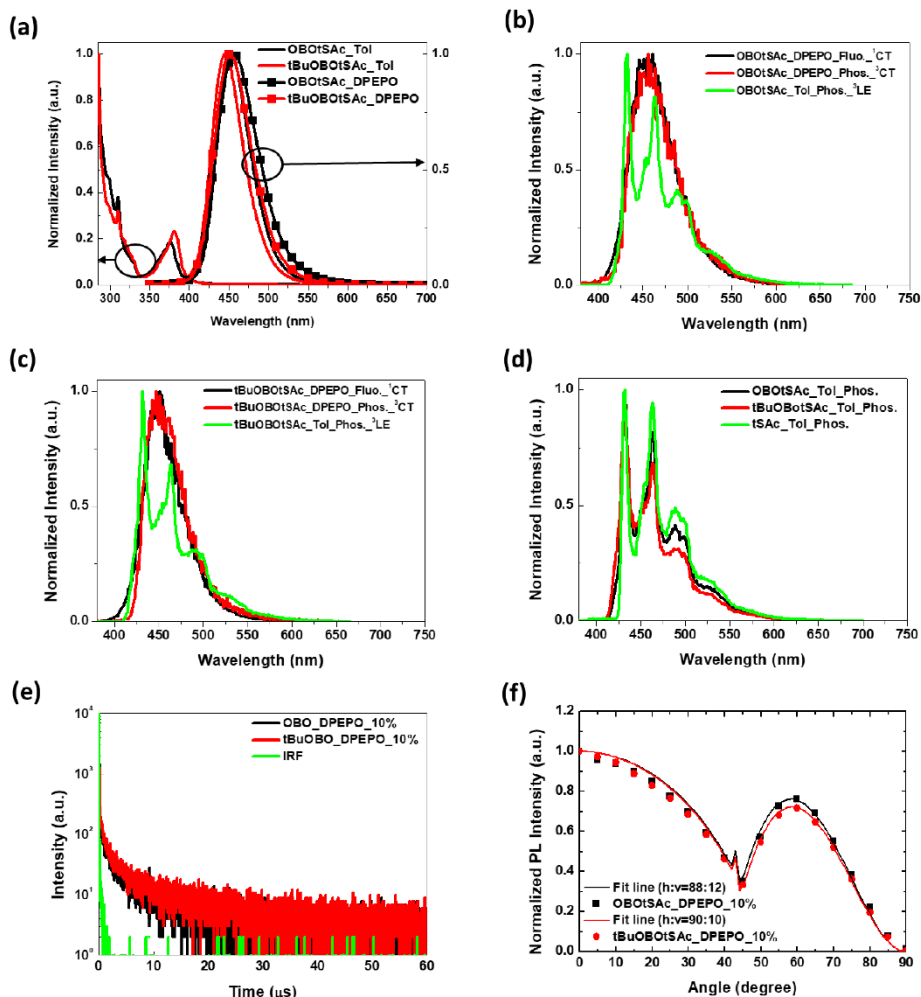


Figure 3-2. Photophysical properties in toluene (10^{-5} M) and 10 wt% doped films in the DPEPO host. a) UV-vis and PL. b) Fluorescence and phosphorescence spectra of OBOtSAc. c) Fluorescence and phosphorescence spectra of tBuOBOtSAc. d) Phosphorescence spectra of OBOtSAc, tBuOBOtSAc, and tSAc in toluene. e) Transient PL of 10 wt% doped films in the DPEPO host. f) Angle-dependent PL of 10 wt% doped films in the DPEPO host.

Table 3–2. Physical properties of OBOtSAc and tBuOBOtSAc

Compound	$\lambda_{\max}^{\text{a)/b)}$ [nm]	$^1\text{CT}^{\text{b)}$ [eV]	$^3\text{CT}^{\text{b)}$ [eV]	$^3\text{LE}^{\text{a)}$ [eV]	$\Delta E_{\text{ST}}^{\text{c)}$ [eV]	$\theta_{//}^{\text{d)}$ [%]	HOMO ^{e)} [eV]	LUMO ^{f)} [eV]	$T_g^{\text{g)}$ [° C]	$T_d^{\text{h)}$ [° C]
OBOtSAc	452/454	2.995	2.938	2.988	0.057	88	5.36	2.21	–	446
tBuOBOtSAc	446/450	3.024	2.945	2.988	0.079	90	5.35	2.20	–	456

^{a)} Measured in toluene (10^{-5} M); ^{b)} Measured in 10 wt% doped films in the DPEPO host; ^{c)} Energy difference between ^1CT and ^3CT ; ^{d)} Horizontal orientation; ^{e)} Estimated from the onset potentials in CV experiments; ^{f)} HOMO + optical energy gap; ^{g)} Glass transition temperature; ^{h)} Thermal decomposition temperature at 5 wt% weight loss.

Table 3–3. PLQYs, lifetimes, and rate constants of OBOtSAc and tBuOBOtSAc

Compound	$\Phi^{\text{a)}$ [%]	$\Phi_{\text{PF}}^{\text{b)}$ [%]	$\Phi_{\text{TADF}}^{\text{c)}$ [%]	$\tau_{\text{PF}}^{\text{d)}$ [ns]	$\tau_{\text{TADF}}^{\text{e)}$ [μs]	$k_{\text{PF}}^{\text{f)}$ [$\times 10^7$]	$k_{\text{TADF}}^{\text{g)}$ [$\times 10^5$]	$k_{\text{RISC}}^{\text{h)}$ [$\times 10^5$]
OBOtSAc	97	60	37	32.2	2.92	1.84	3.44	5.59
tBuOBOtSAc	90	50	40	28.8	3.81	1.73	2.62	4.74

^{a)} Absolute PLQY; ^{b)} PLQY of prompt fluorescence; ^{c)} PLQY of delayed fluorescence; ^{d)} Lifetime of prompt fluorescence; ^{e)} Lifetime of delayed fluorescence; ^{f)} Rate constant of prompt fluorescence; ^{g)} Rate constant of delayed fluorescence; ^{h)} Rate constant of reverse intersystem crossing.

The solution- and film-state photophysical properties were evaluated by UV-vis absorption and PL, TCSPC, and ADPL measurements. The photophysical properties of the two emitters in the solution and film states are shown in Figure 3-2 and summarized in Tables 3-2, 3. The UV-vis absorption maximum peaks in toluene were observed at 375 and 309 nm for OBOtSAC, and 380 and 309 nm for tBuOBOtSAC. The maximum emission wavelengths (λ_{\max}) of OBOtSAC and tBuOBOtSAC appeared at 452 and 446 nm, respectively. The emission wavelengths of OBOtSAC and tBuOBOtSAC shifted to a green region with increasing solvent polarity, indicating their CT characteristics (Figure S3-1). In particular, with increasing solvent polarity from toluene to tetrahydrofuran (THF) and dichloromethane, OBOtSAC showed larger redshifts of 39 and 47 nm compared to the shifts of 36 and 46 nm for tBuOBOtSAC, indicating that OBOtSAC has a stronger CT character than tBuOBOtSAC, as expected. The FWHM values of OBOtSAC and tBuOBOtSAC were estimated to be 50 and 48 nm, respectively, which are narrower than those of most known TADF emitters.⁸

The films of 10 wt% doped in a bis[2-(diphenylphosphino)phenyl] ether oxide (DPEPO) host were fabricated by the thermal evaporation. Since the lowest triplet energies of OBOtSAC and tBuOBOtSAC are 2.938 and 2.945 eV,

DPEPO with a triplet energy of 3.0 eV was used as the host to fully confine the triplet states of the emitters.²⁴ The emission maximum wavelengths of OBOtSAC and tBuOBOtSAC appeared at 454 and 450 nm, respectively, which are slightly redshifted by the solvatochromic effect due to the polar nature of DPEPO, and the absolute PLQYs were 97% and 90%, respectively

The probability of TADF was investigated by the fluorescence and phosphorescence of the emitters in the solution and film state at room and low temperatures (77 K) (Figure 3-2b, c). In high-polarity DPEPO, the fluorescence and phosphorescence of OBOtSAC and tBuOBOtSAC showed a singlet charge-transfer state (¹CT) and triplet charge-transfer state (³CT). The ¹CT and ³CT energies of OBOtSAC were 2.995 and 2.938 eV, respectively, and the ¹CT and ³CT energies of tBuOBOtSAC were 3.024 and 2.945 eV, respectively. Therefore, the ΔE_{ST} values of the 10 wt% doped films of OBOtSAC and tBuOBOtSAC in DPEPO were 0.057 and 0.079 eV, respectively. However, in frozen low-polarity toluene ($T_m = 178$ K) at 77 K, both OBOtSAC and tBuOBOtSAC were in the triplet locally excited state (³LE) at 2.988 eV. In particular, the phosphorescence spectra of OBOtSAC and tBuOBOtSAC in frozen toluene were identical to the vibrational structure of the electron donor tSAC (Figure 3-2d), indicating that the ³LE characteristics of OBOtSAC and tBuOBOtSAC

originate from tSAc. Since both the singlet and triplet energy states of OBOtSAc and tBuOBOtSAc were from the same CT state in the films, the spin-orbit coupling efficiency might be low.²⁵ However, since ³LE exists between ¹CT and ³CT, the emitters exhibited efficient TADF and showed high PLQYs because of the facile electron transfer from ³CT to ¹CT *via* ³LE according to El-Sayed's rule.

The presence of TADF emission was confirmed using TCSPC measurements (Figure 3-2e). When compared with the instrument response function (IRF), both OBOtSAc and tBuOBOtSAc showed clear TADF emission. The rate constants, which were calculated using previously reported methods, including PLQYs and lifetimes, are shown in Table 3-3.^{26, 27} The ΔE_{ST} of OBOtSAc is smaller than that of tBuOBOtSAc because of the stronger CT character of OBOtSAc compared to that of tBuOBOtSAc. Consequently, because the triplet was used more efficiently in OBOtSAc, the lifetime of the delayed component is shorter and the k_{TADF} and k_{RISC} are faster than those of tBuOBOtSAc.

The horizontal molecular orientation of the 10 wt% doped films of emitters in a DPEPO host was investigated by ADPL measurements (Figure 3-2f).^{28, 29} Since OBOtSAc and tBuOBOtSAc have extended linear molecular shapes, they showed 88% and 90% horizontal orientations, respectively. The relatively high horizontal

orientation value of tBuOBtSAC results from the slightly more extended structure due to the *tert*-butyl group at the end of the OBO. Considering that the 66% horizontal orientation of isotropic emitters shows an out-coupling efficiency of only 20–25%, the high horizontal orientation of OBtSAC and tBuOBtSAC is expected to significantly improve the outcoupling efficiency.

The thermal stability of the emitters was determined by DSC and TGA. DSC and TGA studies were conducted with a TA instrument and DSC Q10 and Q50 thermogravimetric analyzers in a nitrogen atmosphere, at a heating rate of $10\text{ }^{\circ}\text{C min}^{-1}$. The results are shown in Figure S3–2 and summarized in Table 3–2. Neither OBtSAC nor tBuOBtSAC showed any thermal change from -40 to $400\text{ }^{\circ}\text{C}$ in the DSC thermogram. The TGA thermograms revealed that the temperatures at 5 wt% loss (T_d) of OBtSAC and tBuOBtSAC were 446 and $456\text{ }^{\circ}\text{C}$, respectively, indicating their excellent thermal stabilities.

CV was conducted to investigate the electrical properties of the emitters. The results of the CV are shown in Figure S–3 and summarized in Table 3–2. The HOMO levels of OBtSAC and tBuOBtSAC were calculated to be 5.36 and 5.35 eV , respectively. Since both materials have a tSAC unit as a common electron donor, separated from the electron acceptor, they showed similar HOMO

values. The LUMO levels of OBOtSAc and tBuOBOtSAc were calculated to be 2.21 and 2.20 eV, respectively, considering the optical energy gap. Thus, DPEPO (HOMO = 6.5 eV, LUMO = 2.5 eV) can serve as a suitable host material for OLED fabrication.²⁴

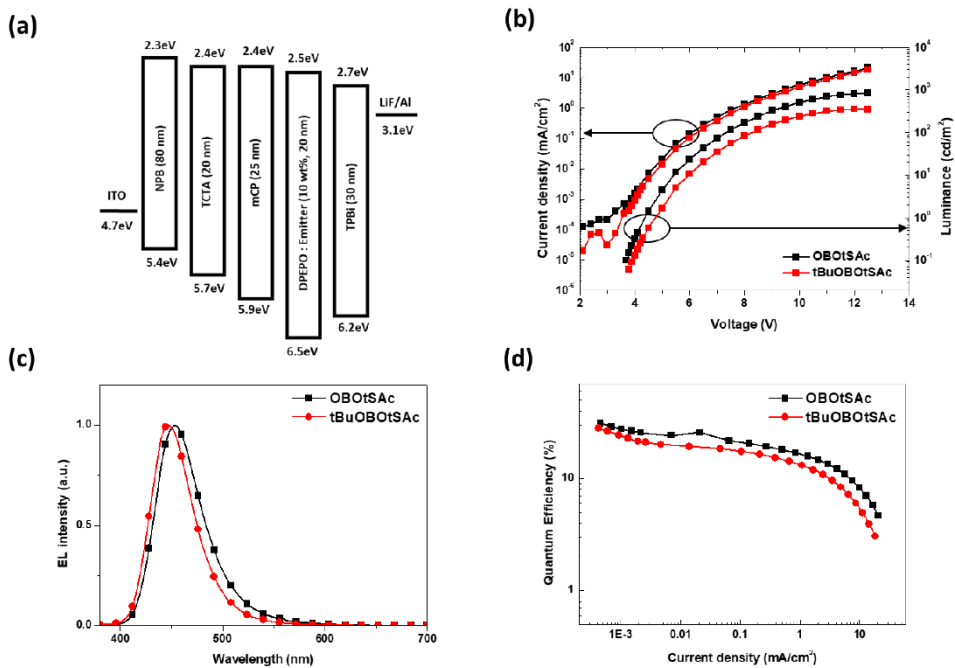


Figure 3-3. a) Optimized device structure of OBOTsAc and tBuOBOTsAc. b) Voltage-current density (V-J) and voltage-luminance (V-L) graph. c) Emission spectra at 100 cd m⁻². d) External quantum efficiency-current density (EQE-J) graph.

Table 3–4. OLED data of OBOtSAc– and tBuOBOtSAc–based devices

Compound	$V_{\text{on}}^{\text{a)}$ [V]	$\text{EQE}_{\text{max}}^{\text{b)}$ [%]	$L_{\text{max}}^{\text{c)}$ [cd m^{-2}]	$\lambda_{\text{max}}^{\text{d)}$ [nm]	FWHM [nm]	CIE ^{e)} [x, y]
OBOtSAc	3.7	31.2	832	452	50	(0.147, 0.092)
tBuOBOtSAc	3.8	28.2	353	448	48	(0.149, 0.061)

^{a)} Turn on voltage; ^{b)} Maximum EQE; ^{c)} Maximum luminance; ^{d)} EL emission wavelength at 100 cd m^{-2} ; ^{e)} CIE 1931 color coordinates.

The characteristics of the OLED devices were measured using the following device structure: indium tin oxide (ITO) (70 nm)/*N,N'*-bis(naphthalen-1-yl)-*N,N'*-bis(phenyl)benzidine (NPB, 80 nm)/tris(4-carbazoyl-9-ylphenyl)amine (TCTA, 20 nm)/1,3-di(9*H*-carbazol-9-yl)benzene (mCP, 25 nm)/ DPEPO:emitter (10 wt%, 20 nm)/2,2',2''-(1,3,5-benzinetriyl)-tris(1-phenyl-1*H*-benzimidazole) (TPBi, 30 nm)/LiF (1 nm)/Al (100 nm). The device data are presented in Figure 3–3 and summarized in Table 3–4. The emission spectra of the OLEDs showed deep-blue emission with a narrow FWHM, which is similar to the PL spectra. Further, there was no change in the wavelength even when the voltage increased (Figure S3–4). Therefore, the light emission of OLEDs originated solely from the emitters, and the excitons were well confined. The OLED device, using OBOtSAc as an emitter, showed a maximum EQE of 31.2% and CIE coordinates of (0.147, 0.092). Moreover, the tBuOBOtSAc–

based OLED devices exhibited a maximum EQE of 28.2% and CIE coordinates of (0.149, 0.061). Notably, OBOtSAC-based OLEDs showed the best EQE with a CIE y of < 0.1 , and the tBuOBOtSAC-based device showed the highest EQE with a CIE y of < 0.07 . To the best of our knowledge, tBuOBOtSAC is the most efficient TADF emitter, showing narrow deep-blue emission with the CIE y coordinate of < 0.07 . The luminance of OBOtSAC and tBuOBOtSAC was slightly low because of the use of DPEPO which has a low hole mobility. We expect that a suitable bipolar host with a high triplet energy would produce devices with high luminance while maintaining high efficiency.

3.4. Conclusion

In summary, we have developed highly efficient deep-blue TADF emitters, namely OBOtSAC and tBuOBOtSAC. OBOtSAC and tBuOBOtSAC are composed of rigid boron-based electron acceptors and a rigid and linear tri-spiral acridine electron donor, which are connected almost perpendicularly. OBOtSAC and tBuOBOtSAC showed λ_{\max} values of 452 and 446 nm, and narrow FWHM values of 50 and 48 nm in toluene, respectively. The 10 wt% doped films of OBOtSAC and tBuOBOtSAC in a DPEPO host showed extremely small ΔE_{ST} values of 0.057 and 0.078 eV, respectively. Furthermore, since

^3LE exists between ^1CT and ^3CT in both emitters, efficient triplet exciton utilization was achieved by facile electron transfer from ^3CT to ^1CT *via* ^3LE . Consequently, the 10 wt% OBOtSAc- and tBuOBOtSAc-doped DPEPO films showed 97% and 90% PLQYs, respectively, and clear TADF emission. In addition, the highly linear molecular shapes of OBOtSAc and tBuOBOtSAc caused horizontal orientations of 88% and 90%, respectively. As a result, OLED devices using OBOtSAc and tBuOBOtSAc show CIE y coordinates of 0.092 and 0.061, with high EQE_{max} values of 31.2% and 28.2%, respectively. Remarkably, the judicious selection of an extended tri-spiral acridine-based electron donor and a boron-fused rigid electron acceptor of an appropriate HOMO/LUMO leads to further improvement in both the EQEs and CIE y coordinates.

3.5. References

1. Y. Lee and J.-I. Hong, *Adv. Opt. Mater.*, 2021, 9, 2100406.
2. H. Uoyama, K. Goushi, K. Shizu, H. Nomura and C. Adachi, *Nature*, 2012, 492, 234–238.
3. S. Hirata, Y. Sakai, K. Masui, H. Tanaka, S. Y. Lee, H. Nomura, N. Nakamura, M. Yasumatsu, H. Nakanotani, Q. Zhang, K. Shizu, H. Miyazaki and C. Adachi, *Nat. Mater.*, 2015, 14, 330–336.
4. Y. Im, M. Kim, Y. J. Cho, J.-A. Seo, K. S. Yook and J. Y. Lee, *Chem. Mater.*, 2017, 29, 1946–1963.
5. B. Li, Z. Li, T. Hu, Y. Zhang, Y. Wang, Y. Yi, F. Guo and L. Zhao, *J. Mater. Chem. C*, 2018, 6, 2351–2359.
6. G. Kreiza, D. Banevičius, J. Jovaišaitė, S. Juršėnas, T. Javorskis, V. Vaitkevičius, E. Orentas and K. Kazlauskas, *J. Mater. Chem. C*, 2020, 8, 8560–8566.
7. T. Hatakeyama, K. Shiren, K. Nakajima, S. Nomura, S. Nakatsuka, K. Kinoshita, J. Ni, Y. Ono and T. Ikuta, *Adv. Mat.*, 2016, 28, 2777–2781.
8. M. Godumala, S. Choi, M. J. Cho and D. H. Choi, *J. Mater. Chem. C*, 2016, 4, 11355–11381.
9. Y. J. Cho, S. K. Jeon, S.-S. Lee, E. Yu and J. Y. Lee, *Chem. Mater.*, 2016, 28, 5400–5405.
10. D. H. Ahn, S. W. Kim, H. Lee, I. J. Ko, D. Karthik, J. Y. Lee

- and J. H. Kwon, *Nat. Photonics*, 2019, 13, 540–546.
11. F. Miyamoto, S. Nakatsuka, K. Yamada, K.-i. Nakayama and T. Hatakeyama, *Org. Lett.*, 2015, 17, 6158–6161.
 12. T. Hatakeyama, S. Hashimoto, S. Seki and M. Nakamura, *J. Am. Chem. Soc.*, 2011, 133, 18614–18617.
 13. H. Hirai, K. Nakajima, S. Nakatsuka, K. Shiren, J. Ni, S. Nomura, T. Ikuta and T. Hatakeyama, *Angew. Chem. Int. Ed.*, 2015, 54, 13581–13585.
 14. H. Lim, H. J. Cheon, S.-J. Woo, S.-K. Kwon, Y.-H. Kim and J.-J. Kim, *Adv. Mat.*, 2020, 32, 2004083.
 15. T.-A. Lin, T. Chatterjee, W.-L. Tsai, W.-K. Lee, M.-J. Wu, M. Jiao, K.-C. Pan, C.-L. Yi, C.-L. Chung, K.-T. Wong and C.-C. Wu, *Adv. Mat.*, 2016, 28, 6976–6983.
 16. Y. Lee, S.-J. Woo, J.-J. Kim and J.-I. Hong, *Org. Electron.*, 2020, 78, 105600.
 17. S. Sun, R. Guo, Q. Zhang, X. Lv, P. Leng, Y. Wang, Z. Huang and L. Wang, *Dyes Pigm.*, 2020, 178, 108367.
 18. Y. Lee, S.-J. Woo, J.-J. Kim and J.-I. Hong, *Dyes Pigm.*, 2020, 172, 107864.
 19. W. Brütting, J. Frischeisen, T. D. Schmidt, B. J. Scholz and C. Mayr, *Phys. Status Solidi A*, 2013, 210, 44–65.
 20. D. Yokoyama, *J. Mater. Chem. A*, 2011, 21, 19187–19202.

21. Y. Lee and J.-I. Hong, *J. Mater. Chem. C*, 2020, 8, 8012–8017.
22. Y. Xiang, P. Li, S. Gong, Y.-H. Huang, C.-Y. Wang, C. Zhong, W. Zeng, Z. Chen, W.-K. Lee, X. Yin, C.-C. Wu and C. Yang, *Sci. Adv.*, 2020, 6, eaba7855.
23. W. Li, B. Li, X. Cai, L. Gan, Z. Xu, W. Li, K. Liu, D. Chen and S.-J. Su, *Angew. Chem. Int. Ed.*, 2019, 58, 11301–11305.
24. J. Zhang, D. Ding, Y. Wei and H. Xu, *Chem. Sci.*, 2016, 7, 2870–2882.
25. P. K. Samanta, D. Kim, V. Coropceanu and J.-L. Brédas, *J. Am. Chem. Soc.*, 2017, 139, 4042–4051.
26. S. Oda, B. Kawakami, R. Kawasumi, R. Okita and T. Hatakeyama, *Org. Lett.*, 2019, 21, 9311–9314.
27. J. Lee, N. Aizawa, M. Numata, C. Adachi and T. Yasuda, *Adv. Mat.*, 2017, 29, 1604856.
28. J. Frischeisen, D. Yokoyama, C. Adachi and W. Brütting, *Appl. Phys. Lett.*, 2010, 96, 073302.
29. S.-Y. Kim, W.-I. Jeong, C. Mayr, Y.-S. Park, K.-H. Kim, J.-H. Lee, C.-K. Moon, W. Brütting and J.-J. Kim, *Adv. Funct. Mater.*, 2013, 23, 3896–3900.

3.6. Supplementary data

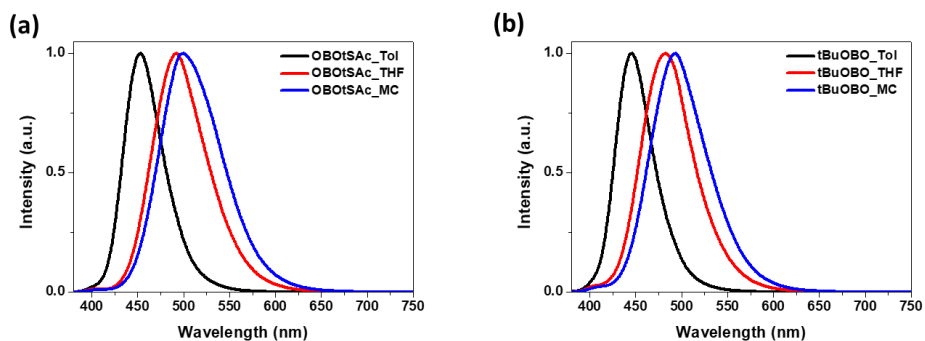


Figure S3–1. PL spectra of (a) OBOtSAC and (b) tBuOBtSAC with varying solvent polarity.

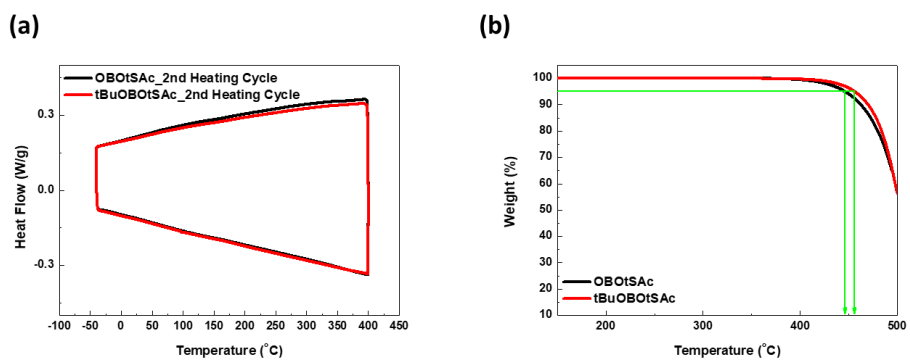


Figure S3–2. (a) DSC thermograms, (b) TGA thermograms of OBOtSAC and tBuOBtSAC.

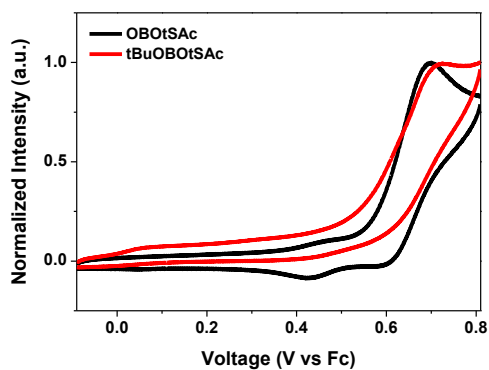


Figure S3–3. Cyclic voltammograms.

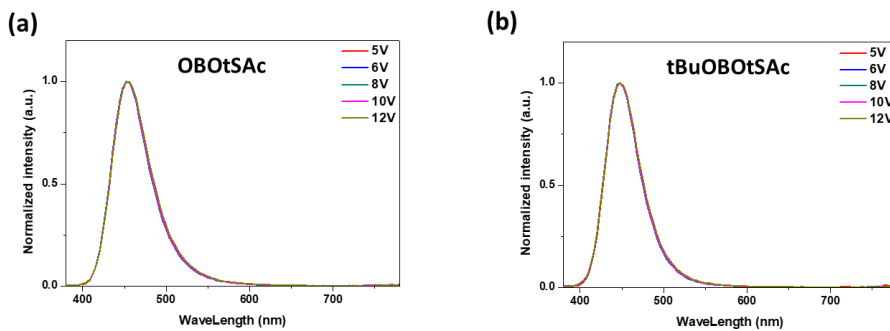


Figure S3–4. EL spectra at various operation voltages of devices fabricated with (a) OBOtSAc and (b) tBuOBOtSAc.

Chapter 4. Multiple Resonance Thermally
Activated Delayed Fluorescence Enhanced by
Halogen Atoms

Chapter 4. Multiple Resonance Thermally Activated Delayed Fluorescence Enhanced by Halogen Atoms

4.1. Introduction

Recently, numerous studies have been conducted on the development of organic light-emitting diodes (OLEDs) emitters using thermally activated delayed fluorescence (TADF).¹⁻³ TADF emitters generally consist of twisted electron donor-acceptor structures to separate the highest occupied molecular orbital (HOMO) and lowest unoccupied molecular orbital (LUMO). As a result, the energy difference between singlet and triplet states (ΔE_{ST}) could be small enough to reverse the intersystem crossing between the singlet and triplet states. Thus, triplet states can also participate in emission as delayed fluorescence and 100% IQE can be achieved. Based on this concept, numerous results involving high EQEs in red, green, and blue emitters were reported.⁴⁻⁶ However, since the twisted TADF structures exhibit strong charge transfer emission and have large reorganization energy,⁷ OLED based on the twisted TADF emitters would lead to a high external quantum efficiency (EQE) along with too wide full width at half maximum (FWHM).

Hatakeyama et al. resolved the problem of wide FWHM by introducing boron with electron-withdrawing ability and nitrogen with electron-donating ability into a fused ring.³ Controlling the positions of boron and nitrogen causes a difference in

electron distribution along ortho, meta, and para positions, which is called multiple resonance thermally activated delayed fluorescence (MR-TADF). This results in the separation of HOMO and LUMO just like that of a distorted TADF structures, emitting TADF emission. In addition, the fused ring structure provides structural rigidity, exhibiting an increase of PLQY and a decrease of FWHM.

A lifetime of a twisted TADF emitter is quite short because the HOMO and LUMO are completely separated.⁸ However, ΔE_{ST} values of MR-TADF molecules are quite large compared to those of twisted TADF molecules, because their HOMO and LUMO are not completely separated.⁹ Therefore, the ratio of a delayed component in total PLQY is small and the lifetime of the delayed component is long. Recently, sensitizers were introduced to resolve the slow lifetime of MR-TADF.¹⁰¹¹ However, with the sensitizer introduced, the electronic interactions between the host, sensitizer, and MR-TADF must be considered in a complicated manner.¹² The fundamental resolution is to shorten the lifetime of the MR-TADF molecule itself.

The interaction between singlet and triplet states can be expressed as follows:

$$\lambda \propto H_{SO} / \Delta E_{ST}$$

the first-order mixing coefficient (λ) between singlet and triplet states is proportional to spin-orbit interaction (H_{SO}) and inversely proportional to ΔE_{ST} .¹³ Twisted TADF molecules could enhance λ by extremely lowering ΔE_{ST} . Since the MR-TADF emitter has some overlap of HOMO and LUMO, it cannot extremely

reduce the ΔE_{ST} like the twisted TADF molecule. However, λ can be increased by increasing the H_{SO} even if the ΔE_{ST} is large. When a heavy atom is introduced, orbit angular momentum and spin angular momentum are mixed and thus the H_{SO} increased, which is called a heavy atom effect. Heavy atom effects can be introduced not only by transition metals such as Ir or Pt but also by halogen atoms such as chlorine and bromine.¹⁴⁻¹⁹

With halogens introduced into the twisted TADF emitters, the performance of the emitters was improved in some cases or not.¹⁶⁻¹⁹ The rather negative effect of halogen was found when halogen was introduced into the TADF emitters with fast k_{RISC} . These molecules did not emit from an excited state because the kinetic rate constant of radiative decay (k_r^s) ($\sim 10^7$) and kinetic rate constant of reverse intersystem crossing (k_{RISC}) ($\sim 10^6$) became similar by halogen atoms. However, when halogen was introduced to twisted TADF molecules with slow k_{RISC} , the PLQY, EQE, and roll-off were improved. The MR-TADF materials have a fast k_r^s of 10^7 – 10^8 and a slow k_{RISC} of 10^4 . To the best of our knowledge, there has been no case of introducing halogen to resolve the slow k_{RISC} problem of MR-TADF emitters. Herein, we report the first case of improving TADF performance by introducing halogens into an MR-TADF molecule.

We have designed 2,12-dichloro-*N,N*,5,9-tetrakis(4-chlorophenyl)-5,9-dihydro-5,9-diaza-13*b*-boranaphtho[3,2,1-de]anthracen-7-amine (Cl-MR) and 2,12-dibromo-*N,N*,5,9-tetrakis(4-bromophenyl)-5,9-dihydro-5,9-

diaza-13*b*-boranaphtho[3,2,1-*de*]anthracen-7-amine (Br-MR) in which six Cl and Br atoms were substituted for six peripheral H atoms at the para positions of three N atoms of a *N,N*,5,9-tetraphenyl-5,9-dihydro-5,9-diaza-13*b*-boranaphtho[3,2,1-*de*]anthracen-7-amine (MR) emitter, respectively. These molecules can be easily synthesized even in the presence of a number of halogens by means of a one-pot borylation. We confirmed the enhanced spin-orbit coupling constant through density functional theory (DFT) and time-dependent density functional theory (TD-DFT) calculations. Also, it was experimentally confirmed through PL and transient PL that halogenated MR emitters used more efficiently the triplet states in both solution and film states. In particular, Cl-MR exhibited improved PLQY (85%) compared to MR (75%) and a high EQE of 27.2%. However, the lifetime of the Br-MR was greatly reduced, but improvement in PLQY and EQE could not be confirmed. We have analyzed the reason through analysis of kinetic rates and calculations of bond dissociation energy (BDE).

4.2. Experimental section

4.2.1. Quantum chemical calculations

Density functional theory (DFT) calculations were performed to predict optimized molecular structures, total enthalpies, and orbital distributions of frontier orbitals using Gaussian 09 software. B3LYP functionals and 6-31G(d) basis set were utilized for calculation of MR and Cl-MR. B3LYP functional and 6-31G(d) and

LanL2DZ basis set were utilized for Br-MR. Time-dependent density functional theory (TD-DFT) calculations were performed to estimate singlet and triplet energies and spin-orbit coupling constant of excited states using Orca 5.0.1 software at B3LYP/G functional and def2-SVP basis set. Natural transition orbital calculations were performed to predict orbital distributions of excited states using Gaussian 09 software at B3LYP/6-31G(d) level.

4.2.2. Photophysical property analysis

Ultraviolet-visible (UV-vis) spectra were recorded on a Jasco V-730 spectrophotometer. Fluorescence and phosphorescence spectra were recorded on a Jasco FP-8300 spectrophotometer. Absolute quantum efficiency was obtained with a PTI QuantaMaster 40 spectrofluorometer using a 3.2 in. integrating sphere at room temperature. Transient photoluminescence (PL) was measured through the time-correlated single-photon counting (TCSPC) techniques by using a PicoQuant, FluoTime 250 instrument. A 377 nm pulsed laser was used as an excitation source.

4.2.3. Electrochemical and thermal analysis

Cyclic voltammetry (CV) were conducted in dichloromethane solution (1.00 mM) with 0.1 M tetra-*n*-butylammonium perchlorate (TBAP) as the supporting electrolyte. A glassy carbon electrode was employed as the working electrode and referenced to an Ag reference electrode. All potential values were calibrated

against the ferrocene/ferrocenium (Fc/Fc^+) redox couple. The onset potential was determined from the intersection of two tangents drawn at the rising and background current of the cyclic voltammogram. Differential scanning calorimetry (DSC) and thermogravimetric analysis (TGA) were performed with DSC Q10 and TGA Q50 of TA instruments in a nitrogen atmosphere at a heating rate of $10\text{ }^\circ\text{C min}^{-1}$.

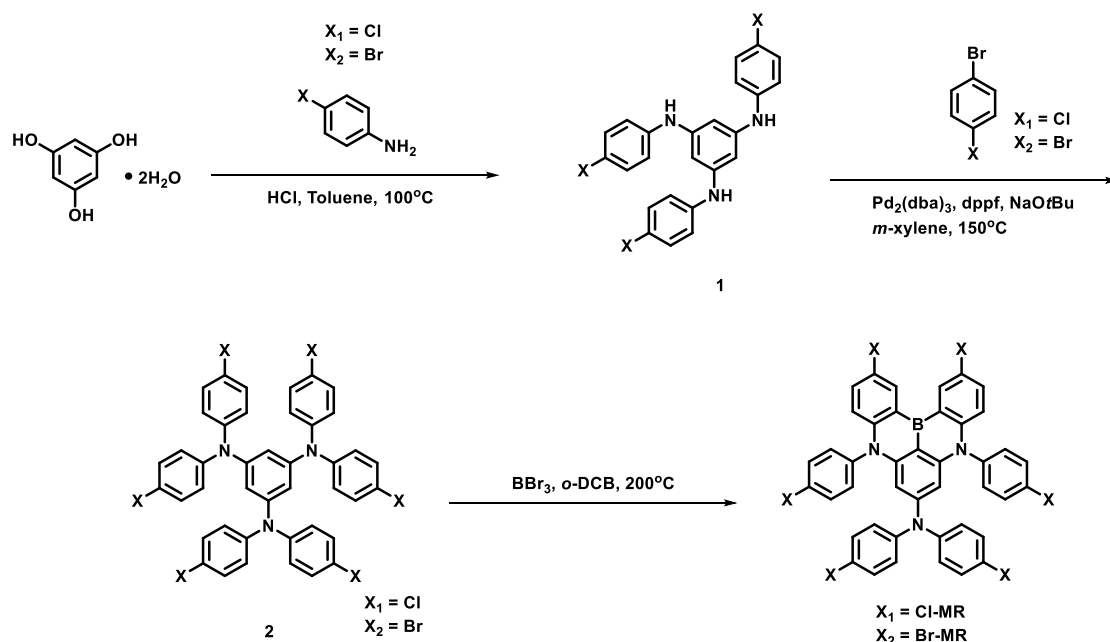
4.2.4. Device fabrication and measurements

The patterned indium–tin–oxide (ITO, 70 nm) substrates were washed with water and isopropyl alcohol, followed by 10 min UV–ozone treatment. Organic layers, LiF, and Al were thermally evaporated at a deposition rate of $1\text{--}2\text{ \AA s}^{-1}$ for organic layers, 0.1 \AA s^{-1} for LiF, and $3\text{--}5\text{ \AA s}^{-1}$ for the Al electrode. OLED properties were measured using a Keithley source meter 2400 and a PR–650 spectrascan colorimeter.

4.2.5. Synthesis and characterization

Commercially available reagents and solvents were used without further purification unless otherwise noted. MR was synthesized by following the previously reported reference. ^1H – and ^{13}C –spectra were recorded using a Varian/Oxford As–500 500 MHz in CDCl_3 and DMSO. ^1H –NMR chemical shifts were referenced to CHCl_3 (7.26 ppm) and DMSO (2.50 ppm). ^{13}C –NMR chemical shifts in CDCl_3 were reported relative to CHCl_3 (77.23 ppm). High–resolution mass

spectrometric (HRMS) data (JEOL, JMS-700) with fast atom bombardment (FAB) positive mode were received directly from the National Center for Inter-University Research Facilities (NCIRF).



Scheme 4-1. Synthetic routes of Cl-MR and Br-MR.

4.2.5.1. Synthesis of *N*1,*N*3,*N*5-tris(4-chlorophenyl)benzene-1,3,5-triamine (1-Cl)

A mixture of phloroglucinol dihydrate (3.0 g, 18.5 mmol), 4-chloroaniline (9.4 g, 74.0 mmol), and catalytic amount of HCl in toluene (14 mL) was degassed and refilled with nitrogen gas. Then, the reaction mixture was stirred at 100 °C for 1 h. The reaction mixture was cooled to room temperature and the solvent was evaporated. The crude product was purified by recrystallization from single phase

ethanol to afford 1-Cl (7.1 g, 84%) as a pale brown solid. $^1\text{H NMR}$ (500 MHz, CDCl_3) δ 7.21 (d, $J = 8.7$ Hz, 6H), 7.00 (d, $J = 8.7$ Hz, 6H), 6.26 (s, 3H), 5.60 (s, 3H).

4.2.5.2. Synthesis of $N1,N1,N3,N3,N5,N5$ -hexakis(4-chlorophenyl)benzene-1,3,5-triamine (2-Cl)

A mixture of 1-Cl (1.1 g, 1.87 mmol), 1-bromo-4-chlorobenzene (3.2 g, 16.8 mmol), tris(dibenzylideneacetone)dipalladium(0) (86 mg, 0.094 mmol), 1,1'-bis(diphenylphosphino)ferrocene (209 mg, 0.37 mmol), and NaOtBu (650 mg, 6.73 mmol) in *m*-xylene (37 mL) was degassed and refilled with nitrogen gas. Then, the reaction mixture was stirred at 150°C for 24 h. The reaction mixture was cooled to room temperature and filtered with silica using dichloromethane. After the solvent was evaporated, the crude product was purified by column chromatography using dichloromethane and hexane (1:6) to afford 2-Cl (1.2 g, 82%) as a white solid. $^1\text{H NMR}$ (500 MHz, CDCl_3) δ 7.15 (d, $J = 8.7$ Hz, 12H), 6.91 (d, $J = 8.7$ Hz, 13H), 6.26 (s, 3H).

4.2.5.3. Synthesis of 2,12-dichloro- $N,N,5,9$ -tetrakis(4-chlorophenyl)-5,9-dihydro-5,9-diaza-13b-boranaphtho[3,2,1-de]anthracen-7-amine (Cl-MR)

A mixture of 2-Cl (1.1 g, 1.40 mmol) and *o*-DCB were degassed and refilled with nitrogen gas. After the reaction mixture was cooled using ice water and reached to 0°C , boron tribromide (12.6 g, 50.4 mmol) was added to the mixture.

Then, the reaction mixture was stirred at 200°C for 24 h. The reaction mixture was cooled to room temperature and degassed for removing HBr gas. After poured on to the ice water, organic phase extract with dichloromethane. After the solvent was evaporated, the crude product was purified by column chromatography (CHCl₃:Hex=1:6) and recrystallization from dichloromethane and ethanol to afford Cl-MR (640 mg, 56%) as a yellow solid ¹H NMR (500 MHz, DMSO) δ 8.58 (d, J = 2.5 Hz, 2H), 7.67 (d, J = 8.6 Hz, 4H), 7.53 (dd, J = 9.3, 2.4 Hz, 2H), 7.34 (d, J = 8.5 Hz, 4H), 7.27 (d, J = 8.7 Hz, 4H), 6.97 (d, J = 8.8 Hz, 4H), 6.74 (d, J = 9.2 Hz, 2H), 5.35 (s, 2H); ¹³C NMR (125 MHz, CDCl₃) δ 151.00, 147.67, 145.63, 144.38, 139.96, 134.83, 133.38, 131.38, 131.27, 130.91, 129.70, 129.20, 126.76, 126.06, 118.35, 98.28, 77.25, 77.00, 76.75; HRMS (FAB+) m/z: [M]⁺ calcd for C₄₂H₂₄BCl₆N₃: 791.0194; found: 791.0202.

1.5.4. Synthesis of *N1,N3,N5*-tris(4-bromophenyl)benzene-1,3,5-triamine (1-Br)

A mixture of phloroglucinoldihydrate (500 mg, 3.96 mmol), 4-bromoaniline (2.73 g, 15.86 mmol), and catalytic amount of HCl in toluene (3 mL) was degassed and refilled with nitrogen gas. Then, the reaction mixture was stirred at 100°C for 1 h. The reaction mixture was cooled to room temperature and the solvent was evaporated. The crude product was purified by recrystallization from single phase ethanol to afford 1-Br (1.21 g, 52%) as a dark brown solid. ¹H NMR (500 MHz,

CDCl₃) δ 7.35 (d, J = 8.7 Hz, 6H), 6.95 (d, J = 8.6 Hz, 6H), 6.28 (s, 3H), 5.61 (s, 3H).

1.5.5. Synthesis of *N*₁,*N*₁,*N*₃,*N*₃,*N*₅,*N*₅-hexakis(4-bromophenyl)benzene-1,3,5-triamine (2-Br)

A mixture of 1-Br (1.0 g, 1.7 mmol), 1,4-dibromobenzene (6 g, 25.5 mmol), tris(dibenzylideneacetone)dipalladium(0) (78 mg, 0.085 mmol), 1,1'-bis(diphenylphosphino)ferrocene (188 mg, 0.34 mmol), and NaOtBu (588 mg, 6.12 mmol) in *m*-xylene (17 mL) was degassed and refilled with nitrogen gas. Then, the reaction mixture was stirred at 150°C for 24 h. The reaction mixture was cooled to room temperature and filtered with silica using dichloromethane. After the solvent was evaporated, the crude product was purified by column chromatography using dichloromethane and hexane (1:6) to afford 2-Br (1.1 g, 65%) as a white solid. ¹H NMR (500 MHz, CDCl₃) δ 7.31 – 7.28 (m, 12H), 6.88 – 6.84 (m, 12H), 6.28 (s, 3H).

1.5.5. Synthesis of 2,12-dibromo-*N,N*,5,9-tetrakis(4-bromophenyl)-5,9-dihydro-5,9-diaza-13b-boranaphtho[3,2,1-de]anthracen-7-amine (Br-MR)

A mixture of 2-Br (1.0 g, 0.94 mmol) and *o*-DCB were degassed and refilled with nitrogen gas. After the reaction mixture was cooled using ice water and reached to 0°C, boron tribromide (8.5 g, 33.8 mmol) was added to the mixture.

Then, the reaction mixture was stirred at 200°C for 24 h. The reaction mixture was cooled to room temperature and degassed for removing HBr gas. After poured on to the ice water, organic phase extract with dichloromethane. After the solvent was evaporated, the crude product was purified by recrystallization from chloroform and ethanol to afford Br-MR (630 mg, 63%) as a yellow solid. ¹H NMR (400 MHz, DMSO) δ 8.69 (d, J = 1.8 Hz, 2H), 7.81 (d, J = 8.3 Hz, 4H), 7.64 (dd, J = 8.9, 2.0 Hz, 2H), 7.39 (d, J = 8.7 Hz, 4H), 7.27 (d, J = 8.4 Hz, 4H), 6.90 (d, J = 8.7 Hz, 4H), 6.68 (d, J = 9.1 Hz, 2H), 5.38 (s, 2H); ¹³C NMR (125 MHz, CDCl₃) δ 151.00, 147.67, 145.63, 144.38, 139.96, 134.83, 133.38, 131.38, 131.27, 130.91, 129.70, 129.20, 126.76, 126.06, 118.35, 98.28, 77.25, 77.00, 76.75; HRMS (FAB+) m/z: [M]⁺ calcd for C₄₂H₂₄BBr₆N₃: 1054.7164; found: 1054.7187.

4.3. Results and discussion

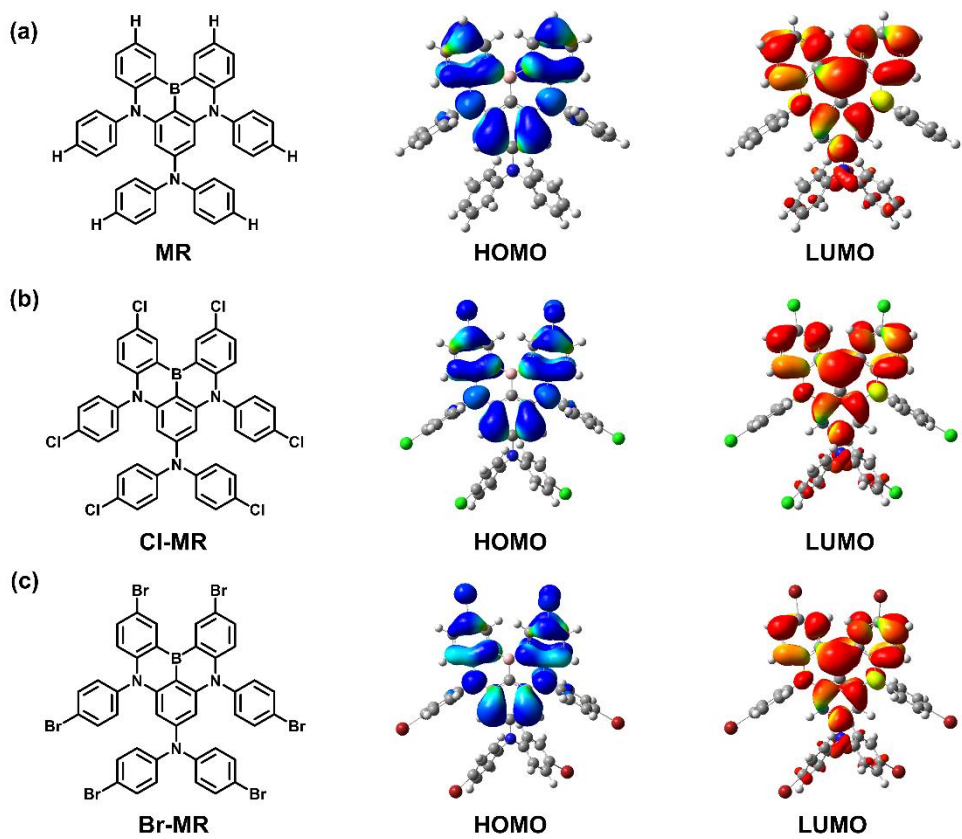


Figure 2-1 Molecular structures and frontier orbitals (blue: HOMO, red: LUMO). (a) MR, (b) Cl-MR, (c) Br-MR.

Table 4–1. Calculated Data

Compound	HOMO [eV]	LUMO [eV]	E_{gap} ^[a] [eV]	S_1 ^[b] [eV]	T_1 ^[c] [eV]	T_2 ^[d] [eV]	$\langle S_1 H_{\text{SO}} T_1 \rangle$ ^[e] [cm ⁻¹]	$\langle S_1 H_{\text{SO}} T_2 \rangle$ ^[f] [cm ⁻¹]
MR	4.76	1.08	3.68	3.145	2.678	2.927	0.06	0.19
Cl–MR	5.33	1.75	3.58	3.043	2.581	2.857	0.06	0.68
Br–MR	5.42	1.84	3.58	3.052	2.599	2.864	0.19	2.21

[a] Energy gap between HOMO and LUMO. [b] Energy of the 1st singlet state, [c] Energy of the 1st triplet state, [d] Energy of the 2nd triplet state, [e] Spin–orbit coupling constant between S_1 and T_1 , [f] Spin–orbit coupling constant between the S_1 and T_2 .

We performed DFT and TD-DFT calculations to make theoretical predictions. The geometries in the ground state were optimized using B3LYP functional and 6-31G(d) basis set by Gaussian 09 software. In particular, Br-MR was calculated by introducing the B3LYP functional and LANL2DZ basis sets. To calculate the spin-orbit coupling constant through TD-DFT, the calculations were performed using the B3LYP/G functional and the def2-SVP basis set by ORCA 5.0.1 software. All the calculated results are shown in Figure 4-1 and summarized in Table 4-1. Since MR, Cl-MR, and Br-MR are all MR-TADF molecules, they show the difference in orbital distribution between the HOMO and LUMO along the ortho, meta, and para positions. Substitution of the halogen atoms did not cause any change in the frontier orbital. To confirm the effect in the excited state by halogen atoms, natural transition orbital calculations were also performed using Gaussian 09. B3LYP functional and 6-31G(d) basis set were employed (Figure S4-1, 2, 3). Halogen atoms also did not cause any change in the NTO 1, 2, and 3. Therefore, even if halogen is introduced, there will be no change in the photoluminescence mechanism.

When the electron-donating group (EDG) is introduced, E_{gap} decreases while HOMO and LUMO increase, but in the case of the electron-withdrawing group (EWG), E_{gap} increases while HOMO and LUMO decrease.^{20, 21} A halogen element, unlike the typical EDG or EWG, can act as an EDG due to the non-bonding orbital on the halogen or as an EWG by its electronegativity. Therefore, when halogen

atoms are attached, the propensity of E_{gap} , HOMO, and LUMO changes might be altered. In other words, E_{gap} may decrease while both HOMO and LUMO decrease. This propensity was confirmed through the DFT calculations. Changes of H_{SO} by the substitution of halogen elements could be confirmed through TD-DFT calculations. With the introduction of chlorine and bromine, H_{SO} was gradually increased by the heavy atom effect. Therefore, it can be expected that chlorine and bromine can enhance the TADF emission by accelerating the interaction between the singlet and triplets.

Syntheses were carried out as shown in Scheme 4-1. First, compound 1 was synthesized by the dehydration reaction under an acid catalyst. Next, compound 2 was synthesized by reacting 1 with aryl bromide through the Buchwald Hartwig reaction using 1,1'-bis(diphenylphosphino)ferrocene (dppf) ligand. Finally, Cl-MR and Br-MR were synthesized using BBr_3 by a one-pot borylation at 200°C under *o*-DCB solvent conditions. MR-TADF materials generally form a ring through selective borylation with a lithium-halogen exchange reaction.³ However, in the case of halogenated MR-TADF, it is difficult to selectively perform borylation through lithium-halogen exchange because several halogens exist. DFT calculations (B3LYP/6-31G(d)) are conducted to predict orbital distributions of 2-Cl and 2-Br. Electrons in the HOMOs of 2-Cl and 2-Br are mainly concentrated on the ortho-position of nitrogen (Figure S4-4). Therefore, we were able to selectively carry out borylation as a one-pot reaction without any lithium-halogen

exchange reaction. New compounds were purified through column chromatography, recrystallization, and vacuum thermal sublimation. Cl-MR and Br-MR were characterized by $^1\text{H-NMR}$, $^{13}\text{C-NMR}$, and HRMS.

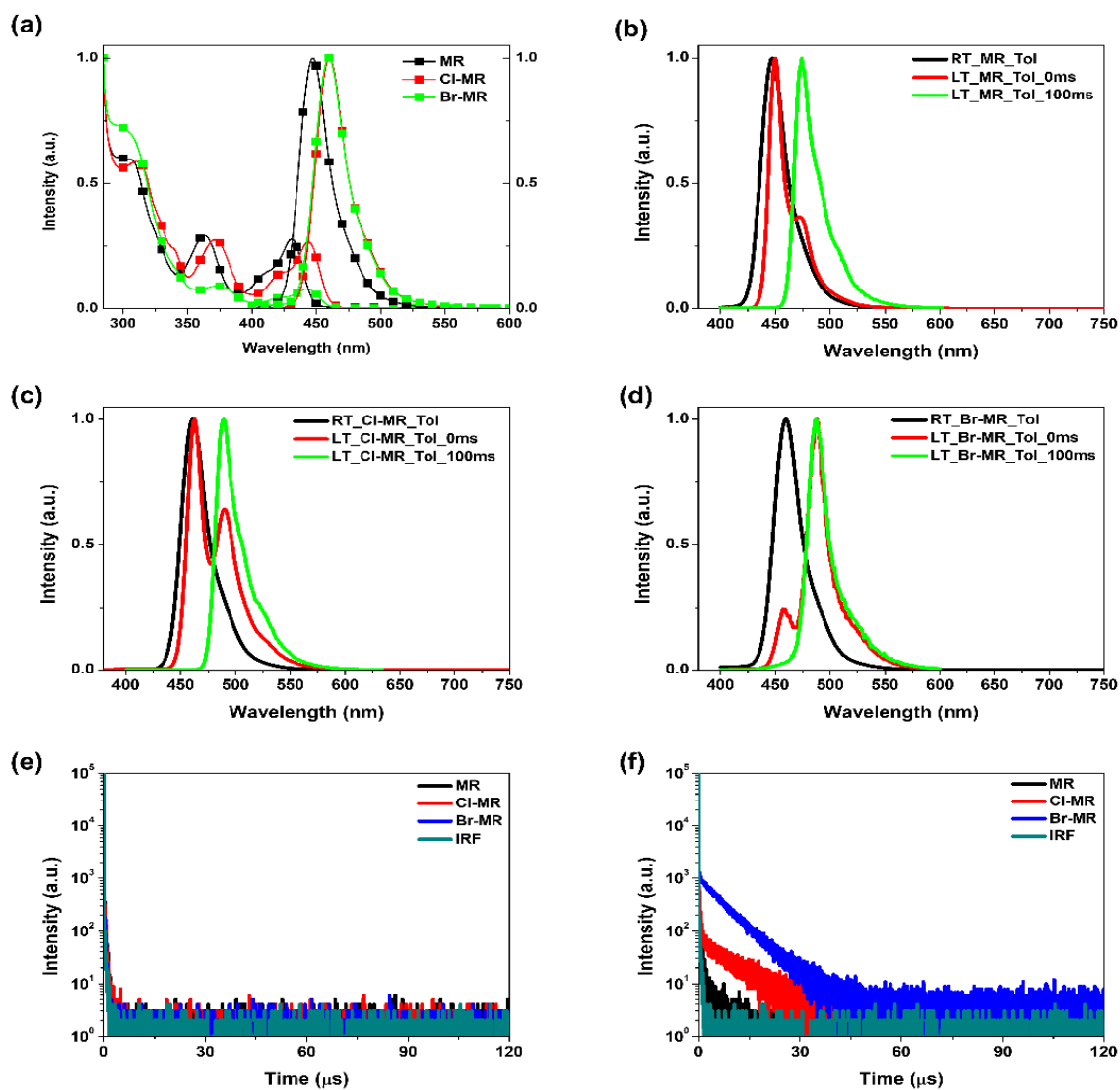


Figure 4-2. Photophysical properties in toluene (10^{-5} M) solution. a) UV-vis and PL. b) Fluorescence and phosphorescence spectra of MR. c) Fluorescence and phosphorescence spectra of Cl-MR. d) Fluorescence and phosphorescence spectra of Br-MR. e) Transient PL of aerated toluene solution. f) Transient PL of argon-bubbling toluene solution.

Table 4–2. Physical and electrochemical properties of MR–Series

Compound d	λ max [a]/[b] [nm]	FWHM ^{[a]/[b]} [nm]	HOMO ^[c] [eV]	LUMO ^[d] [eV]	E_{gap} ^[e] [eV]	S_1 ^[f] [eV]	T_1 ^[g] [eV]	ΔE_{ST} ^[h] [eV]	Φ ^[i] [%]	Φ_{PF} ^[j] [%]	Φ_{TADF} ^[k] [%]
MR	447/456	27/36	5.09	2.32	2.77	2.85/2.80	2.71/2.67	0.14/0.13	75	70	5
Cl–MR	460/474	27/36	5.28	2.59	2.69	2.77/2.71	2.63/2.58	0.14/0.13	85	51	34
Br–MR	460/474	27/36	5.28	2.59	2.69	2.79/2.71	2.67/2.59	0.14/0.13	76	13	63

[a] Measured in the toluene solution (10^{-5} M); [b] Measured in 10 wt.% the doped films in the DPEPO host; [c] Estimated from the onset potentials in CV experiments; [d] HOMO + optical energy gap; [e] Optical energy gap; [f] Energy of the 1st singlet state; [g] Energy of the 1st triplet state; [h] Energy difference between the S_1 and T_1 ; [i] Absolute PLQY; [j] PLQY of prompt fluorescence; [j] PLQY of delayed fluorescence.

Table 4–3. Lifetimes and rate constants of MR–series

Compound	$\tau_{\text{PF}}^{[a]}$ (ns)	$\tau_{\text{DF}}^{[b]}$ (us)	k_r^s ^[c] ($\times 10^8$)	k_{DF} ^[d] ($\times 10^4$)	k_{IC} ^[e] ($\times 10^7$)	k_{ISC} ^[f] ($\times 10^7$)	k_{RISC} ^[g] ($\times 10^4$)	Φ_r^s ^[h] (%)	Φ_{IC} ^[i] (%)	Φ_{ISC} ^[j] (%)	Φ_r^{s*} (ISC) (%)	Φ_{IC^*} (ISC) (%)	Φ_{ISC^*} (ISC) (%)
MR	4.6	39	1.5	2.6	5.0	1.6	2.8	69	23	7	5	1.7	0.55
Cl–MR	4.1	17	1.2	5.8	2.2	9.8	9.8	51	9	40	20	3.6	16
Br–MR	1.0	9.9	1.3	10	4.1	83	59	13	4	83	11	3.4	69

[a] Lifetime of prompt fluorescence; [b] Lifetime of delayed fluorescence; [c] Rate constant of radiative decay; [d] Rate constant of delayed fluorescence; [e] Rate constant of internal conversion; [f] Rate constant of intersystem crossing; [g] Rate constant of reverse intersystem crossing; [h] $k_r^s/(k_r^s+k_{\text{IC}}+k_{\text{ISC}})$; [i] $k_{\text{IC}}/(k_r^s+k_{\text{IC}}+k_{\text{ISC}})$; [j] $k_{\text{ISC}}/(k_r^s+k_{\text{IC}}+k_{\text{ISC}})$.

Photophysical and electrochemical were evaluated using UV-vis absorption, CV, PL, and TCSPC experiments. The photophysical properties of the emitters in solution and film states are shown in Figures 4-2, 3 and summarized in Tables 4-2, 3. MR showed UV absorption at 430 nm, and Cl-MR, and Br-MR at 443 nm, which correspond to the HOMO-LUMO transition. The HOMO levels of MR, Cl-MR and Br-MR were calculated using the CV measurements. Using the CV and UV-vis results, the LUMO energies were calculated. The HOMO/LUMO of MR were 5.09/2.32 eV, but Cl-MR and Br-MR showed the HOMO at 5.28/2.60 eV. As in the DFT calculations, both HOMO and LUMO decreased and E_{gap} was also decreased under the influence of the halogen atoms. Since the E_{gap} was reduced, the maximum emission wavelength was red-shifted in Cl-MR (460 nm) and Br-MR (460 nm) compared to MR (447 nm). However, there were no changes in spectra shape. FWHM values were all the same in MR, Cl-MR, and Br-MR (27 nm in solution and 36 nm in film). This result can be attributed to the same emission mechanism of MR, Cl-MR, and Br-MR as shown in the NTO calculations.

In order to obtain the ΔE_{ST} values of MR, Cl-MR, and Br-MR, the PL spectra of the toluene solution were examined at room

temperature (RT) and 77 K. All three compounds showed only fluorescence at RT and phosphorescence at 77 K with a 100 ms delay. MR, Cl-MR, and Br-MR showed the same ΔE_{ST} values, indicating that halogens have no effect on ΔE_{ST} . However, when measured without delay at 77 K, a gradual difference appeared. In the case of general TADF emitters, H_{S0} is low according to the spin selection rule, so the fluorescence is predominant at low temperature with 0 ms delay.²² However, the intensity of phosphorescence versus fluorescence increases in the order of MR, Cl-MR, and Br-MR, which is in parallel with the atomic size, due to the heavy atom effect. In other words, the interaction between the singlet and triplet is strongest in the Br-MR in spite of the same ΔE_{ST} . This propensity was also clearly observable through TCSPC. All three materials exhibit only fluorescence without TADF emission in aerated toluene solution. However, after bubbling for 10 minutes using argon gas, all three materials exhibit TADF emission, but the ratio of TADF emission increased in the order of MR, Cl-MR, and Br-MR. As a result, we confirmed the effect of the halogen atoms in solution states through low-temperature PL and TCSPC.

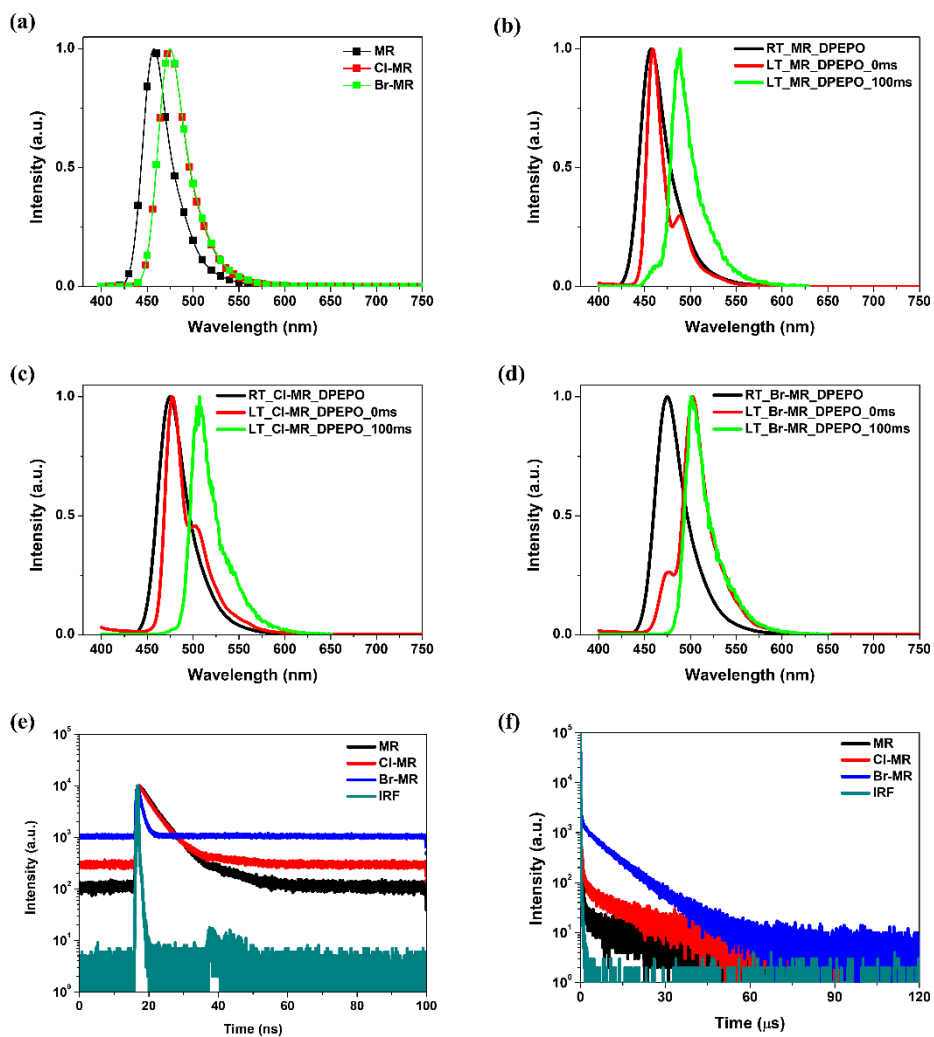


Figure 4-3. Photophysical properties of the 10 wt% doped films in the DPEPO host. a) PL. b) Fluorescence and phosphorescence spectra of MR. c) Fluorescence and phosphorescence spectra of Cl-MR. d) Fluorescence and phosphorescence spectra of Br-MR. e) Transient PL of PicoHarp mode. f) Transient PL of NanoHarp mode.

In order to confirm the photophysical properties in the film state, 10 wt% doped films with a thickness of 50 nm using bis[2-(diphenylphosphino)phenyl]ether oxide (DPEPO) host were deposited on quartz. To confine all triplets, DPEPO, which has a high triplet energy of 3.0 eV, was used.²³ The HOMO and LUMO were also properly aligned with MR, Cl-MR, and Br-MR.²⁴ At RT, the emission wavelength of the film slightly red-shifted and the FWHM increased by 9 nm, because of the polarity of DPEPO. Due to the difference of E_{gap} , the emission wavelengths of Cl-MR and Br-MR are also red-shifted compared to the MR in solution states, but the shape and FWHM of the spectra are the same. PL spectra of doped films were also obtained at RT and 77 K. As in the toluene solution, only fluorescence and phosphorescence appeared at RT and 77 K with a 100 ms delay. However, at 77 K with 0 ms delay, the ratio of phosphorescence to fluorescence is improved as in toluene solution states. That is, the interaction between singlet and triplet also increased in the film states.

The effect of halogen was confirmed through TCSPC using the doped films. The rate constants were calculated using PLQYs and lifetimes of the prompt and delayed fluorescence (Table 4-3).²⁵ First, the lifetimes of prompt component decrease in the order of MR, Cl-MR, and Br-MR (Figure 4-3e). Therefore, it was confirmed that k_{ISC}

increased in the order of MR, Cl–MR, and Br–MR by the heavy atom effect through PicoHarp mode. In addition, it was possible to confirm the gradual increase in the delayed component and the decrease in lifetime through the NanoHarp mode (Figure 4–3f). However, Br–MR has not shown any significant improvement in PLQY compared to MR in spite of an increased ratio and decreased lifetime of the delayed component. The reason could be analyzed by calculating the rate constants of excited states. Because k_{RISC} is faster than rate constant of phosphorescence (k_{r}^{T}) and rate constant of non–radiative decay at triplet state (k_{nr}^{T}), we assumed Φ_{RISC} is 1.²⁵ In the case of Cl–MR, the probability of the singlet excited state behavior returned from the T_1 is as follows: the radiative decay is 20%, internal conversion (IC) is 3.6%, and return to the T_1 is 16%. In the case of Br–MR, the probability of the singlet excited–state behavior from the T_1 is as follows: the radiative decay is 11%, IC is 3.4%, and return to the T_1 is 69%. In other words, $\Phi_{\text{r}}^{\text{S}}*\Phi_{\text{ISC}}$, $\Phi_{\text{IC}}*\Phi_{\text{ISC}}$, $\Phi_{\text{ISC}}*\Phi_{\text{ISC}}$ values of Cl–MR increased by 4, 2.1, and 29 times, respectively, compared to MR. In the case of Br–MR, $\Phi_{\text{r}}^{\text{S}}*\Phi_{\text{ISC}}$, $\Phi_{\text{IC}}*\Phi_{\text{ISC}}$, $\Phi_{\text{ISC}}*\Phi_{\text{ISC}}$ values increased by 2.2, 2, and 125 times, respectively, compared to MR. That is, in the case of Br–MR, the excited states did not emit light due to the too fast ISC and RISC, but rather stayed in the excited state. However, in the case of Cl–MR, PLQY of 10%

could be further improved compared to that of MR due to the balanced increase of kinetic rates.

TGA and DSC measurements were performed to confirm the thermal stability of the materials (Figure S4–6). DSC and TGA studies were conducted using DSC Q10 and TGA Q50, which are TA instruments, at a heating rate of $10\text{ }^{\circ}\text{C min}^{-1}$ in a nitrogen atmosphere. From the DSC graph, MR, Cl–MR, and Br–MR did not exhibit glass transition temperature (T_g) from 0 to $250\text{ }^{\circ}\text{C}$. Cl–MR and Br–MR showed improved thermal decomposition temperatures (T_d) at $450\text{ }^{\circ}\text{C}$ and $420\text{ }^{\circ}\text{C}$, respectively, compared to the MR ($384\text{ }^{\circ}\text{C}$). It was confirmed that even though halogen was introduced, it exhibited excellent thermal stability.

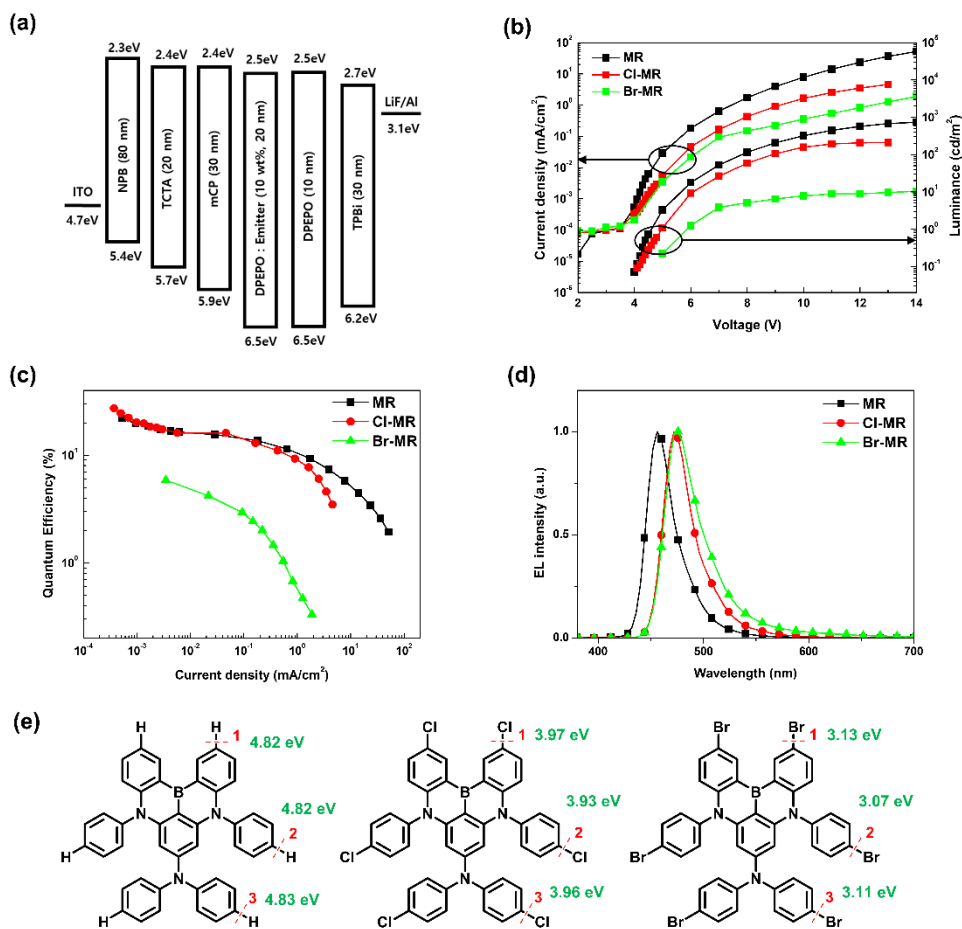


Figure 4-4. a) Optimized device structure of the MR-series. b) Voltage-current density (V - J) and voltage-luminance (V - L) graph. c) External quantum efficiency-current density (EQE- J) graph. d) Emission spectra at 10 V. e) Molecular structures and bond dissociation energy of the MR-series.

Table 4–4. OLED properties and Calculated BDE of MR–Series

Compound	V_{on} ^[a] [V]	λ_{max} ^[b] [nm]	FWHM ^[c] [nm]	EQE_{max} ^[d] [%]	L_{max} ^[e] [cd/m ²]	CIE ^[f] [x, y]	BDE–1 ^[g] [eV]	BDE–2 ^[h] [eV]	BDE–3 ^[i] [eV]
MR	4.0	456	30	21.8	732	0.14, 0.08	4.82	4.82	4.83
Cl–MR	4.2	472	30	27.2	209	0.12, 0.19	3.97	3.93	3.96
Br–MR	5.0	476	39	5.9	10.3	0.14, 0.25	3.13	3.07	3.11

[a] Turn on voltage [b] Emission wavelength at 100 cd m⁻²; [c] Full width at half maximum; [d] Maximum EQE; [e] Maximum luminance; [f] CIE 1931 color coordinates; [g] Bond dissociation energy of the 1st position; [h] Bond dissociation energy of the 2nd position; [i] Bond dissociation energy of the 3rd position

To confirm the OLED characteristics, the devices were constructed as follows: Indium tin oxide (ITO) (70 nm)/*N,N'*-bis(naphthalen-1-yl)-*N,N'*-bis(phenyl)benzidine (NPB, 80 nm)/tris(4-carbazoyl-9-ylphenyl)amine (TCTA, 20 nm)/1,3-di(9*H*-carbazol-9-yl)benzene (mCP, 30 nm)/DPEPO:emitters (10 wt%, 20 nm)/2,2',2''-(1,3,5-benzinetriyl)-tris(1-phenyl-1*H*-benzimidazole) (TPBi, 30 nm)/LiF (1 nm)/Al (100 nm). The device data are presented in Figure 4-4 and summarized in Table 4-4. The doping concentration of Br-MR was improved to 20% due to the very low luminance. MR showed an EQE of 21.8% and Commission Internationale de l'Éclairage (CIE) coordinates of (0.14, 0.08). Cl-MR showed an EQE of 27.2% and a CIE coordinate of (0.12, 0.19). When chlorine was introduced into the MR molecule, EQE was improved by using the triplet more efficiently as shown in theoretical calculations and photophysical properties. However, OLED using Br-MR had very low EQE and luminance which gradually decreased over time, making it difficult to measure. Since MR, Cl-MR, and Br-MR were all manufactured with the same device structures, it can be inferred as a problem only from Br-MR itself.

Bond dissociation energies (BDEs) were calculated to confirm the differences of the carbon-halogen bond. BDE was calculated by optimizing the structures which undergo homolytic bond cleavage of

the carbon–halogen bond, and then calculating the enthalpy (Figure S4–7, 8, 9 and Table S4–1, 2, 3). The BDE of the C–H bond of the MR material was about 4.8 eV at all three positions. The BDE of the C–Cl bond of the Cl–MR was about 3.9 eV and about 3.1 eV for Br–MR at all three positions. In the case of Br–MR, there was no significant difference with the energy level of S_1 when compared with MR and Cl–MR. Thus, when voltage of a 5 V or more was applied, accumulated high–energy excitons may affect the bond dissociation of the C–Br bond. Therefore, the OLED pixel died as the voltage increased and was hard to measure.

In the case of Cl–MR, the BDE is larger than that of Br–MR, but it is lower than that of MR. The lifetime of delayed fluorescence of Cl–MR is shorter and the PLQY is larger than that of MR, but the roll–off is severe and the maximum luminance is extremely low. Because the EQE of Cl–MR at low voltage is higher than that of MR, the triplet is effectively used compared to MR in the low current density. However, as the voltage increases, high energy excitons are accumulated and finally close to the BDE, affecting the C–Cl bond which is lower than the C–H bond. In order to reduce the roll–off of OLED using TADF molecules, it was considered that the enhancement of the k_{RISC} is significant.^{26, 27} However, although k_{RISC} was greatly increased by means of the introduction of halogen atoms,

the roll-off and device stability were severely poor. In other words, it was confirmed that in order to improve PLQY, EQE, and roll-off, not only k_{RISC} should be considered with k_{r}^{S} , k_{IC} , and k_{ISC} , but also the stability of the dopant itself should be greatly considered.

4.4. Conclusion

We introduced chlorine and bromine, which have heavy nuclei compared to hydrogen, to enhance the slow k_{RISC} of MR-TADF emitters. The orbital and spin angular momentum were mixed by the heavy atom, so that both the solution and the film utilize the triplet states more than hydrogenated MR. Due to this, Cl-MR showed enhanced PLQY of 85% and EQE of 27.2%. However, Br-MR did not show any significant improvement in PLQY and EQE, despite a fast lifetime of the delayed fluorescence compared to MR. The analysis of rate constants confirmed the importance of balancing the kinetic rates in the singlet and triplet states as well as shortening the lifetime of the delayed component. In addition, through BDE analysis, we found out the deterioration of the device due to the weak carbon-halogen bond. Our study confirmed that the introduction of a halogen atom could reduce the lifetime of delayed components, but other factors must also be considered in the development of MR-TADF emitters.

4.5. References

1. H. Uoyama, K. Goushi, K. Shizu, H. Nomura and C. Adachi, *Nature*, 2012, 492, 234–238.
2. D. H. Ahn, S. W. Kim, H. Lee, I. J. Ko, D. Karthik, J. Y. Lee and J. H. Kwon, *Nat. Photonics*, 2019, 13, 540–546.
3. T. Hatakeyama, K. Shiren, K. Nakajima, S. Nomura, S. Nakatsuka, K. Kinoshita, J. Ni, Y. Ono and T. Ikuta, *Adv. Mat.*, 2016, 28, 2777–2781.
4. Y. Lee and J.-I. Hong, *Adv. Opt. Mater.*, 2021, 9, 2100406.
5. J.-X. Chen, K. Wang, C.-J. Zheng, M. Zhang, Y.-Z. Shi, S.-L. Tao, H. Lin, W. Liu, W.-W. Tao, X.-M. Ou and X.-H. Zhang, *Adv. Sci.*, 2018, 5, 1800436.
6. T.-L. Wu, M.-J. Huang, C.-C. Lin, P.-Y. Huang, T.-Y. Chou, R.-W. Chen-Cheng, H.-W. Lin, R.-S. Liu and C.-H. Cheng, *Nat. Photonics*, 2018, 12, 235–240.
7. A. Pershin, D. Hall, V. Lemaire, J.-C. Sancho-Garcia, L. Muccioli, E. Zysman-Colman, D. Beljonne and Y. Olivier, *Nat. Commun.*, 2019, 10, 597.
8. J. U. Kim, I. S. Park, C.-Y. Chan, M. Tanaka, Y. Tsuchiya, H. Nakanotani and C. Adachi, *Nat. Commun.*, 2020, 11, 1765.
9. S. Oda, W. Kumano, T. Hama, R. Kawasumi, K. Yoshiura and T. Hatakeyama, *Angew. Chem. Int. Ed.*, 2021, 60, 2882–2886.

10. S. O. Jeon, K. H. Lee, J. S. Kim, S.-G. Ihn, Y. S. Chung, J. W. Kim, H. Lee, S. Kim, H. Choi and J. Y. Lee, *Nat. Photonics*, 2021, 15, 208–215.
11. C.-Y. Chan, M. Tanaka, Y.-T. Lee, Y.-W. Wong, H. Nakanotani, T. Hatakeyama and C. Adachi, *Nat. Photonics*, 2021, 15, 203–207.
12. Y. Wang, K. Di, Y. Duan, R. Guo, L. Lian, W. Zhang and L. Wang, *Chem. Eng. J.*, 2021, DOI: <https://doi.org/10.1016/j.cej.2021.133221>, 133221.
13. M. Y. Wong and E. Zysman-Colman, *Adv. Mat.*, 2017, 29, 1605444.
14. Z.-G. Wu, Y.-M. Jing, G.-Z. Lu, J. Zhou, Y.-X. Zheng, L. Zhou, Y. Wang and Y. Pan, *Sci. Rep.*, 2016, 6, 38478.
15. C. Cebrián and M. Mauro, *Beilstein J. Org. Chem.*, 2018, 14, 1459–1481.
16. S. Gan, S. Hu, X.-L. Li, J. Zeng, D. Zhang, T. Huang, W. Luo, Z. Zhao, L. Duan, S.-J. Su and B. Z. Tang, *ACS Appl. Mater. Interfaces*, 2018, 10, 17327–17334.
17. H. S. Kim, J. Y. Lee, S. Shin, W. Jeong, S. H. Lee, S. Kim, J. Lee, M. C. Suh and S. Yoo, *Adv. Funct. Mater.*, 2021, 31, 2104646.
18. N. Aizawa, Y. Harabuchi, S. Maeda and Y.-J. Pu, *Nat. Commun.*, 2020, 11, 3909.

19. Y. Xiang, Y. Zhao, N. Xu, S. Gong, F. Ni, K. Wu, J. Luo, G. Xie, Z.-H. Lu and C. Yang, *J. Mater. Chem. C*, 2017, 5, 12204–12210.
20. G. L. Eakins, J. S. Alford, B. J. Tiegs, B. E. Breyfogle and C. J. Stearman, *J. Phys. Org. Chem.*, 2011, 24, 1119–1128.
21. T. J. Gately, W. Sontising, C. J. Easley, I. Islam, R. O. Al-Kaysi, G. J. O. Beran and C. J. Bardeen, *CrystEngComm*, 2021, 23, 5931–5943.
22. W. Li, B. Li, X. Cai, L. Gan, Z. Xu, W. Li, K. Liu, D. Chen and S.-J. Su, *Angew. Chem. Int. Ed.*, 2019, 58, 11301–11305.
23. C. Han, Y. Zhao, H. Xu, J. Chen, Z. Deng, D. Ma, Q. Li and P. Yan, *Chem. Eur. J*, 2011, 17, 5800–5803.
24. J. Zhang, D. Ding, Y. Wei and H. Xu, *Chem. Sci.*, 2016, 7, 2870–2882.
25. J. Lee, N. Aizawa, M. Numata, C. Adachi and T. Yasuda, *Adv. Mat.*, 2017, 29, 1604856.
26. K. Masui, H. Nakanotani and C. Adachi, *Org. Electron.*, 2013, 14, 2721–2726.
27. Z. Yang, Z. Mao, Z. Xie, Y. Zhang, S. Liu, J. Zhao, J. Xu, Z. Chi and M. P. Aldred, *Chem. Soc. Rev.*, 2017, 46, 915–1016.

4.6. Supplementary data

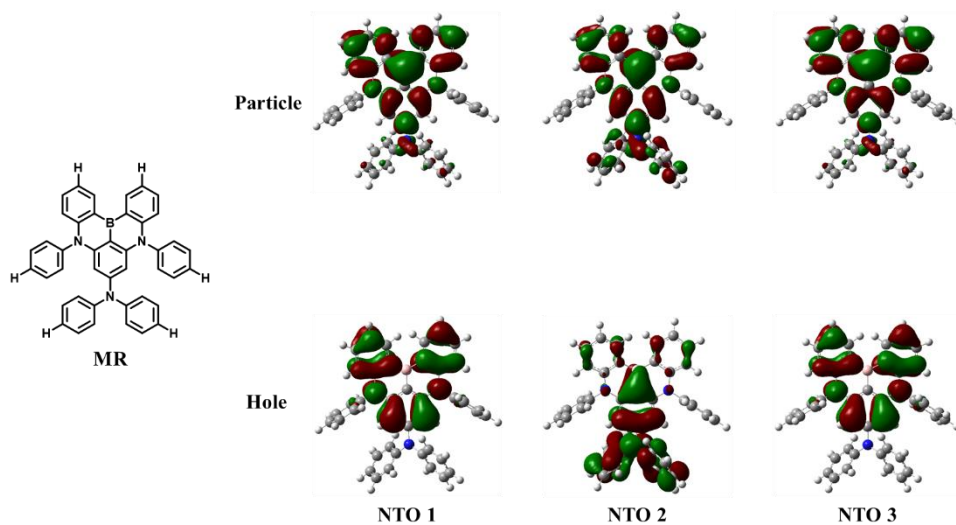


Figure S4-1. NTO distribution of MR.

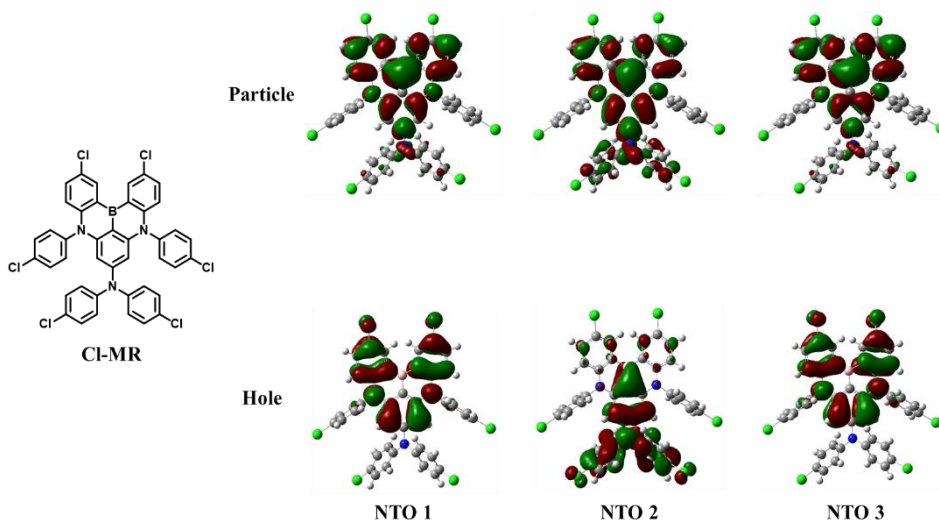


Figure S4-2. NTO distribution of Cl-MR.

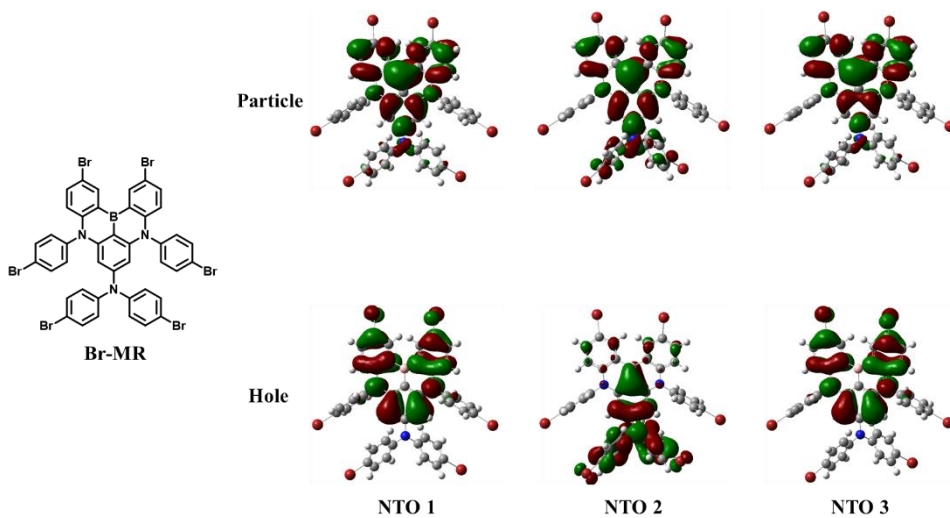


Figure S4-3. NTO distribution of Br-MR.

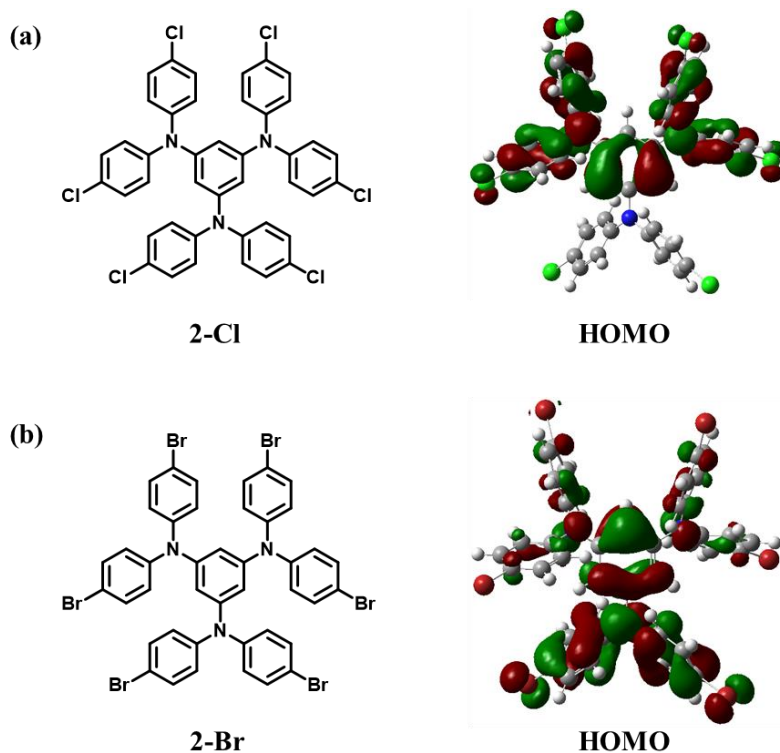


Figure S4-4. Molecular structures and orbital distributions of 2-Cl and 2-Br

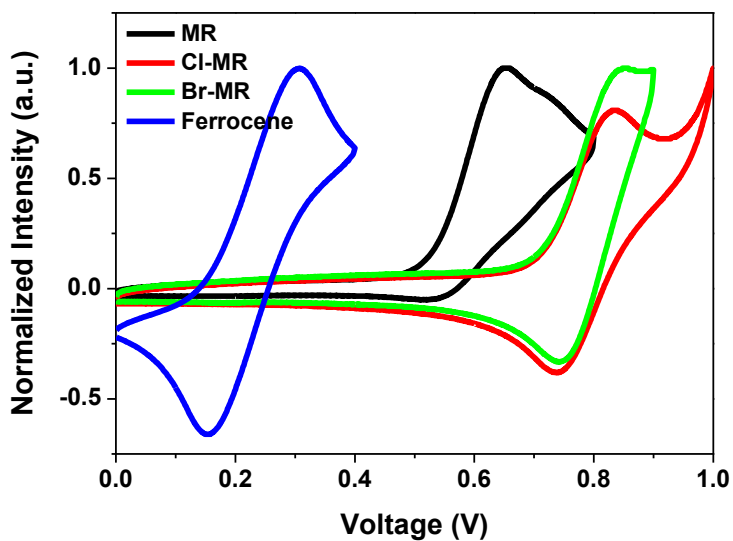


Figure S4-5. Cyclic voltammograms.

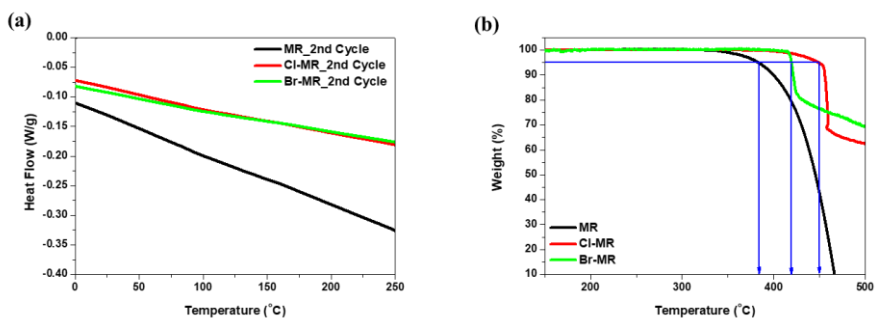


Figure S4-6. (a) DSC thermograms, (b) TGA thermograms.

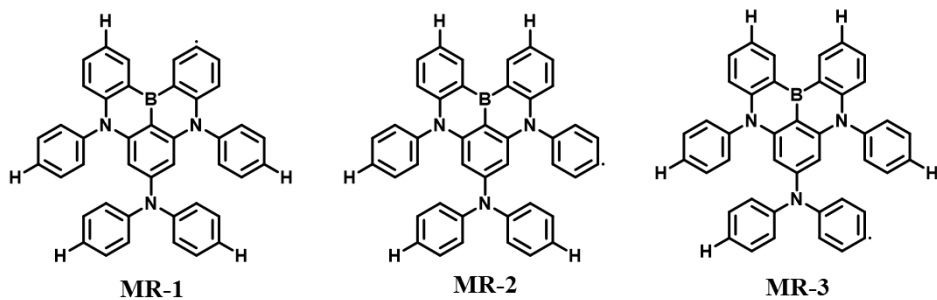


Figure S4-7. Homolyptic cleaved MR structures.

Table S4-1. Calculated enthalpies of MR structures

	MR [eV]	MR-1 [eV]	MR-2 [eV]	MR-3 [eV]	H · [eV]
Enthalpy	49172.77 14	49154.39 96	49154.39 96	49154.39 14	13.5489

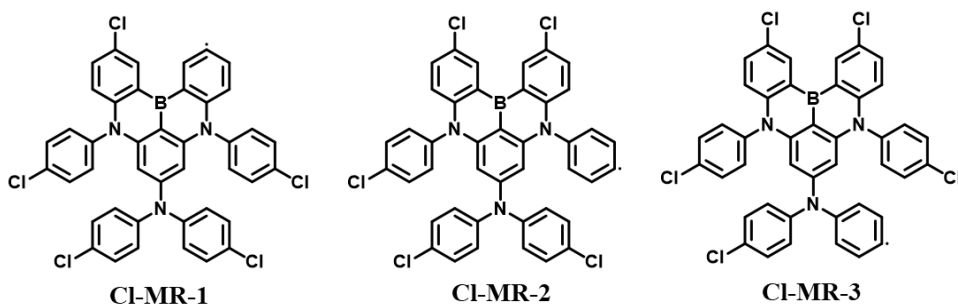


Figure S4-8. Homolyptic cleaved Cl-MR structures.

Table S4-2. Calculated enthalpies of Cl-MR structures

	Cl-MR [eV]	Cl-MR-1 [eV]	Cl-MR-2 [eV]	Cl-MR-3 [eV]	Cl · [eV]
Enthalpy	124211.5 962	111686.7 381	111686.7 792	111686.7 470	12520.88 71

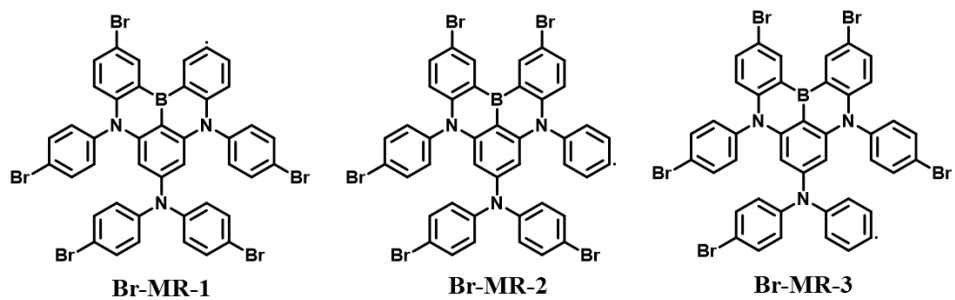


Figure S4-9. Homolytic cleaved Br-MR structures.

Table S4-3. Calculated enthalpies of Br-MR structures

	Br-MR [eV]	Br-MR-1 [eV]	Br-MR-2 [eV]	Br-MR-3 [eV]	Br · [eV]
Enthalpy	51223.57 00	50862.46 11	50863.26 12	50863.22 27	357.2336

Abstract

고효율의 유기 발광 소자를 위한 열 활성 지연 형광 발광체의 개발

이영남

유기화학전공

자연과학대학 화학과

서울대학교 대학원

열 활성 지연 형광 발광체는 유기발광 다이오드의 내부 양자 효율과 외부 양자 효율을 상당히 향상시켰다. 열 활성 지연 형광 발광체는 일반 형광 발광체에서는 사용할 수 없는 역 계간 전이를 통해 단일항과 삼중항 모두를 활용할 수 있다. 이는 뒤뜰어진 전자 주개와 받개의 구조 그리고 다중 공명 효과를 통해 가장 낮은 단일항과 삼중항의 들뜬 상태의 에너지 차이 (ΔE_{ST})가 상당히 낮기 때문이다. 따라서 삼중항은 주위의 열에너지를 이용하여 단일항으로 전환될 수 있고, 이를 통해 100%의 내부 양자 효율을 달성할 수 있게 되었다. 열 활성 지연 형광 개념을 기본으로 높은 효율의 유기발광 다이오드를 개발하기 위해 3가지 유형의 TADF 발광체를 합성하고 개발했다.

2장은 1,5-naphthyridine을 전자 받개로 phenoxazine을 전자 주개로 사용하여 개발한 2,6-bis(4-(10*H*-phenoxazin-10-yl)phenyl)-1,5-naphthyridine (NyDPO)와 2,6-bis(4-(10*H*-phenothiazin-10-yl)phenyl)-1,5-naphthyridine (NyDPT) 열지연형광

발광체에 관한 내용이다. 선형의 분자구조를 가지고 있기 때문에 NyDPO와 NyDPT 모두 각각 81%와 84%의 높은 수평 배향을 나타내었다. 더욱이 NyDPO와 NyDPt는 선명한 열 활성화 지연 형광 발광을 나타내며 각각 79%와 45%의 광 발광 양자 수율을 나타내었다. 특히 NyDPt는 유사 축 방향과 유사 적도 방향의 구조체로부터 이중 광 발광을 나타내었다. 하지만 유기발광 다이오드를 제작하였을 때 낮은 전류 밀도에서는 열 활성화 지연 형광 발광을 나타내는 유사 적도 방향의 발광만 확인할 수 있었다. 따라서 NyDPO와 NyDPt를 활용한 유기발광 다이오드를 제작하였을 때 각각 29.9%와 25.8%의 높은 외부 양자 효율과 33540 cd m^{-2} 와 14480 cd m^{-2} 의 휘도를 달성할 수 있었다.

3장은 단단한 5,9-dioxa13b-boranaphtho[3,2,1-de]anthracene (OBO) 전자 받개와 단단하고 선형의 tri-spiral acridine을 전자 주개를 활용한 10-(5,9-dioxa-13b-boranaphtho[3,2,1-de]anthracen-7-yl)-10*H*-dispiro[acridine-9,9'-anthracene-10',9''-fluorene] (OBOtSAc) and 10-(2,12-di-*tert*-butyl-5,9-dioxa-13b-boranaphtho[3,2,1-de]anthracen-7-yl)-10*H*-dispiro[acridine-9,9'-anthracene-10',9''-fluorene] (tBuOBOtSAc) 발광체에 관한 연구이다. OBOtSAc와 tBuOBOtSAc는 각각 50 nm와 40 nm의 좁은 반치폭과 짙은 파란색의 발광($\lambda_{\text{max}} = 452, 446 \text{ nm}$)을 나타냈다. 단단하고 뒤틀린 구조로 인해 두 발광체 모두 열 활성화 지연 형광에 유리한 단일항과 삼중항 에너지를 나타냈다. 따라서 bis[2-(diphenylphosphino)phenyl] ether oxide

(DPEPO)를 호스트로 사용하고 10%로 도핑한 필름은 효율적인 TADF 발광과 각각 97%, 90%의 높은 광 발광 양자 수율을 나타내었다. 더욱이 OBOtSAC와 tBuOBOtSAC는 선형의 분자 모양을 가지기에 각각 88%와 90%의 높은 수평 배향을 나타낼 수 있었다. 결과적으로 OBOtSAC와 tBuOBOtSAC를 활용한 유기발광 다이오드는 각각 31.2%와 28.2%의 외부 양자 효율, (0.147, 0.092)와 (0.149, 0.061)의 Commission Internationale de l'Éclairage (CIE) 좌표 값들을 나타내었다.

4장은 할로젠으로 치환된 다중 공명 열 활성화 지연 형광 발광체인 2,12-dichloro-*N,N*,5,9-tetrakis(4-chlorophenyl)-5,9-dihydro-5,9-diaza-13*b*-boranaphtho[3,2,1-de]anthracen-7-amine (Cl-MR)와 2,12-dibromo-*N,N*,5,9-tetrakis(4-bromophenyl)-5,9-dihydro-5,9-diaza-13*b*-boranaphtho[3,2,1-de]anthracen-7-amine (Br-MR) 개발에 관한 연구이다. Cl-MR, Br-MR은 할로젠을 이용하여 할로젠이 치환되지 않은 MR 발광체와 비교해서 $\angle E_{ST}$ 와 오비탈 분포의 변화 없이 감소된 지연 형광 수명과 향상된 역 계간 전이 속도를 나타내었다. 결과적으로 Cl-MR은 85%의 높은 광 발광 양자 수율과 27.2%의 외부 양자 효율을 나타내었다. 하지만 Br-MR은 어떠한 광 발광 양자 수율과 외부 양자 효율의 향상을 나타내지 않았다. Cl-MR과 Br-MR의 다른 성능은 들뜬 상태의 속도 상수와 탄소-할로젠 결합의 결합 분해 에너지의 분석을 통해 분석할 수 있었다.

Keywords : 발광체, 수평 배향, 유기 발광 다이오드, 다중 고리 방향족

탄화수소, 열 지연 형광

Student Number : 2016-22748